CHALMERS
UNIVERSITY OF TECHNOLOGY

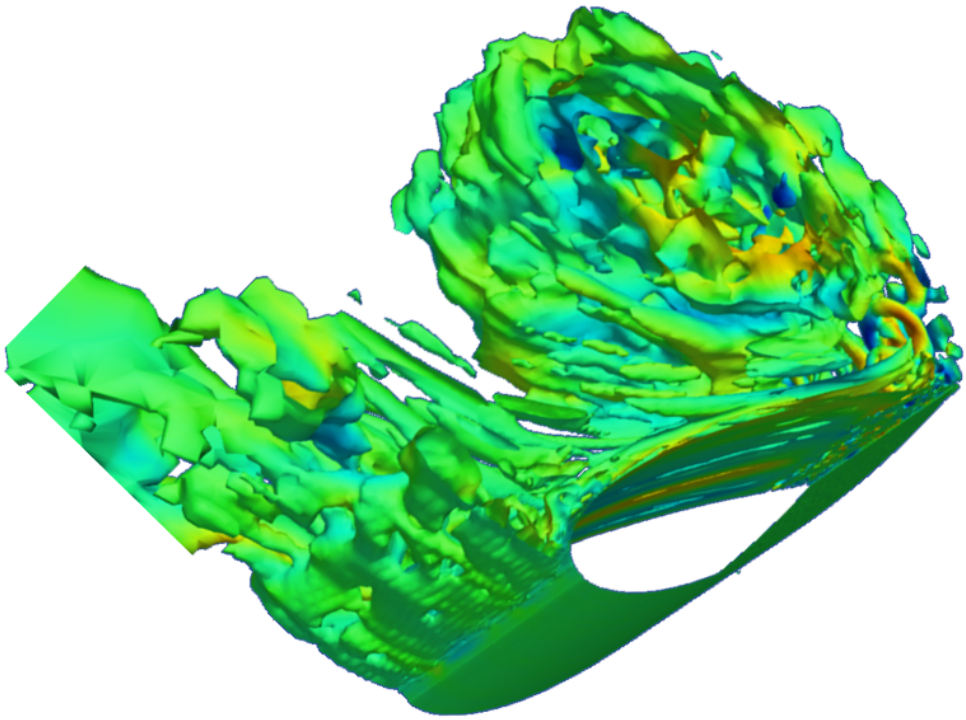

CFD Investigation of Wind-powered Ships under Extreme Condition

Simulations on the NACA-0015 Foil under Deep Stall Condition

Master's thesis in Naval Architecture and Ocean Engineering

HENG ZHU

Department of Mechanics and Maritime Sciences
CHALMERS UNIVERSITY OF TECHNOLOGY
Gothenburg, Sweden 2020

Master's thesis 2020

CFD Investigation of Wind-powered Ships under Extreme Condition

Simulations on the NACA-0015 Foil under Deep Stall Condition

HENG ZHU

CHALMERS
UNIVERSITY OF TECHNOLOGY

Department of Mechanics and Maritime Sciences
Division of Marine Technology
Chalmers University of Technology
Gothenburg, Sweden 2020

CFD Investigation of Wind-powered Ships under Extreme Condition
Simulations on the NACA-0015 Foil under Deep Stall Condition
HENG ZHU

Supervisor: Rickard Bensow, Department of Mechanics and Maritime Sciences
Examiner: Rickard Bensow, Department of Mechanics and Maritime Sciences

Master's Thesis 2020:79
Department of Mechanics and Maritime Sciences
Division of Marine Technology
Chalmers University of Technology
SE-412 96 Gothenburg
Telephone +46 73 629 3274

Cover: 3D flow structures predicted at deep-stall condition of foil NACA-0015. The iso-surface of $Q = 10$ are contoured by velocity in the longitudinal direction.

Typeset in LaTeX
Printed by Chalmers Reproservice
Gothenburg, Sweden 2020

CFD Investigation of Wind-powered Ships under Extreme Condition
Simulations on the NACA-0015 Foil under Deep Stall Condition
HENG ZHU
Department of Mechanics and Maritime Sciences
Chalmers University of Technology

Abstract

This thesis is dedicated to study the loading condition of the rigid wingsails on a ship with wind-assisted propulsion using CFD methods. OpenFOAM is used for the CFD simulations. 2D simulation cases are performed for both low angles of attack and 90 degrees angle of attack conditions. Simulations on a uniform 3D foil with 90 degrees angle of attack conditions are also performed.

Unsteady RANS and DES simulations are carried out to predict the loading condition on a NACA-0015 foil. Under the conditions of low angles of attack, the $k-\omega$ SST model and the $k-\omega$ SST DDES model are used in the simulation. For 90 degrees angle of attack simulation cases, the $k-\omega$ SST model and the $k-\omega$ SST IDDES model are used. The simulation results are compared with experimental data. These simulation cases provide the loading condition on foils and characters of the flow field. The possible causes of error, especially the overestimation of the force coefficients for 90 degrees angle of attack, are discussed.

For the cases of 90 degrees angle of attack, the influence of mesh factors on the simulation results is analyzed, which includes the refinement of profile mesh, structured and unstructured downstream fields, and the ratio between the chord length and the longitudinal length.

A rough prediction of the interaction between two foils is presented as well. Experiences on performing deep stall simulation, and suggestions on wind propulsion from an engineering perspective are also provided.

Keywords: NACA-0015, IDDES, flow separation, deep stall, high Reynolds number.

Acknowledgements

The fourth semester of the Master's program Naval Architecture and Ocean Engineering at the Chalmers University of Technology includes the Master Thesis. This thesis project of CFD simulations on wind propulsion ships under extreme conditions is established by SSPA.

In order to properly finalize this concept, I would like to thank several persons for their time, support, and concern and especially for their following inputs to the project:

- Rickard Bensow from *Chalmers*, for his advice and guidance by supporting my work, especially by utilizing his fluid dynamics background for guiding me on choosing study cases, solving problems of inaccuracy, and checking and approving my thesis.
- Sofia Werner from *SSPA*, for her instructions in the overall concept and working plan of this project, as well as her advice regarding many important details.
- Karolina Malmek from *SSPA*, for helping me with guiding my research direction, collecting critical databases, and providing suggestions from engineering perspective.

Heng Zhu, Gothenburg, June 2020

Contents

List of Figures

List of Tables

1

Introduction

This chapter introduces the research background of this project, the literature review, and how the research is conducted. In the introduction of the research background, the development of wing sails and the advantages and disadvantages of rigid wings are briefly described. In the literature review, wind tunnel tests and CFD simulations of airfoil under extreme conditions, i.e. high angle of attack conditions, are mainly presented.

1.1 Background

In recent decades, the consumption of fossil energy resources has caused significant climate change. In the field of naval architecture, stakeholders are trying to find a new alternative energy plan. Wind-powered ships could be a feasible way to reduce fossil fuel emissions from shipping.

In an ongoing research project, involving Wallenius Marine in cooperation with SSPA, KTH, and Chalmers, a wind-powered car carrier concept is being developed. In this concept, the sails are planned to be very large rigid wings. Under normal operation, the flow over the wings will be attached. In some extreme situations, however, the wings may have a large angle of attack so that the flow is partly or completely de-attached, i.e. stalled. A situation like that can potentially lead to large unsteady forces that may be harmful to the ship in terms of structural integrity and risk of capsizing.

1.1.1 History of wind propulsion

The history of sailing can be traced back to 6000 BC and onwards in Eastern Europe [1]. In the Near East, excavations provide evidence of existing sailing during 6000~4300 BC [2]. The earliest recorded sail in history is a sailboat made in ancient Egypt around 4000 BC [3]. The first ocean-going sailing yacht was produced by Austronesian in present southern China, which led to the expansion across the South Pacific between 3000 and 1500 BC [4]. With the development of sailing technology, seaborne trade was boosted by the Greeks and Phoenicians by around 1200 BC [5]. In the Mediterranean, single-yarded lateen sails arose by around the 100 BC [6]. In the early period, sailing boats could only sail downwind. When BC met AD, the

people from the Malay Archipelago already made large ships and were able to sail against the wind [7].

During the 15th~19th centuries, fore-and-aft sails were invented and developed in Europe, which improved the upwind sailing ability of European vessels [8]. However, sailing depends on the variable weather. As a result, wind power as the primary source of propulsion for ocean-going ships significantly declined after the invention of steamships during the Industrial Revolution [9].

1.1.2 Development of modern wind-powered ships

By the 1920s, few sails were applied on ocean-going ships. However, the development of sails has never stopped [9]. In 1979, oil prices suddenly increased significantly, which is known as the "1979 oil crisis". This event led to the exploration of developments in potential alternative propulsion systems [10]. Sail technology, an ancient means of propulsion, boomed again during that period [11].

Sailing with rigid wingsails, which is known as the wing sail concept, is one form of wind-assisted propulsion. In the 1980s, a number of ships were equipped with rigid sails by Japan Marine Machinery Development Association (JAMDA) [12]. Rather than being the primary source of propulsion, these sails were fitted to ships in order to reduce fuel consumption [9]. JAMDA sails reduced the fuel consumption of up to 30% or more [12]. During that period, another type of rigid sail known as the Walker WingSail, which was estimated to save 15%~20% fuels, was also developed [9]. In 2000, a product carrier with rigid wingsails, which was estimated to save up to 15% of fuel, was designed for the Danish Ministry of Environment and Energy [13].

Other forms of wind-assisted propulsion include kite sails and Flettner rotors. In the 1980s, researchers commissioned by the U.S. government explored the economic feasibility of using wind-assisted propulsion to reduce fuel consumption on the U.S. Merchant Marine [14]. During that time, wind-assisted propulsion facilities as kite sails [15] and Flettner rotors were arisen [16]. In 2007, a series of full-scale tests showed that kites together with conventional engines could save 35% of fuel [17]. If the ships were slowing down by 20%, up to 40% of the fuel consumption could be saved [10].

Although these sails have shown significant energy saving, the research on wind-assisted propulsion sometimes slow down because of the periodic low oil prices [9]. In order to reduce fuel consumption, since the financial crisis in 2008, the cruise speed of many ships has been reduced, so the effect of wind-assisted propulsion on fuel-saving is more obvious [10].

In the meantime, wind propulsion is much more environment-friendly compared with fossil fuels or bio fuels. The worldwide merchant fleet produces more than 3% of the total global carbon emissions [18]. Thus, the application of sail technology is considered to increase in the next few years [10].

1.1.3 Advantages and disadvantages of rigid wingsails

According to subsection 1.1.2, compared with the traditional propulsion approaches, wind-assisted propulsion saves fuel and does less damage to the environment. Nevertheless, wind-assisted propulsion depends on the weather to a certain extent, which makes it not as flexible as traditional propulsion approaches.

Ships with rigid wingsails can not only make use of the wind energy under downwind conditions but also under upwind conditions, which can not be achieved by kite sails. Compared with the Flettner rotors, rigid wingsails hardly need extra power to rotate the wind-assisted facilities. However, as compared in subsection 1.1.2, kite sails can save more fuels, especially when reducing the speed.

In comparison to rigid wingsails, traditional flexible fabric sails have some drawbacks. They are prone to wearing and tearing, must be furled when not in use, and the ropes are easy to get into jam [19]. To overcome these problems, most ships nowadays use rigid wingsails with symmetrical airfoils. NACA-00xx series are usually chosen for the profiles. Asymmetrical airfoils are not common since the wind is from both sides of the vessel, even though it's known that they present better values for the lift force coefficient (C_L), and for the ratio between lift and drag force coefficients (C_L/C_D) [20].

The main advantages of rigid wingsails over the traditional sails are the fact that the rigid wingsails maintain their shape in light winds while traditional sails would collapse, and are more robust to control since there is no rope which could become entangled [21]. Rigid wingsails are considered to be more efficient. This is because modern airfoils provide an increased lift-drag ratio (C_L/C_D) over a conventional fabric sail, which increases the thrust and reduces the overturning moment [20]. This character is more remarkable when navigating downwind. At this point of sailing, soft sails produce thrust entirely by drag, while for rigid wingsails, thrust is obtained from both lift and drag [22]. Other advantages include that rigid wingsails have fewer structures and are easy to design and operate [20].

Though rigid wingsails have quantities of advantages compared with traditional flexible fabric sail, the larger aerodynamic forces acting on the wingsails can compromise the stability of the hull during navigation, especially in unsteady wind conditions [23]. Rigid wingsails will confronted by the vortex induced oscillation problem. Besides, rigid wingsails are more expensive to manufacture.

1.2 Literature survey

1.2.1 Design and optimization of wind-propulsion ships

Wind-propulsion ship design is a kind of systems engineering. The design parameters are coupled, which means that the relationship between them is one of mutual influence, condition, and transformation, presenting great complexity and considerable changeability. For example, if the area of the sail increases, the thrust force but

also the side force will increase, as well as the yaw moment and the heeling moment, therefore also the resistance increases. The designer needs to judge and weigh since both the thrust and the resistance increase [10].

K. Kijima (1975) developed Velocity Prediction Program (VPP) which is a computer program and one of the common approaches in high-performance sailing ships to solve the coupled equations of motion [24]. VPP is based on computational fluid dynamics, experimental fluid dynamics, or analytical formulations. Models of how the aerodynamic and the hydrodynamic forces and moments vary with the key design parameters are used to solve the equations of motion of the ship [25].

J. He et al. (2015) proposed a stability criteria calculation method of sail-assisted ships and introduced a calculation method for the stability parameter to investigate the reasonableness of the sail models. [26].

1.2.2 Experiments and CFD simulations on deep stall foils

In this subsection, several research that are related to this thesis will be summarized. Brief descriptions of research on a flat plate with high angles of attack, wind tunnel tests, and CFD simulations on deep stall foils, improvements on the DES model out of the purpose to predicting the flow field around a foil are presented. Since the research object in this thesis is the NACA-0015 foil, some experiments and CFD simulations on NACA-0015 are also included.

In fluid dynamics, a stall is a reduction in the lift coefficient generated by a foil as the angle of attack increases [27]. Unsteady turbulent flow with separation under a high angle of attack condition is challenging for computational fluid dynamics (CFD). Conventional Reynolds-averaged Navier–Stokes (RANS) approaches do not fit this condition very well since they temporally average large-scale unsteady coherent structures [28].

The aerodynamic studies on wingsails are indeed not numerous especially for foils in case of deep stall [23]. Since in the sense of flow field, a foil at a high angle of attack is similar to a flat plate under the same condition, research on deep stall flat plate are also meaningful. For flat plates, C. P. Jackson (1987) performed 2D simulations on the laminar flow past flat plates aligned over a range of angles to the direction of flow, and analyzed its periodic behavior [29]. C. W. Knisely (1990) did experiments to determine Strouhal numbers for a series of rectangular cylinders with side ratios (B/D) ranging from 0.04 to 1.0 and with angles of attack from 0° to 90° [30]. M. R. Castelli et al. (2012) used the standard $k - \epsilon$ turbulence model to analyze the flow field around a thin flat plate of infinite span inclined at 90° to a fluid stream of infinite extent and underestimated the drag force coefficients [31].

Wind tunnel test is the main research method of experimental aerodynamics. Some research executed wind tunnel tests to study deep stall foils. R. E. Sheldahl et al. (1981) performed wind tunnel experiments at Sandia National Laboratories for a series of NACA foils with angles of attack from 0° to 180°, and presented its

force coefficients [32]. K. W. McAlister (1991) in NASA performed wind tunnel experiments for NACA-0015 foils using a 3D wing model with round sides with angles of attack from 4° to 12° and Reynolds number from 1×10^6 to 1×10^7, and measured its force coefficients, velocity profile in boundary layers and downstream development of the trailing vortex [33]. B. Franck (2008) also conducted wind tunnel experiments for NACA-0015 with angles of attack from 0° to 12° and collected the velocity profile in boundary layers [34].

Though CFD simulations are not as reliable as the wind tunnel tests, it's much cheaper and able to provide more information about the flow fields. In recent years, with the development of computer performance, many CFD simulations have been carried out for deep stall foils. In the mean time, the improvement of the Detached Eddy Simulation model is also in progress. J. A. Ekaterinaris et al. (1998) discussed the impact of the transition from laminar to turbulent flow on the dynamic stall phenomenon and summarized currently available methods for its prediction [35]. S. A. Morton et al. (2005) employed DES97 to simulate a full F/A-18E aircraft experiencing massively separated flow, which had a good agreement with the experiments [36]. A. K. Travin et al. (2006) proposed adjustments of DDES, simulated the massively separated flows over airfoils, and observed that the DDES performs similarly to the original DES97 [37]. N. Durrani et al. (2011) applied both DES97 and DDES for the A-airfoil under the condition of maximum lift force and observed that for the flow with a relatively thick boundary layer and a bland separation at the trailing edge, DES97 has better performance than DDES due to its relatively lower turbulence dissipation levels [38]. F. Bertagnolio (2011) applied the $k-\omega$ SST model to simulate NACA-0015 foil with angles of attack from 4° to 12°, presented the velocity profile in boundary layers, and analyzed the turbulent stress [39]. Y. Yang et al. (2016) applied the high order accuracy schemes to IDDES with different mesh sizes to simulate a deep stall foil (60° angle of attack), compared with RANS and DES results [40]. M. Sato et al. (2017) used the LES model to simulate NACA-0015 foil at Reynolds Number of 1.6×10^6, presented the loading condition, and the velocity profile in boundary layers, and analyzed the transition phenomenon [41]. J. S. Park (2017) used PyFR to simulate unsteady turbulent flow over a NACA-0021 aerofoil in a deep stall condition, using a wall-resolved implicit large-eddy simulation (ILES) approach, and indicated that the ration between the chord length and the span length had a deep influence on the simulations for a deep stall foil [42].

1.3 Thesis structure

1.3.1 Aim and motivation

From the engineering perspective, although wind-assisted propulsion cannot completely replace the engine, the energy saving is considerable, as subsection 1.1.2 presents. Since fossil fuels are limited and the international community pays more and more attention to environmental impacts, wind-assisted propulsion will possibly be applied widely in the future. Thus, it's meaningful and constructive to research into wind propulsion.

For an ocean-going ship with wind-assisted propulsion systems, one of the challenging conditions it will confront is varying wind directions including headwind, beam wind, and whirlwind. The main goal of this project is to study the most severe conditions and describe the dynamic forces acting on the rigid wingsails, identifying the most hazardous behavior for the ship.

Under these conditions, the angles of attack of the wingsails might be very large. Thus the foil can be deep stalled. Since unsteady turbulent flow with separation, which is a challenging regime for computational fluid dynamics, will happen under the extreme conditions, this project will also explore methods for simulating deep stall foils.

1.3.2 Methodology

This project begins with the collection of experimental and CFD simulation data of the NACA-0015 foil. These data are used to compare with the CFD simulation results in the following steps. Since before using CFD methods to give prediction for a rigid wingsail, it's important to make sure this simulation gives an accurate estimation.

The simulations with 2D low angles of attack cases will be presented first, following with 2D and 3D simulations on 90° cases. For the 3D simulations, some preliminary cases are first made for finding defects in the simulation process. Then a final case is carried out. In the last phase, mesh analysis, comparison between different schemes and solvers are also carried out in order to make the simulation results more reasonable and accurate. All the results are compared with the experimental data.

Typically, more than one foil are installed on a ship. Therefore, it's important to study the interaction between foils. A 2D simulation for two foils is made to give a rough prediction on this problem.

The initial plan of this project included simulation for a realistic foil model and stability calculation for the ship. However, some unexpected problems occurred. A lot of time was spent on the 3D simulation for a uniform foil to make sure that with the DES simulation approach, the complex flows under deep stall can be reasonably predicted. Unfortunately, time was not enough for these works.

Figure 1.1 shows the process of this project. The process in dashed boxes were included in the initial plan but not put into effect.

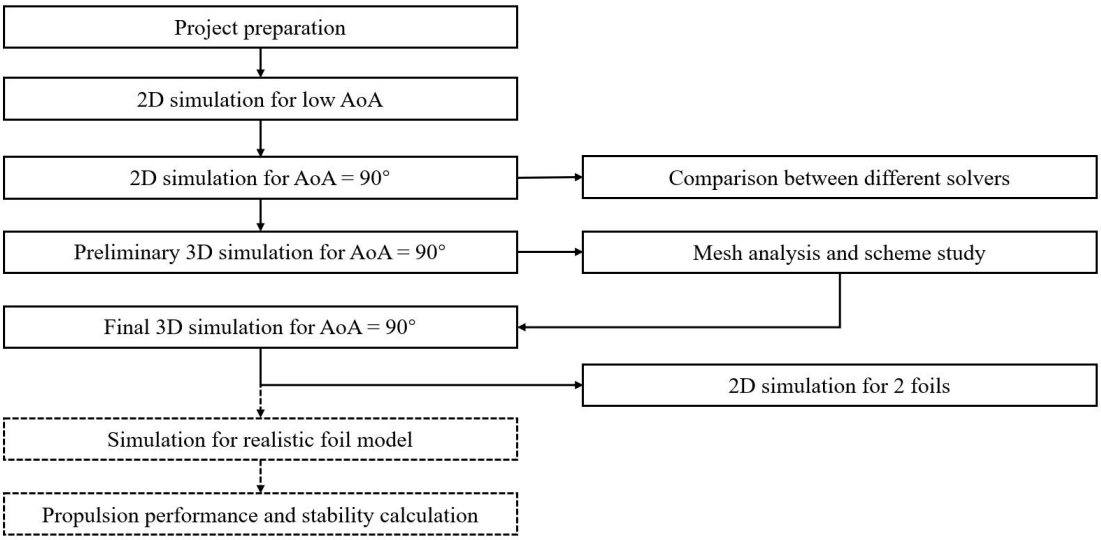

Figure 1.1: Methodology of this project.

1.3.3 Specification of issues under investigation

As a result of this project, the following questions will be answered:

1. Whether the selected turbulence models give accurate results.
2. What are the main difficulties in CFD simulation on deep stall foils.
3. How much propulsive force can be generated by the foils under conditions that were calculated.
4. What problems may possibly happen when several foils are operating together.

Some detailed CFD issues will also be deeply discussed in this project like a comparison between RANS and DES simulation and mesh size analysis. A brief description of the influence on hull stability from the rigid wingsails would be provided in this project in the initial plan. However, when performing simulations on a uniform 3D foil, the simulation always overestimates the force coefficients due to some unexpected reasons, which will be discussed in chapter 4. Thus, more time is devoted to exploring the causes of this overestimation.

2

Theory and methods

In this chapter, the methodology and the theory that it is based on will be presented.

In the general process, to compute the loading condition on sails, 3D models of the sails are typically tested with EFD or CFD [43]. In the present project, the task is to investigate these extreme conditions, i.e. conditions with 90° angle of attack (AoA), using CFD. As the flow is largely separated, unsteady scale-resolving simulations need to be performed. The conventional unsteady RANS models do not fit this condition very well since they average large-scale unsteady coherent structures [28]. For LES or DNS approaches, the effort in calculation is too large and the requirement for computers is too high [44]. Thus, the DES-type model, which combines RANS and LES is chosen as the turbulence model. Simulations will be performed in OpenFOAM. The calculation mesh will be generated by Pointwise software and the color plot of the CFD results will be provided by ParaView software.

This project can be divided into two stages: 2D simulations and 3D simulations. In both of the two stages, the simulations will be performed using OpenFOAM. During 2D simulations, both the RANS model (mainly $k-\omega$ SST model) and DES (mainly SST-IDDES model) will be used. The results from the 2D simulations will be compared with experimental data and results from available research, to ensure the performance of accuracy. During the 3D simulations, the DES model will be used to analyze the 3D rigid wingsails. The study case will simulate the real condition which the ship will encounter. Therefore, the condition of simulation cases will be more practical including the downwind and extreme conditions.

2.1 Loading condition of sails

The aim of this project is to analyze the loading condition of wingsails on a ship. So, the theory and calculating methods about loading conditions on sails will be presented in this section.

In order to compute the aerodynamic forces, the apparent wind experienced by the ship must be computed as a vectorial sum of the true wind and wind due to the ship speed ($-V$). Figure 2.1 shows the wind velocity triangle. The apparent wind speed (AWS) and direction (AWA) vary with the height because the true wind speed

(TWS) is increasing with the height.

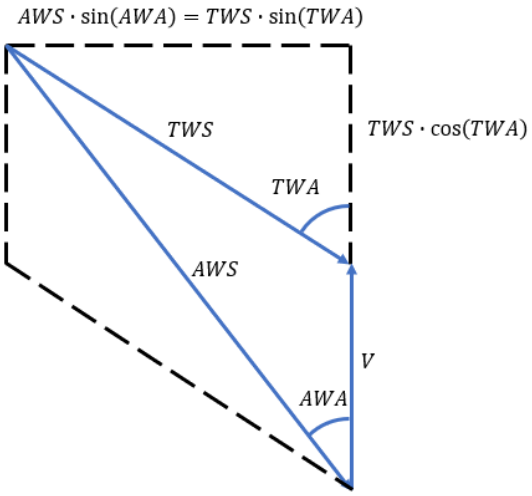

Figure 2.1: Wind velocity triangle.

TWS is computed from [10]

$$TWS = \frac{u*}{k} \log(\frac{z}{z_0}), \tag{2.1}$$

where $u*$ is the shear velocity which is computed by solving equation 2.1 for a given true wind speed at $z = 10$ m, while z_0 is the water roughness height, which is computed with [45]

$$z_0 = 5 \cdot 10^{-5} \frac{(TWS|_{10})^2}{g}, \tag{2.2}$$

in which $TWS|_{10}$ is the true wind speed at $z = 10$ m, g is the gravity acceleration.

At each horizontal section along the height, the apparent wind speed is computed by

$$AWS = \sqrt{V^2 + TWS^2 + 2V \cdot TWS \cos TWA}, \tag{2.3}$$

$$AWA = \arctan(\frac{TWS \sin TWA}{V + TWS \cos TWA}). \tag{2.4}$$

The wingsail trim with the maximum thrust is not regarded as the best, because the associated large side force will increase the hull resistance. Assuming that a ship sails at constant cruising speed, the increase of the hull resistance must be balanced

by the increase of propeller thrust. Therefore, the optimization goal of wingsail trim must be the minimum propeller thrust at the chosen cruising speed [10].

In order to model the forces and moments generated by wingsails with different trims and section shapes, firstly the force conditions are computed by the CFD process, and then these are integrated into the span-wise direction based on the chosen horizontal section. A correction needs to be made in order to take into account the non-infinite aspect ration of the wingsails. When sailing at large TWA, the drag generated by the wingsails contributes positively to the wingsails thrust, so the stalled conditions also need to be considered [10].

2.2 Turbulence models

The $k-\omega$ SST model is used for the RANS simulations and RANS region in DES simulations. DES model is applied to study the flow separation.

2.2.1 $k-\omega$ SST

The turbulence model, $k-\omega$ Shear Stress Transport (SST), is a two equation model one for the turbulence kinetic energy, k, and another equation for turbulence specific dissipation rate, ω [46][47].

The turbulence specific dissipation rate equation is given by equation 2.5, and the turbulence kinetic energy by equation 2.6,

$$\frac{\mathrm{D}}{\mathrm{D}t}(\rho\omega) = \nabla\cdot(\rho D_\omega \nabla\omega) + \frac{\rho\gamma G}{\nu} - \frac{2}{3}\rho\gamma\omega(\nabla\cdot\mathbf{u}) - \rho\beta\omega^2 - \rho(F_1-1)CD_{k\omega} + S_\omega, \quad (2.5)$$

$$\frac{\mathrm{D}}{\mathrm{D}t}(\rho k) = \nabla\cdot(\rho D_k \nabla k) + \rho G - \frac{2}{3}\rho k(\nabla\cdot\mathbf{u}) - \rho\beta^*\omega k + S_k. \quad (2.6)$$

The turbulence viscosity is obtained using

$$\nu_t = a_1 \frac{k}{\max(a_1\omega, b_1 F_{33}\mathbf{S})}. \quad (2.7)$$

Table 2.1 shows the default model coefficients in OpenFOAM [48].

Table 2.1: Default model coefficients in OpenFOAM.

α_{k1}	α_{k2}	$\alpha_{\omega1}$	$\alpha_{\omega2}$	β_1	β_2	γ_1	γ_2	$\beta*$	a_1	b_1	c_1
0.85	1.0	0.5	0.856	0.075	0.0828	5/9	0.44	0.09	0.31	1.0	10.0

The $k-\omega$ SST model can overcome the deficiencies of the standard $k-\omega$ model with respect to dependency on the freestream values of k and ω. The $k-\omega$ SST model is also able to capture flow separation.

For isotropic turbulence, the turbulence kinetic energy can be estimated by

$$k = \frac{3}{2}(I\,|\mathbf{u}_{ref}|)^2, \tag{2.8}$$

where I is the intensity, and $\mathbf{u}_{ref}$ is a reference velocity. The turbulence specific dissipation rate follows as

$$\omega = \frac{k^{0.5}}{C_\mu^{0.5} L}, \tag{2.9}$$

where C_μ is a constant equal to 0.09, and L a reference length scale.

2.2.2 DES

Detached Eddy Simulation (DES) relates to a hybrid RANS-LES approach to turbulence modeling, aiming to alleviate the costly near-wall meshing requirements imposed by LES.

The aim is to treat the boundary layer with RANS and capture the outer detached eddies with LES. Since the flow in the boundary layer will be strongly influenced by the unsteady LES in the outer region, the flow in the boundary layer will also be unsteady. Hence the boundary layer is treated with unsteady RANS (URANS). The DES was originally developed for wings at very high angles of attack [49].

For the $k-\omega$ SST DES model, the length scale, $\widetilde{d}$, is given by

$$\widetilde{d} = \min(C_{DES}\Delta, \frac{\sqrt{k}}{\beta * \omega}). \tag{2.10}$$

For the $k-\omega$ SST Delayed Detached Eddy Simulation (DDES) model and $k-\omega$ SST Improved Delayed Detached Eddy Simulation (IDDES) model, the model equations are the same as used by the DES variant of the model, with a different approximation for $\widetilde{d}$ [50].

The DDES length scale is calculated by

$$
\begin{aligned}
l_{DDES} &= l_{RANS} - f_d \max(0, l_{RANS} - l_{LES}), \\
l_{LES} &= C_{DES} h_{\max}, \\
l_{RANS} &= \frac{\sqrt{k}}{C_\mu \omega}, \\
C_{DES} &= C_{DES1} \cdot F_1 + C_{DES2} \cdot (1 - F_1).
\end{aligned}
\tag{2.11}
$$

where h_{max} is the maximum edge length of the cell, and the empirical delay function f_d involved in the DDES approach reads as equation 2.13 and 2.14. The value h_{max} can also be replaced by other calculation methods which will be described and compared in section 4.1.2 and 4.1.2. The constant C_{DES1} and C_{DES2} can be found in table 2.2.

F_1 and F_2 denote the SST blending functions [47], which read as

$$
\begin{aligned}
F_1 &= \tanh\left(arg_1^4\right), \\
arg_1^4 &= \min(\max(\frac{\sqrt{k}}{C_\mu \omega d_w}, \frac{500\nu}{d_w^2 \omega}), \frac{4\rho\sigma_{\omega 2} k}{CD_{k\omega} d_w^2}), \\
CD_{k\omega} &= \max(2\sigma_{\omega 2} \frac{\nabla k \cdot \nabla \omega}{\omega}), \\
F_2 &= \tanh\left(arg_2^2\right), \\
arg_2^2 &= \max(\frac{2\sqrt{k}}{C_\mu}, \frac{500\nu}{d_w^2 \omega}).
\end{aligned}
\tag{2.12}
$$

So the DES model coefficient C_{DES} in $k-\omega$ SST DDES model is 0.82 [51],

$$
f_d = 1 - \tanh\left[\left(C_{d1} r_d\right)^{C_{d2}}\right], \tag{2.13}
$$

$$
r_d = \frac{\nu_t + \nu}{\kappa^2 d_w^2 \sqrt{0.5 \cdot (S^2 + \Omega^2)}}, \tag{2.14}
$$

where S is the magnitude of the strain rate tensor and Ω is the magnitude of vorticity tensor. The model constants read as table 2.2.

Table 2.2: DDES model constants.

C_μ	κ	a_1	C_{DES1}	C_{DES2}	C_{d1}	C_{d2}
0.09	0.41	0.31	0.78	0.61	20	3

The IDDES length scale is calculated as

$$l_{IDDES} = \widetilde{f}_d \cdot (1 + f_e) \cdot l_{RANS} + (1 - \widetilde{f}_d) \cdot l_{LES}. \tag{2.15}$$

The LES length-scale Δ is defined as

$$\Delta = min[C_w max(d_w, h_{max}), h_{max}]. \tag{2.16}$$

The empirical blending function $\widetilde{f}_d$ in equation 2.15 is computed with the use of

$$\begin{aligned}
\widetilde{f}_d &= max[(1 - f_{dt}), f_b], \\
f_{dt} &= 1 - \tanh\left[(C_{dt1} r_d t)^{C_{dt2}}\right], \\
r_d &= \frac{\nu_t}{\kappa^2 d_w^2 \sqrt{0.5 \cdot (S^2 + \Omega^2)}}, \\
f_b &= min[2 \exp -9\alpha^2, 1.0], \\
\alpha &= 0.25 - d_w / h_{max}.
\end{aligned} \tag{2.17}$$

In the simplified version of the IDDES model, the elevating function f_e is set to be zero.

In RANS all turbulent scales are modeled, while in LES, only small, isotropic turbulent scales are modeled, so it will be more accurate. However, LES is very much more expensive than RANS in the boundary layer [44]. If all the domain is using the LES model, the mesh at the boundary layer need to be refined, then the simulation case will be more time-consuming. Thus, the pure LES model is not applied in this project.

2.3 Algorithms

In this project, OpenFOAM is used for CFD simulations. SIMPLE and PIMPLE algorithms are separately used for steady and unsteady states.

2.3.1 OpenFOAM

OpenFOAM is a free, open-source CFD software package. It has a large user base across most areas of engineering and science, from both commercial and academic organizations. OpenFOAM is one of the first important scientific computing software packages written in C++, and has an extensive range of features to solve problems from complex fluid flows involving chemical reactions, turbulence and heat transfer, to solid dynamics and electromagnetics [48].

The advantages of OpenFOAM compared with other CFD softwares include user-friendly partial differential equation description syntax, ability to process unstructured polyhedral meshes, fully documented source code, and no license cost.

2.3.2 SIMPLE and PIMPLE algorithms

L. S. Caretto et al. (1972) put forward the SIMPLE algorithm which is short for Semi-Implicit Method for Pressure Linked Equations algorithm [52]. Figure 2.2 shows the 2D SIMPLE algorithm without under-relaxation [53]. An approximation of the velocity field is obtained by solving the momentum equation. The pressure gradient term is calculated using the pressure distribution from the previous iteration or an initial guess. The equation is under-relaxed in an implicit manner with the velocity under-relaxation factor α_U. The pressure equation is formulated and solved in order to obtain the new pressure distribution [52].

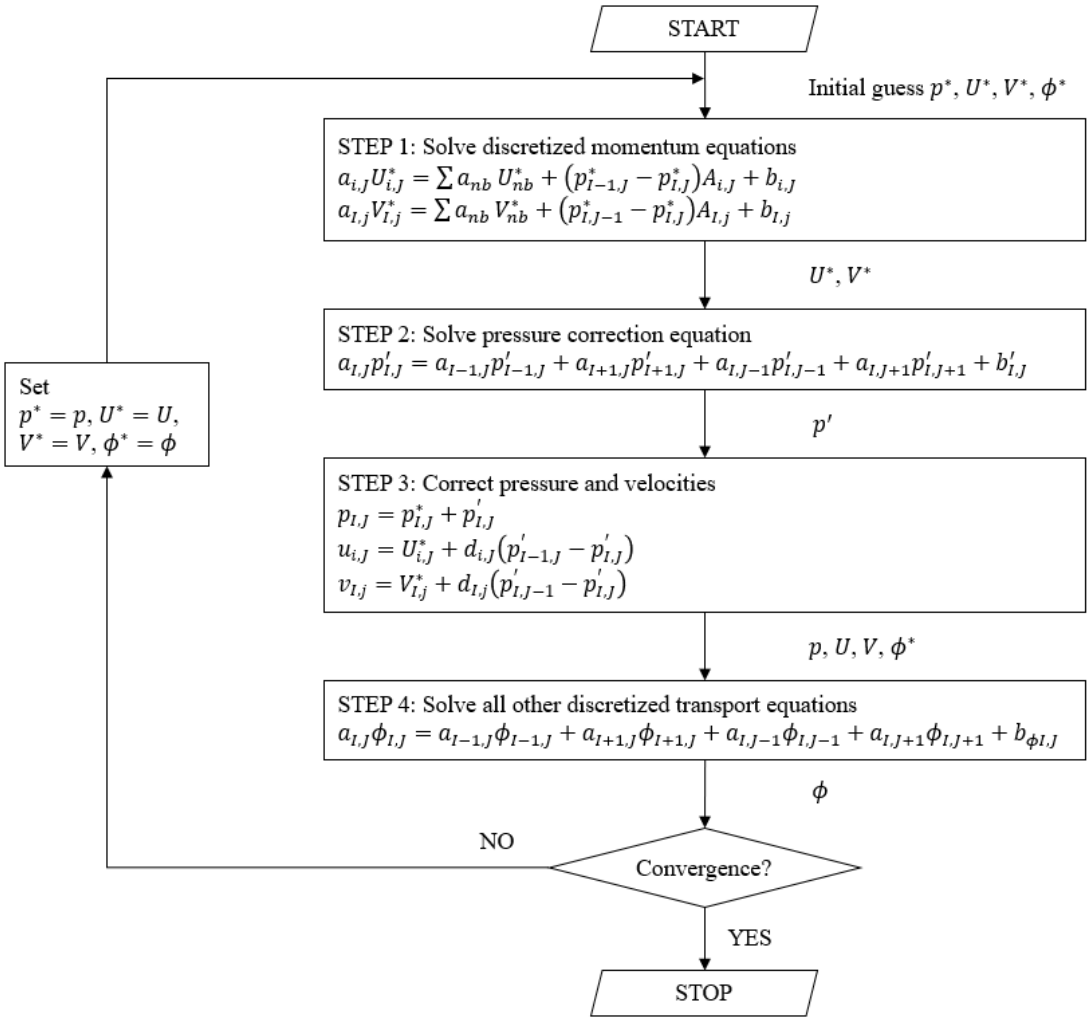

Figure 2.2: The SIMPLE algorithm.

R. I. Issa (1986) put forward the PISO algorithm which is short for Pressure Implicit with Splitting of Operators algorithm [54]. It is a pressure–velocity calculation procedure developed originally for non-iterative computation of unsteady compressible flows. Figure 2.3 shows the 2D PISO algorithm. PISO involves one predictor step and two corrector steps and may be seen as an extension of SIMPLE, with a further corrector step to enhance it [53]. The PISO algorithm solves the pressure correction equation twice so the method requires additional storage for calculating the source term of the second pressure correction equation.

Although this method implies a considerable increase in the computational effort it has been found to be efficient and fast [53].

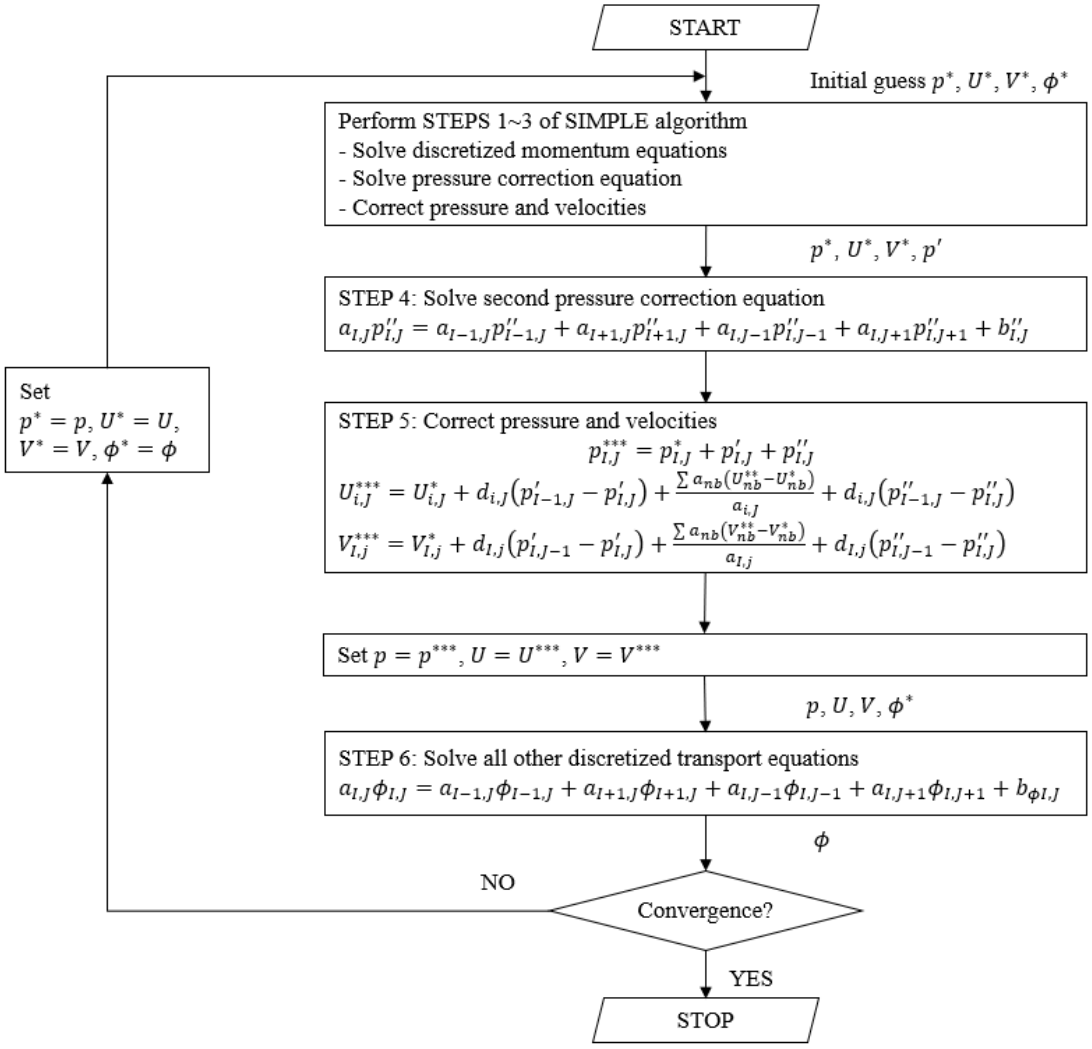

Figure 2.3: The PISO algorithm.

PIMPLE algorithm combines the PISO and SIMPLE algorithms. For the PIMPLE algorithm, outer correctors are the iterations, and once converged will move on to the next time step until the solution is complete.

2.4 Mesh generation

In this project, the simulation cases are based on NACA-0015 foil. The numerical meshes are generated by Pointwise software.

2.4.1 NACA series

NACA airfoil is a series of airfoils developed by the National Advisory Committee for Aeronautics (NACA). The code of each airfoil is composed of four letters "NACA" and a series of numbers. The exact shape of the airfoil can be obtained

by substituting the geometric parameters described by the numbers into a specific equation.

The first number of the code represents the percentage of maximum curvature to chord length. The second number represents the distance between the maximum camber and the leading edge of the wing, which accounts for a few tenths of the chord length. The last two digits represent the maximum wing thickness as a percentage of chord length [55].

Equation 2.18 is the equation for a symmetrical 4-digit NACA airfoil [56],

$$y_t = 5t[0.2969\sqrt{x} - 0.1260x - 0.3516x^2 + 0.2843x^3 - 0.1015x^4], \tag{2.18}$$

where x is the position along the chord from 0 to 1.00 (0 to 100%), y_t is the half-thickness at a given value of x, t is the maximum thickness as a fraction of the chord.

For all the simulations in this thesis, the foil is chosen to be NACA-0015. It's a symmetric foil with the maximum thickness as 15% of the chord length at 30% chord. The data source is UIUC Airfoil Coordinates Database Source [57]. To get a smooth geometry shape of the toil, quadratic interpolation is applied. Figure 2.4 shows the geometry shape of NACA-0015 foil.

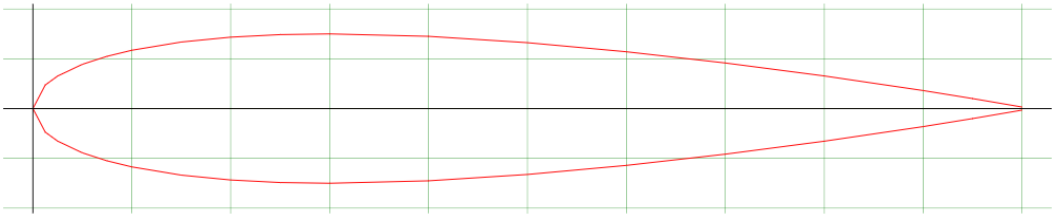

Figure 2.4: Geometry shape of a NACA-0015 foil.

2.4.2 Pointwise

Pointwise, as a software system, is used for generating calculation meshes in this project. Pointwise combines the expertise and history of grid generation embedded in Gridgen with more modern software engineering and graphical interface to make grid generation as simple as possible [58].

2.4.3 Structured and unstructured mesh

Identified by regular connectivity, the structured mesh has two possible cell choices: 2D quadrilateral and 3D hexahedron. Unstructured meshes usually use triangles in 2D and tetrahedrons in 3D, although quadrangles and hexahedrons may also exist [59].

Compared with unstructured meshes, structured meshes have some advantages. Unstructured and hybrid meshing algorithms are highly automated. On the other hand, structured meshing typically allows the users to better control of interior node locations and sizes. Besides, well solved structured grids are generally aligned in the flow direction leading to more accurate results and better convergence in CFD solvers [60].

3

Low AoA simulations

The aim of this project is to investigate the prediction accuracy of high AoA conditions, but the experimental data for NACA-0015 foils with 90° AoA is rare. Nevertheless, for low AoA conditions, there are quantities of experimental data. Thus, it's still necessary to perform a series of low AoA simulations to verify the choice of turbulence model and other simulation settings such as numerical schemes and solvers.

Table 3.1 lists the 2D simulation cases with low AoA that are performed to compare with experimental data and CFD results from other research. Table 3.2 lists the extra 2D simulation cases with low AoA that are performed in order to study the effects of AoA on the flow field and simulation accuracy. The results of the extra cases will be discussed in section 3.3.

Table 3.1: List of 2D simulation cases under low AoA that compared with experimental data.

AoA / °	Re	Steady RANS	Unsteady RANS	DES	DDES	IDDES
0	1e6	√				
4	2.85e6	√				
8.13	1.6e6	√	√	√	√	√
12	2.85e6	√	√		√	

Table 3.2: List of extra 2D simulation cases under low AoA.

AoA / °	Re	Steady RANS	Unsteady RANS	DES	DDES	IDDES
8	1e7	√	√		√	
10	1e7	√	√		√	
12	1e7	√	√		√	
14	1e7	√	√		√	
16	1e7	√	√		√	
18	1e7	√	√		√	

The experimental data of force coefficients is from a series of wind tunnel tests

executed by R. E. Sheldahl et al. (1981) [32], which provides the force coefficients of NACA-0015 foil at AoA from 0° to 180°.

The 0° case is carried out to check whether the simulation provides results with $C_L = 0$. C_D is also compared with the experimental data from wind tunnel tests.

The 4° case and 12° case are carried out to compare the force coefficients, velocity profile, and pressure distribution with experimental data and RANS ($k - \omega$ SST) simulation results. The reference data is from wind tunnel experiments and CFD simulations using the $k - \omega$ SST model performed by F. Bertagnolio (2011) [39].

The 8.13° case is carried out to compare the force coefficients, velocity profile, and pressure distribution with experimental data and LES simulation results. The experimental data is from wind tunnel tests executed by F. Bertagnolio (2008) [34]. The CFD simulation results are from LES simulations performed by M. Sato et al. (2017) [41].

In reality, the foils on ships will work under very high Reynolds numbers which is around 15 million, so when selecting the reference data, data with as high as possible Reynolds numbers are put into use.

3.1 Steady simulations

The simulation begins with steady state. Four cases are carried out as table 3.1 shows. The steady state simulations use the $k - \omega$ SST model and the SIMPLE algorithm.

The domain needs to be large enough to produce reasonable results and make the iteration stable. For the simulations in this project, the chord length of the foil is set to be 1 m. The domain size is 26 m $\times$ 20 m. This size of the domain is also applied for extreme condition simulations in chapter 4.

The numerical mesh of the 12° simulation cases are shown as figure 3.1. The boundary layer and the nearby region is structured, while for the outer region, an unstructured mesh is used to reduce the total number of cells. The meshes used for 0°, 4°, and 8.13° are generated in a similar way.

The total number of cells for these low angles of attack cases is around 50,000. The number of cells around the foil, i.e. the surface mesh, is 1,000. The y^+ at wall is kept to be less than 1.

3.1.1 Domains and meshes

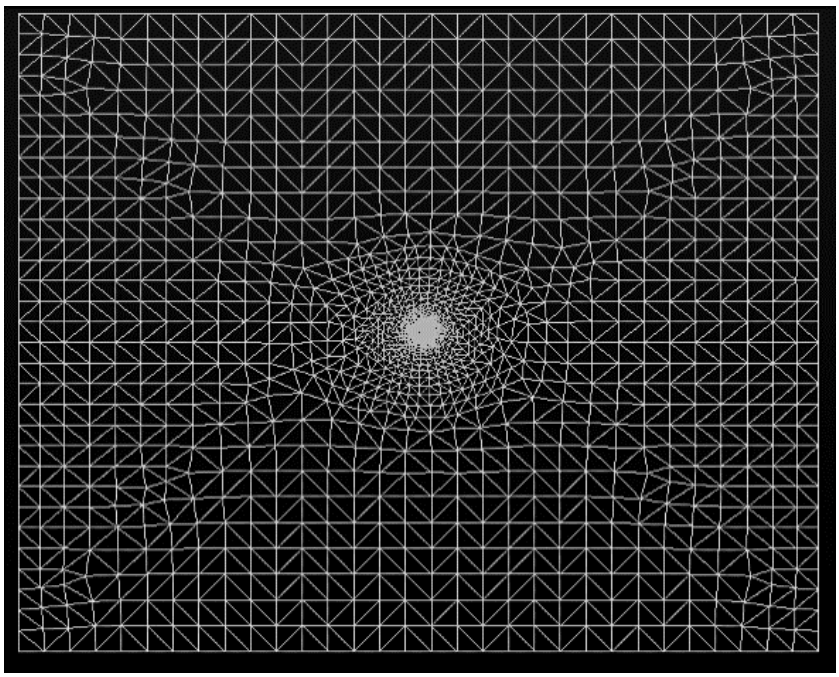

(a) Entire domain.

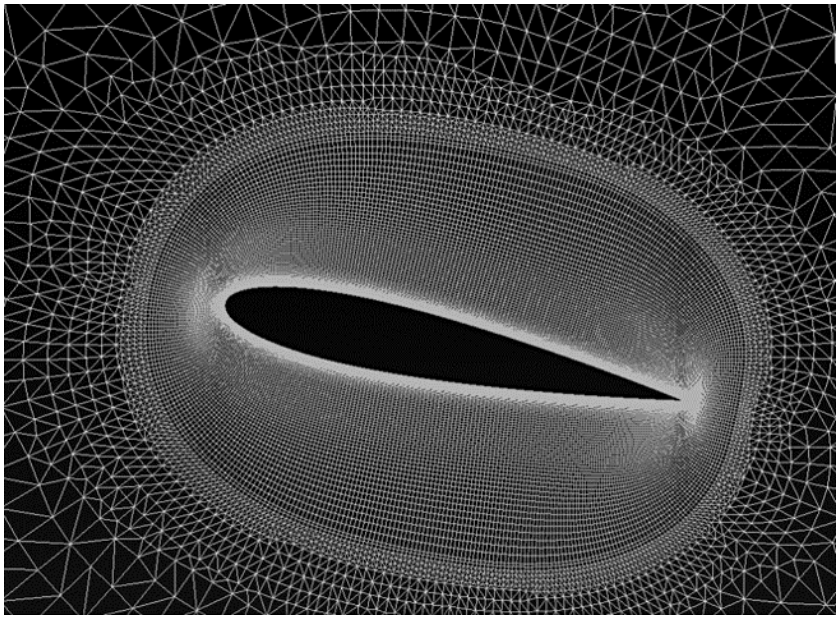

(b) Zoom close to the foil.

Figure 3.1: Numerical mesh, 2D simulations with AoA as 12°.

3.1.2 Boundary conditions

Table 3.3 shows the boundary condition settings of 2D cases. These settings are not only used for the low angle of attack simulations but also for 2D extreme condition simulations. Since it's a 2D simulation, the front and back panel is set to be empty.

Table 3.3: Boundary condition settings, 2D simulations.

	Foil	Front and Back	Top and Bottom	Inlet	Outlet
P	zeroGradient	empty	zeroGradient	zeroGradient	fixedValue uniform 0
U	fixedValue uniform (0 0 0)	empty	slip	fixedValue uniform (10 0 0)	zeroGradient
k	fixedValue uniform 0	empty	slip	fixedValue uniform 0.047633	inletOutlet uniform 0.047633
omega	omegaWallFunction	empty	slip	fixedValue uniform 264.63	inletOutlet uniform 264.63
nut	nutkWallFunction	empty	slip	calculated	calculated

3.1.3 Simulation results

Table 3.4 shows force coefficients from the low angles of attack steady state RANS simulation cases. Figure 3.2 is the bar chart that shows the difference between the predicted force coefficients, C_L and C_D compared to the experimental data.

Simulation results of the lift force coefficients, C_L, fit the experimental data very well, while for the drag force coefficients, C_D, they have a discrepancy from experimental data. It is because the absolute value of drag force at low AoA is quite minor compared with the lift force, so the relative error becomes large, even if the absolute difference is not so large.

Table 3.4: Force coefficients, 2D low-AoA steady-state simulations.

AoA		Experimental data	Steady RANS simulation	Difference
0°	C_L	0.0000	0.0001	-
	C_D	0.0074	0.0122	64.865%
4°	C_L	0.4400	0.4396	-0.091%
	C_D	0.0077	0.0112	45.172%
8.13°	C_L	0.8788	0.8790	0.024%
	C_D	0.0117	0.0153	30.951%
12°	C_L	1.1485	1.2026	4.709%
	C_D	0.0154	0.0251	63.075%

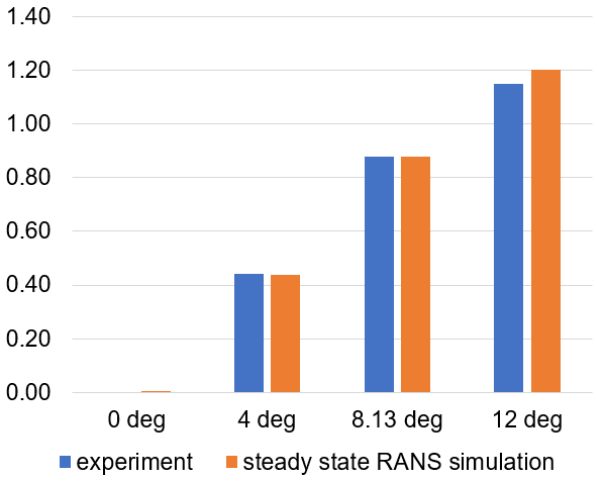

(a) C_L

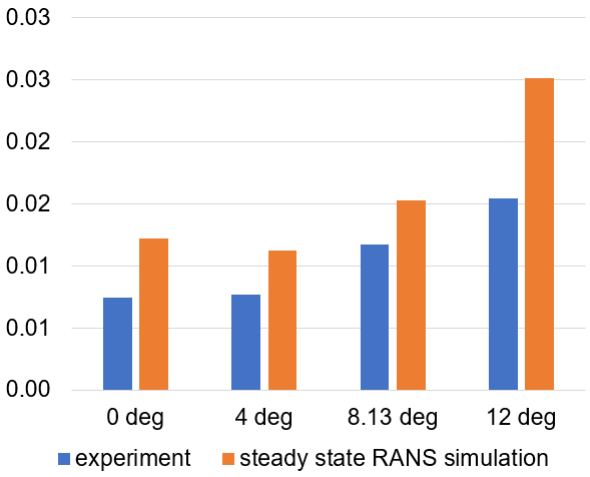

(b) C_D

Figure 3.2: Difference of the force coefficients from the experimental data, 2D low-AoA steady-state simulations.

Figure 3.3 shows the pressure (p/ρ) distribution around the foil from 2D steady RANS simulation at low AoA. There are two high-pressure areas at the leading edge and the trailing edge when the angle of attack is 0°, and the low-pressure areas are distributed on both sides of the foil, which can be found in figure 3.3. With the increase of the angle of attack, the distribution of high-pressure areas and low-pressure areas changes. When the angle of attack is 12°, the main high-pressure area and low-pressure area appear in the pressure side and suction side near the leading edge respectively, which results in the lift force.

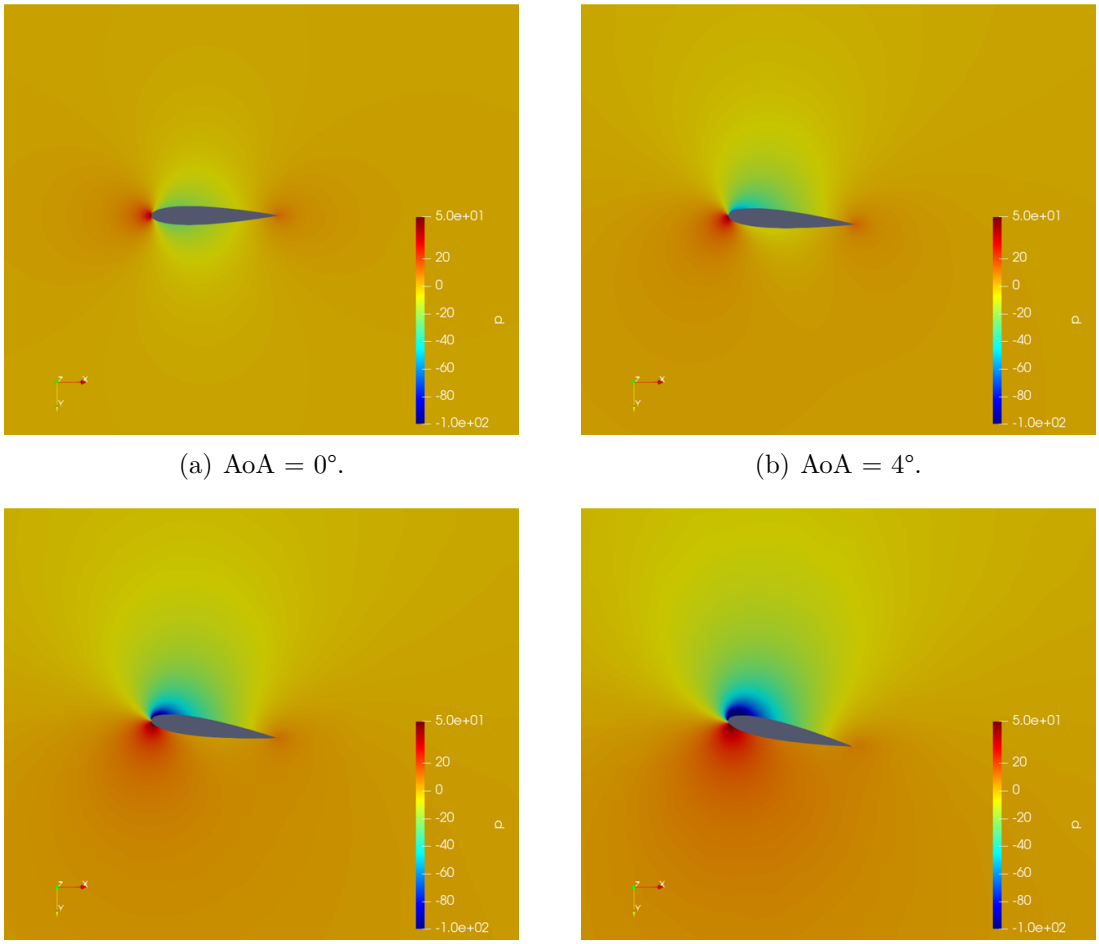

(a) AoA = 0°.

(b) AoA = 4°.

(c) AoA = 8.13°.

(d) AoA = 12°.

Figure 3.3: Pressure (p/ρ) distribution, 2D low-AoA steady-state simulations.

3.2 Unsteady simulations

The unsteady simulations are carried out by using both the URANS model and the DES model. The aim of the unsteady simulations are to test if the unsteady character will have a significant influence on the loading condition when the angle of attack is low. In contrast to the extreme condition, much more reference data about the low angle of attack conditions has been provided in other related studies. Thus, the research on the unsteady state in this stage is meaningful.

3.2.1 URANS simulation

For the URANS simulation, the $k-\omega$ SST model is still applied. The PIMPLE algorithm is used to simulate the unsteady states.

Table 3.5 in the subsection 4.1.2 shows the force coefficients from the unsteady simulations and the relative difference from the experimental data. Compared with

the steady state results in table 3.4, the difference is not obvious in the sense of the force coefficients, especially under the 8.13° condition.

Figure 3.4 shows the pressure distribution along the foil from URANS simulation at 8.13° angle of attack, compared with the experimental data [34]. Since the pressure does not show much fluctuation, here only the mean values are presented. It can be seen that the predicted pressure distribution does not show much difference from the experimental data. Therefore, the results from the low angle of attack simulations can be considered reasonable.

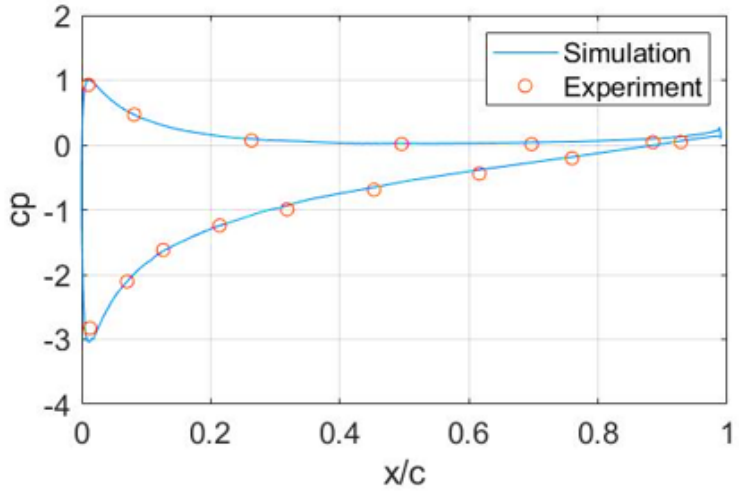

Figure 3.4: Predicted pressure coefficients along the foil.

3.2.2 DES simulation

The DES model splits the domain into a RANS region and an LES region to make full use of the advantages of the two models. All the boundary layers need to be in the RANS region, and the large eddy vortex needs to be in the LES region. The URANS simulation results provide a prediction of the thickness of the boundary layers.

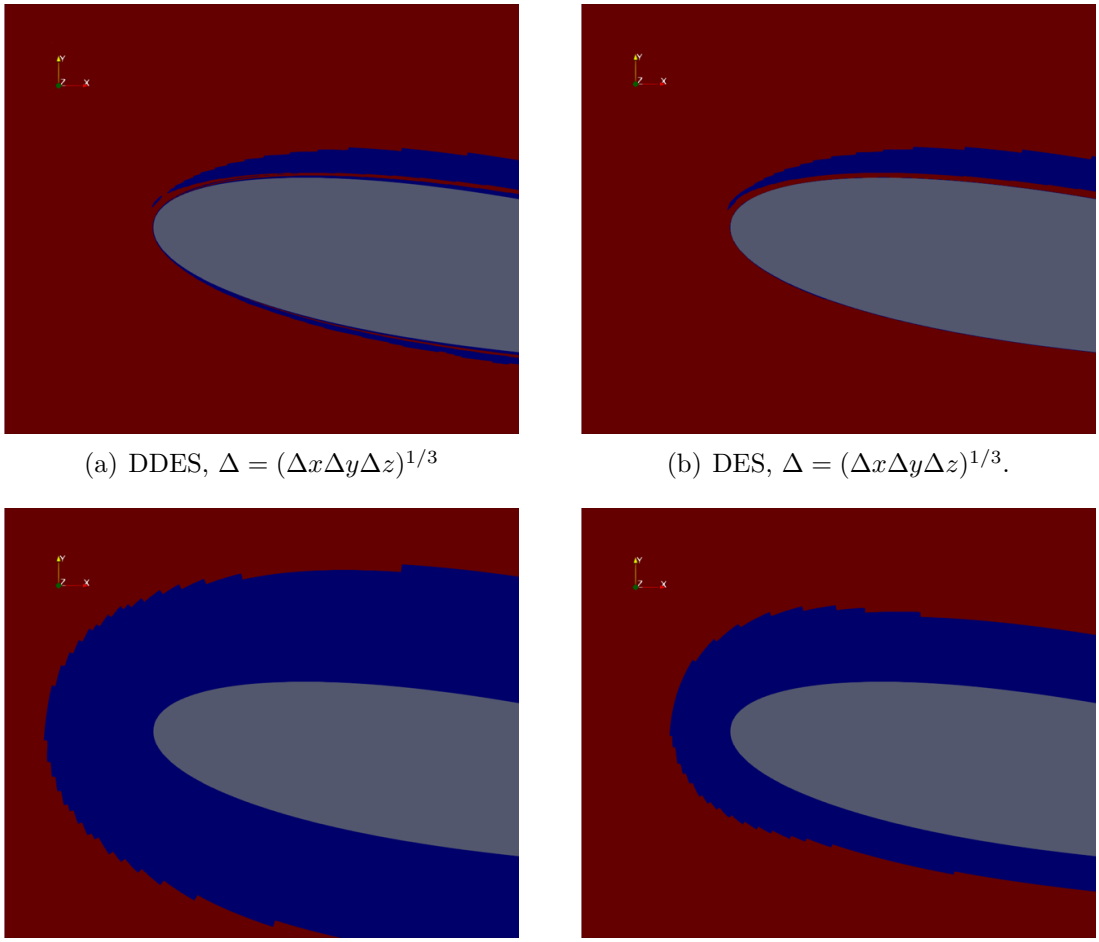

(a) DDES, $\Delta = (\Delta x \Delta y \Delta z)^{1/3}$

(b) DES, $\Delta = (\Delta x \Delta y \Delta z)^{1/3}$.

(c) IDDES.

(d) DDES, $\Delta = max(\Delta x, \Delta y, \Delta z)$.

Figure 3.5: Comparison of DES field between different DES models and DES delta calculating methods at leading edge, low AoA.

There are several options of the DES model, and several methods to calculate the LES length-scale delta, which are compared in Figure 3.5 and figure 3.6. In these figures, the DES field from different DES models and the DES delta calculating methods are shown. The RANS region is in blue; the LES region is in red.

As shown in figure 3.5 and figure 3.6, DES model and LES length-scale delta calculating method $\Delta = \sqrt[3]{\Delta x \Delta y \Delta z}$ allocate too little domain into the RANS region. In the meantime, some LES region is mixed up with the RANS region in the boundary layer, so that not all the boundary layer is covered, especially at the trailing edge. On the other hand, too much domain is allocated into the RANS region when the IDDES model is applied, so the flow separation may not be well predicted.

DDES with $\Delta = max(\Delta x, \Delta y, \Delta z)$ is used for low AoA cases, and IDDES is used for high AoA cases.

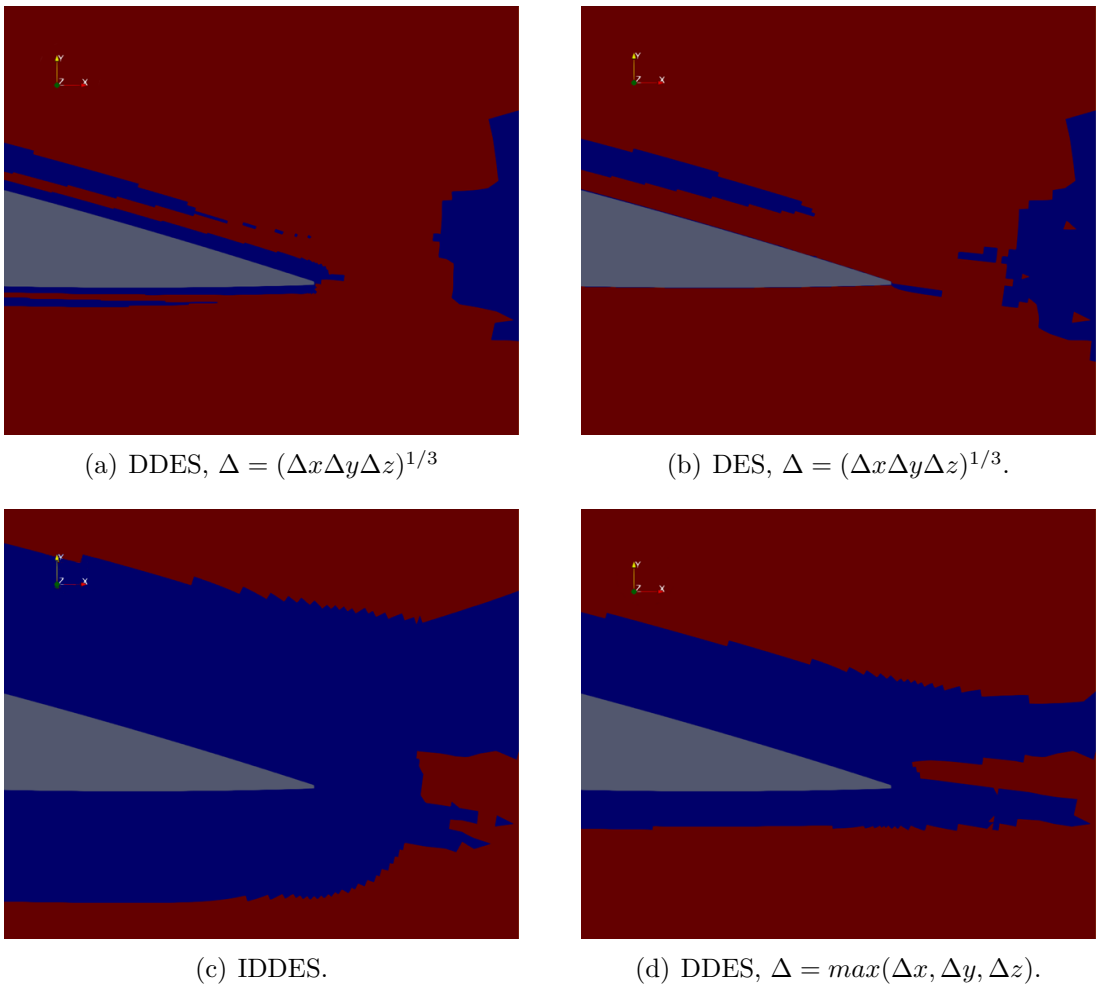

(a) DDES, $\Delta = (\Delta x \Delta y \Delta z)^{1/3}$

(b) DES, $\Delta = (\Delta x \Delta y \Delta z)^{1/3}$.

(c) IDDES.

(d) DDES, $\Delta = max(\Delta x, \Delta y, \Delta z)$.

Figure 3.6: Comparison of DES field between different DES models and DES delta calculating methods at trailing edge, low AoA.

The simulation results of force coefficients C_D and C_L can be found in table 3.5. Both unsteady RANS and DDES simulations provide similar results as the steady state in table 3.4. Therefore, for low AoA conditions, the unsteady character is not significant.

Table 3.5: Force coefficients, 2D low-AoA unsteady state simulation.

AoA	8.13°		12°	
	C_L	C_D	C_L	C_D
Experimental data	0.8788	0.0117	1.1485	0.0154
URANS simulation	0.8787	0.0157	1.2552	0.0211
URANS difference	-0.01%	34.19%	9.29%	37.01%
DDES simulation	0.8794	0.0157	1.2519	0.0219
DDES difference	0.068%	34.188%	9.003%	42.208%

3.2.3 Cause analysis for inaccuracy

The reason for the inaccuracy is considered to be the transition phenomenon, which is indicated by M. Sato et al. (2017) [41]. The process of a laminar flow becoming turbulent is known as laminar-turbulent transition. The main parameter characterizing transition is the Reynolds number. From Makoto Sato's research, for the 8.13° angle of attack case, there is an obvious transition region based on LES simulation. According to a rough simulation using the Langtry-Menter $k-\omega$ SST model, the transition can be seen in the same region. While for the cases using the $k-\omega$ SST model, this region will be regarded as turbulent.

This transition phenomenon is not considered in extreme condition simulations. Because for the 90° angle of attack cases, the Reynolds number is higher and the region of boundary layer is not so large. The boundary layer mainly distributes around the two tips of the foil. Therefore it not necessary to consider the transition for the high angle of attack conditions.

Besides, the mesh may not be fine enough to reach mesh independence which needs a series of mesh analysis to prove. However, since the results do not show significant deviation from the experimental data, and low angle of attack conditions are not the primary goal of this project, the mesh analysis for low angles of attack is not carried out in this thesis.

3.3 Critical angle of attack analysis

The above research in this chapter proves that 2D CFD simulations on a foil with low AoA can provide a relatively accurate prediction. In this section, a series of extra simulations are performed to study the effects of different AoA on the flow field and accuracy of CFD at high Reynolds numbers. The simulations in this section are listed in table 3.2. All the simulations carried out in this section are with $Re = 1e7$.

The pressure (p/ρ) distribution, together with the surface line integral convolution (LIC), from the simulation results are summarized in figure 3.7. It can be seen that when the AoA is less than 14°, the flow is attached to the foil. However, when the AoA is larger than 16°, flow separation becomes obvious, i.e. the stall phenomenon occurs. From this point of view, the critical angle of attack is about 16°, which is confirmed by wind tunnel experiments [32], since the maximum lift coefficient is obtained when the angle of attack is 16°. Flow separation begins near the trailing edge of the foil while the rest of the flow over the foil remains attached. For the case with the AoA as 18°, the flow separation is quite significant, which leads to the reduction in the lift coefficient generated by a foil as angle of attack increases.

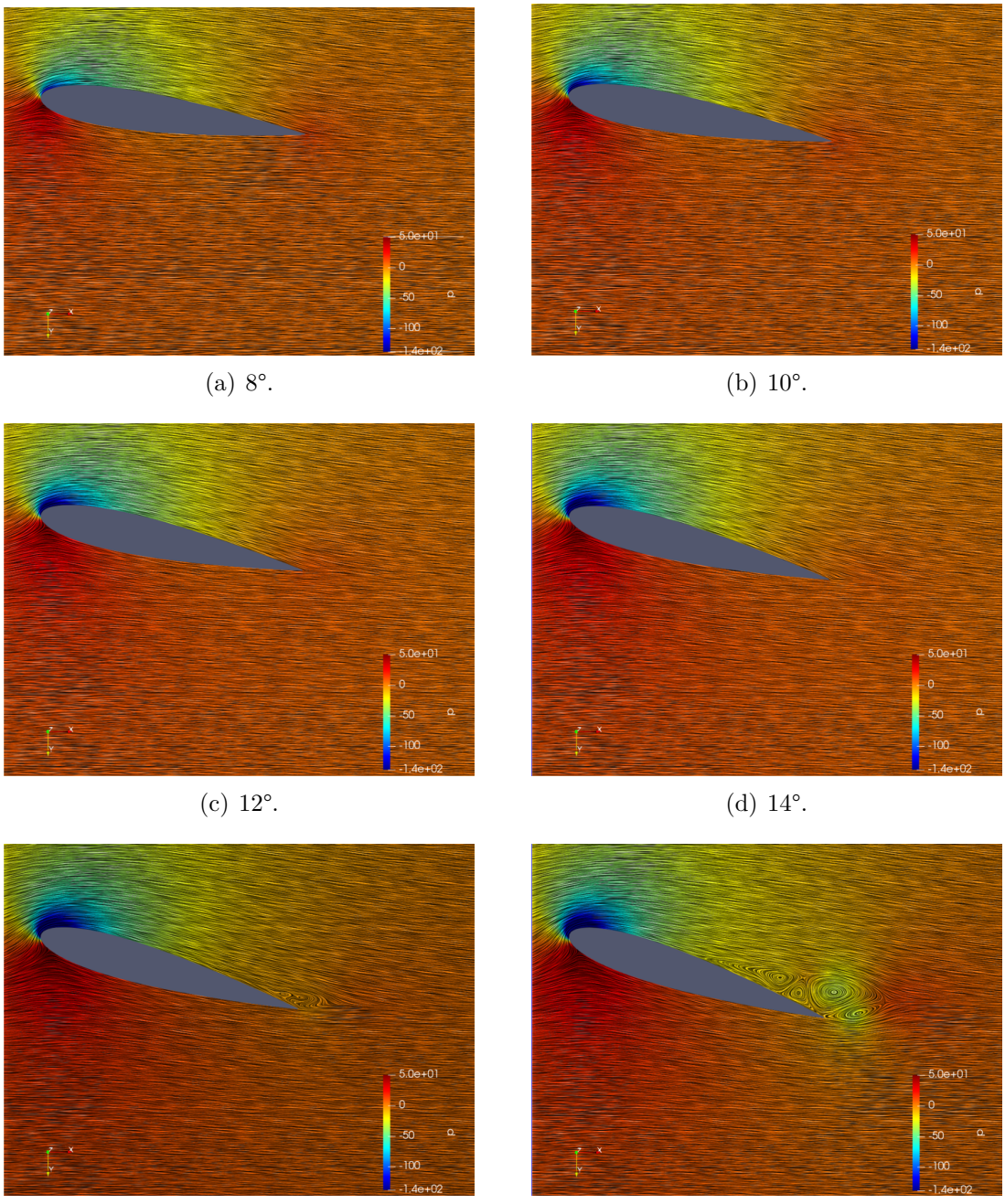

(a) 8°. (b) 10°.

(c) 12°. (d) 14°.

(e) 16°. (f) 18°.

Figure 3.7: Pressure (p/ρ) distribution and the surface line integral convolution (LIC), extra 2D low-AoA steady-state simulations.

Table 3.6 summarizes the force coefficients from the simulation results. Figure 3.8 is the bar chart that compares results from different simulations and the experimental data. When the AoA is in the range of 8° to 18°, the results from steady and unsteady state $k-\omega$ SST simulation are always similar. When the AoA is larger than 14°, RANS simulations will overestimate the lift force coefficients. The overestimation will be more significant when the AoA is 18°. On the other hand, DDES simulations

provide a more accurate prediction for situations with flow separation.

Table 3.6: Force coefficients, extra 2D low-AoA simulations.

	AoA / °	8	10	12	14	16	18
C_L	experiment	0.8800	1.1000	1.2591	1.3825	1.4233	1.3897
	steady RANS	0.8979	1.1050	1.2985	1.4713	1.6098	1.6826
	URANS	0.8826	1.0821	1.2667	1.4337	1.5758	1.6900
	DDES	0.8758	1.0703	1.2473	1.3957	1.4903	1.4820
C_D	experiment	0.0090	0.0103	0.0123	0.0147	0.0176	0.0213
	steady RANS	0.0109	0.0127	0.0127	0.0188	0.0246	0.0356
	URANS	0.0115	0.0134	0.0160	0.0197	0.0248	0.0325
	DDES	0.0124	0.0146	0.0178	0.0230	0.0323	0.0527

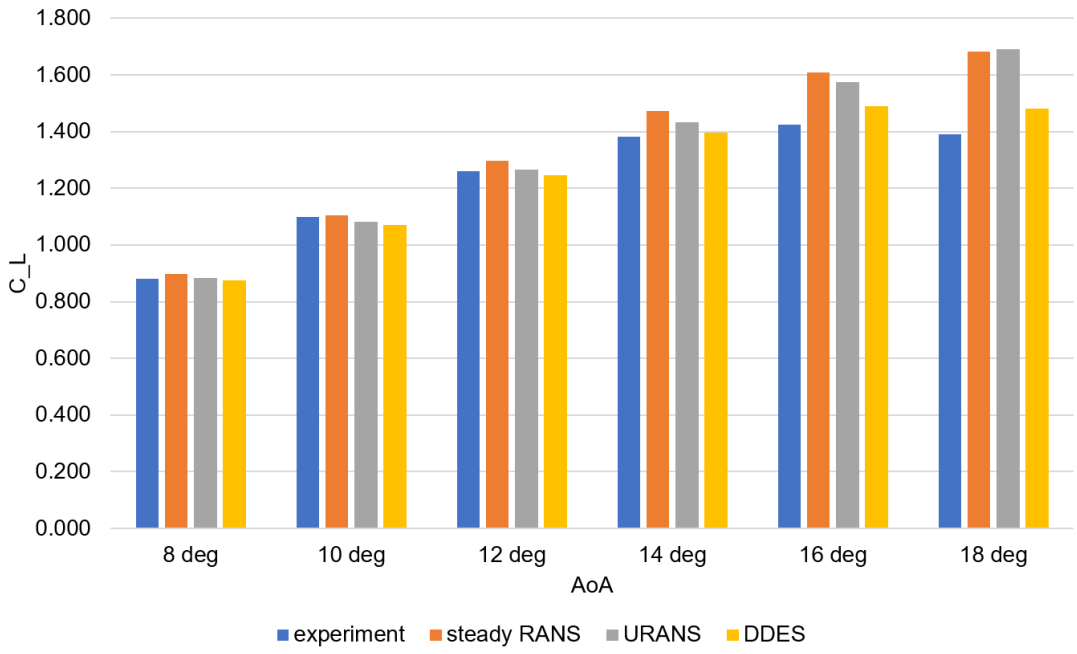

Figure 3.8: C_L, extra 2D low-AoA simulations.

Although flow separation is noticeable when the AoA is 18°, the unsteady flow character is still not obvious. Figure 3.9 is the results of DDES simulation with the AoA as 18°, which shows the distribution of velocity magnitude and its direction around the foil at different times. The difference in the flow field at different times is not obvious. In the sense of force coefficient, the unsteady character is also imperceptible. The variation of C_L with the AoA as 18° through time is plotted in figure 3.10. The value of the lift force coefficient becomes steady after 2 s with unapparent fluctuation.

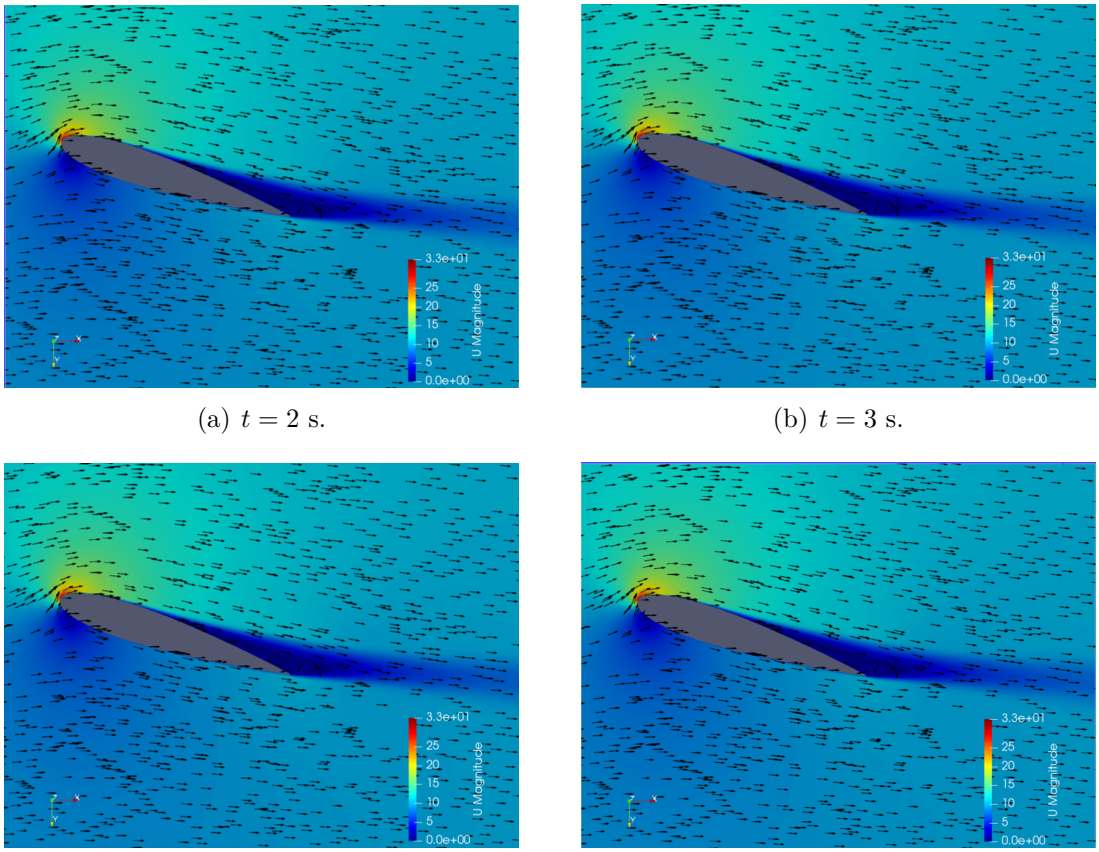

(a) $t = 2$ s. (b) $t = 3$ s.

(c) $t = 4$ s. (d) $t = 5$ s.

Figure 3.9: Velocity distribution, 2D 18° AoA DDES simulations.

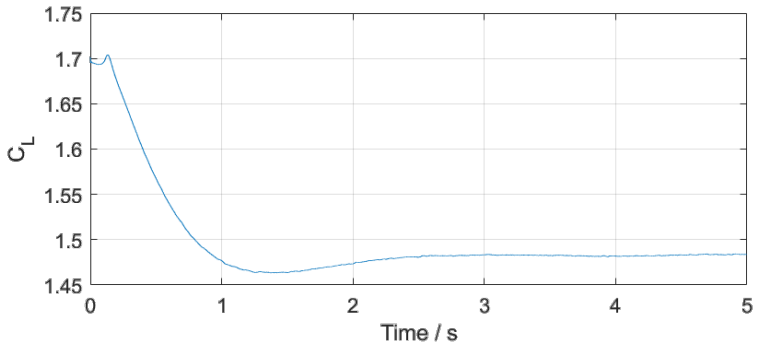

Figure 3.10: C_L, 2D 18° AoA DDES simulations.

4

Extreme condition simulations

The main aim of this project is to analyze the loading condition of foils under the extreme condition, i.e. the 90° AoA condition. In this chapter, the methodologies and results of simulations for AoA = 90° will be presented.

The aim of these simulation cases is to provide results in good agreement with the experimental data so that the simulation methodologies can be proved to be credible. However, some unexpected errors happen during the simulation. The accuracy of the results is hard to reach. It can be believed that there are many uncertainties, which are not considered in the initial plan of this project, for simulations under the deep stall condition. Therefore, this chapter will present the process of the research work and discuss the reasons for inaccuracy.

For simulation cases in this chapter, the Reynolds number is set to be 1×10^7.

4.1 2D simulation

To begin with, 2D simulations are carried out to provide approximate information. In the current method, the horizontal 2D wing profile is simulated by CFD. The aerodynamic pressure distribution along the foil is calculated to estimate the total foil force [10]. Although the 3D flow phenomenon is obvious for the deep stall foil and the calculation results may not be accurate enough, the 2D simulation can still roughly reflect the trend of the flow field and provide guidance for the follow-up work.

4.1.1 RANS simulation

Steady and unsteady RANS simulations, i.e. RANS simpleFoam and pimpleFoam in OpenFOAM, are executed.

Because of the flow separation, which can not be predicted very well by the RANS model, RANS simulation may not give very accurate results. Even so, it's still important to perform RANS simulations to give an initial condition for IDDES simulation and also be applied for the mesh analysis.

The mesh for the 2D cases is shown in figure 4.1. The region close to the foil is

structured, while other regions are unstructured. One of the differences from low AoA cases is that the downstream region is refined to simulate the expected vortex shedding. The length of the refined region is 10 times the chord length (10m). The total number of cells is 98,759.

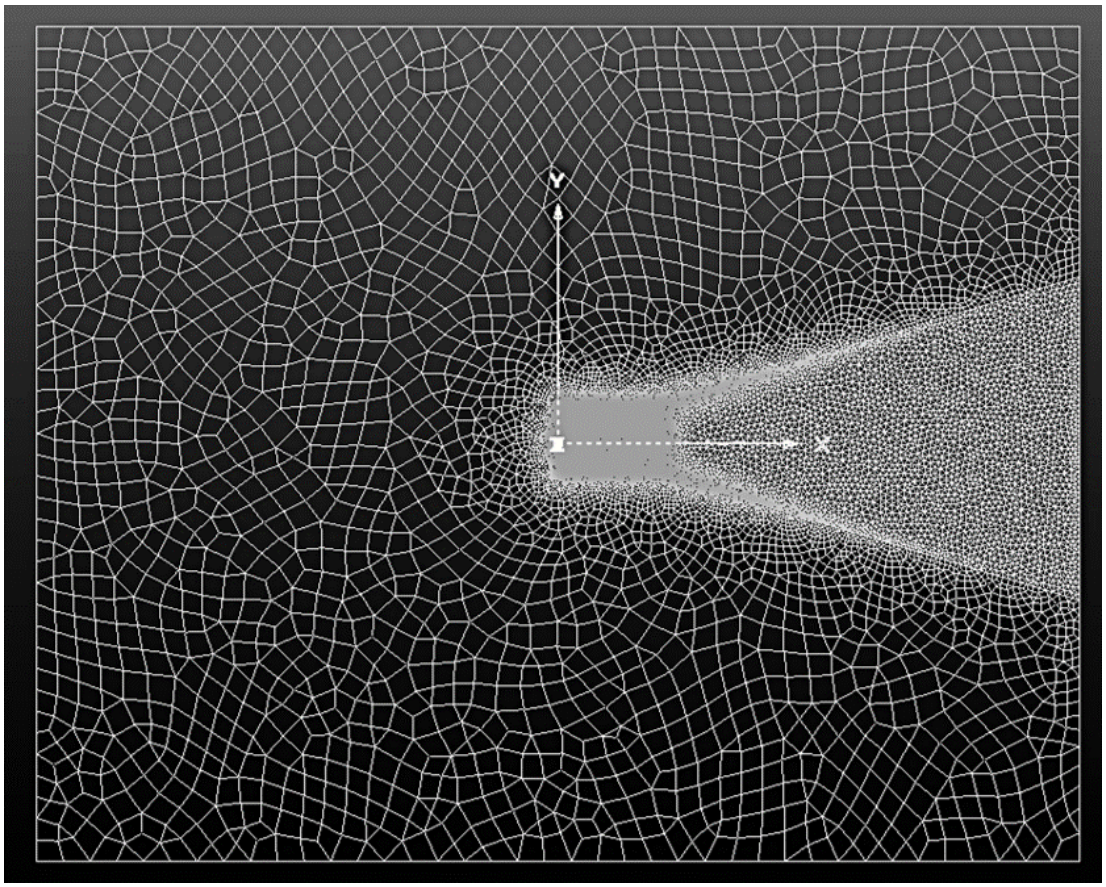

Figure 4.1: Mesh, 90° 2D cases.

The mean value of force coefficients C_D and C_L from RANS simulations are summarized in table 4.1. The detailed time-varying curves of the force coefficient can found in section 4.3. In the sense of the force coefficients, the simulation results from steady and unsteady states are similar. However, the results are quite different from the experimental data.

Table 4.1: Force coefficients, 2D RANS simulation with 90° AoA.

Coefficients	Experimental data	SimpleFoam result	SimpleFoam difference	PimpleFoam result	PimpleFoam difference
C_D	1.8	1.3483	-25.09%	1.374	-23.67%
C_L	0.09	0.1071	19.00%	0.11	22.22%

Figure 4.2 shows the distribution of velocity magnitude of 12° AoA case and 90° AoA case with the same Reynolds number (1e7) from steady state RANS simulation.

For the low angle of attack condition, the flow becomes uniform quickly in the downstream field. However, under the 90° AoA condition, the foil has a great influence on the downstream flow. There is an area in front of the foil, where the velocity is almost zero. In the downstream region, the velocity magnitude is also very low, so it seems that there is a large area of added mass at the suction side of the foil. That's because of the vorticity which will be discussed in subsection 4.1.2.

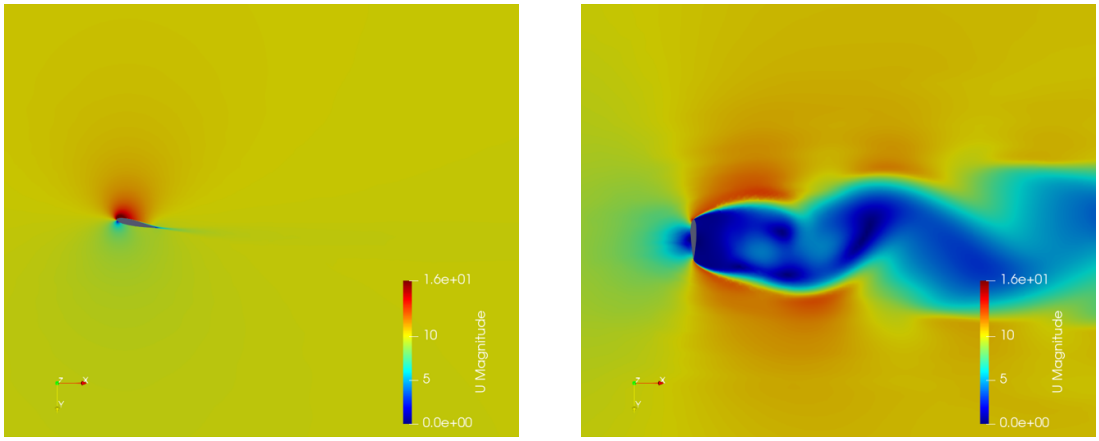

(a) 12°. (b) 90°.

Figure 4.2: Velocity distribution, 2D steady state RANS simulation with 90° AoA.

The velocity vectors and pressure (p/ρ) distribution of steady state RANS and URANS results are shown in figure 4.3. Compared with the results from low AoA simulation cases in chapter 3, an obvious low-pressure region can be found in the downstream region of the foil, which results in the high C_D.

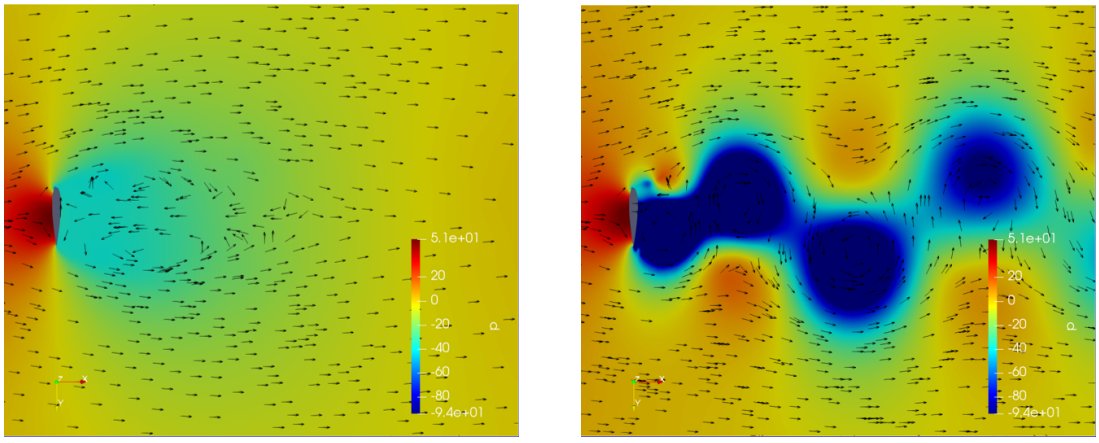

(a) Steady state. (b) Unsteady state.

Figure 4.3: Velocity vectors and pressure (p/ρ) distribution, 2D RANS simulation.

From the steady state results, only two big vortices can be found behind the foil. A similar phenomenon was also pointed out by M. R. Castelli et al. (2012) in a

simulation for a flat plate with 90° AoA [31]. However, from the unsteady state results, more instantaneous characters of the flow filed are provided. It can be seen that repeating pattern of swirling vortices develop one after another in the downstream region.

4.1.2 DES simulation

For DES simulations, several different models are compared. Figure 4.4 shows the initial DES field from different DES models. For the DES model, the same problem that the RANS region in boundary layers is not thick enough to cover all the boundary region encountered as low-AoA simulations. For the DDES model, the LES region is too small at the beginning, so that some vorticities and the flow separation are not included in the LES region. Although the IDDES model may allocate too much domain into the LES region, which may ask higher requirements for the numerical meshes, all the boundary layer is in the RANS region and most of the downstream field is in the LES region. Therefore, the IDDES model is selected for the 90° AoA simulations.

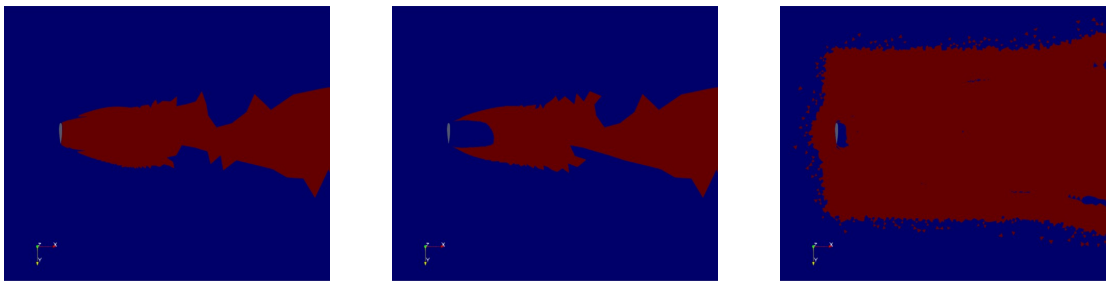

(a) DES model. (b) DDES model. (c) IDDES model.

Figure 4.4: Comparison between DES model under large AoA condition.

During the time steps of the IDDES simulation, the DES field keeps continuously changing. Figure 4.5 shows its development over time steps. It can be seen that at the beginning, the distribution of the DES field has a strong relationship with the mesh. The boundary of the RANS region and the DES region is almost the boundary of the refined downstream part and the outer mesh, as figure 4.1 shows. However, it changes after several time steps and shows less dependence on the mesh.

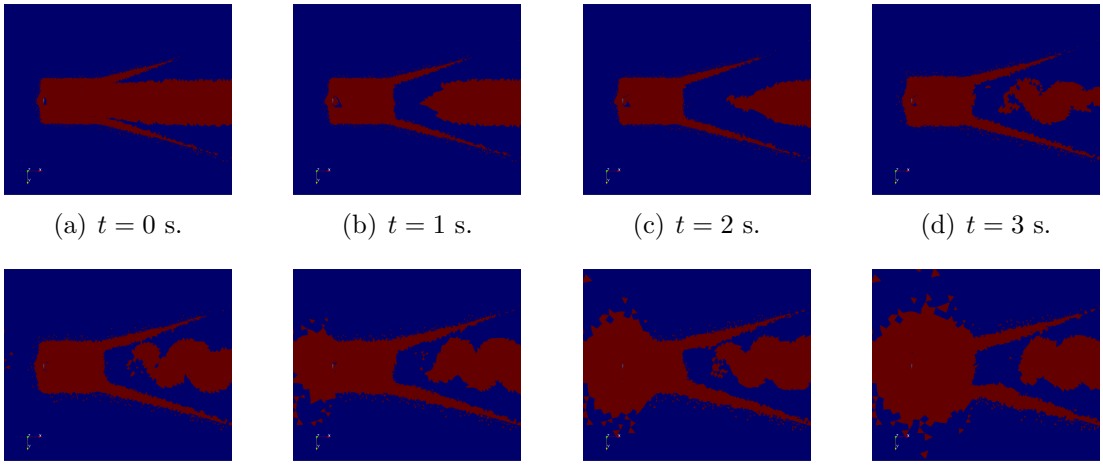

(a) $t = 0$ s. (b) $t = 1$ s. (c) $t = 2$ s. (d) $t = 3$ s.

(e) $t = 4$ s. (f) $t = 4.5$ s. (g) $t = 5$ s. (h) $t = 5.5$ s.

Figure 4.5: Development of DES field through time, 2D IDDES simulation with 90° AoA.

From the results, obvious von Kármán vortex street can be seen in the downstream region. Figure 4.6 shows the pressure (p/ρ) distribution at different time steps. Vortices are created at the back of the foil and detach periodically from either edge of the foil forming a von Kármán vortex street. The vortex street can not be predicted when performing steady state simulations, which is the reason for the low-velocity areas in figure 4.2.

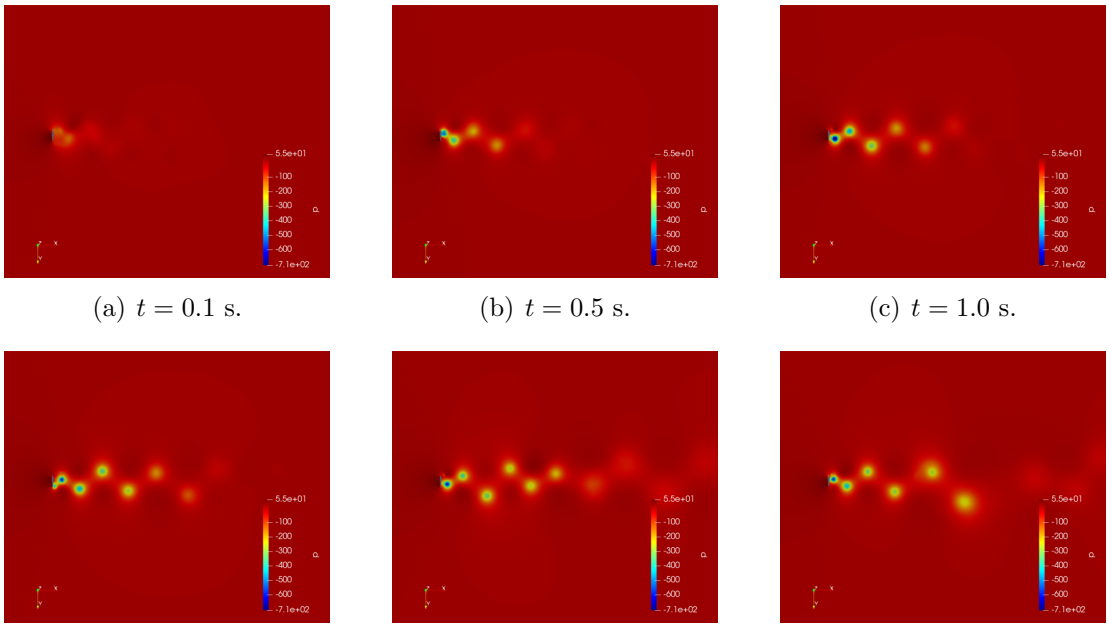

(a) $t = 0.1$ s. (b) $t = 0.5$ s. (c) $t = 1.0$ s.

(d) $t = 1.5$ s. (e) $t = 3.5$ s. (f) $t = 5.5$ s.

Figure 4.6: Pressure (p/ρ) distribution through time, 2D IDDES simulation with 90° AoA.

The variation of the force coefficients C_D and C_L through time steps is summarized in figure 4.7. Due to the vortex shedding, the force coefficients have notable oscillation. One interesting thing is that not only the main vortices are developing, but also small vortices at the two tips are created and dissipate quickly, as figure 4.17 in section 4.2 shows, which leads to the fluctuation of the force coefficients.

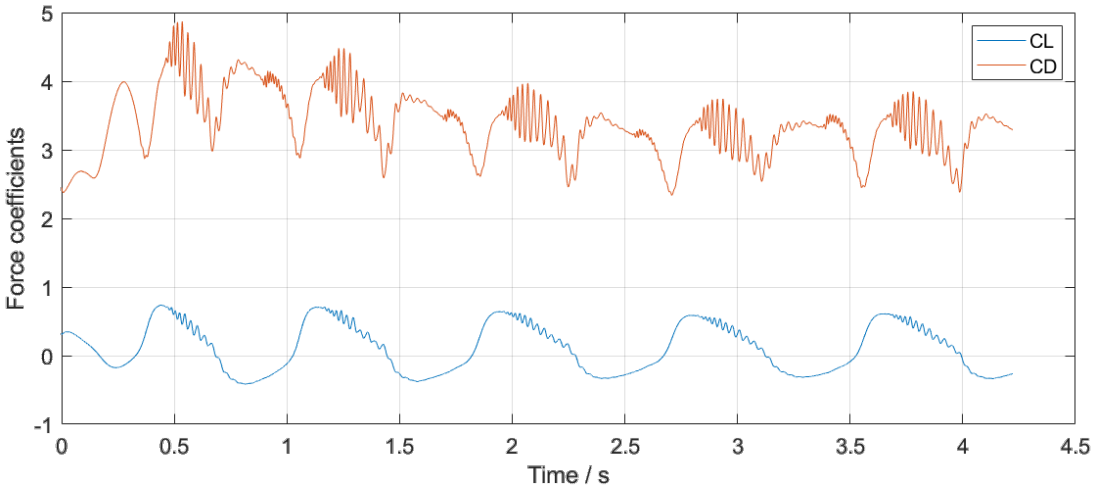

Figure 4.7: Force coefficients C_D and C_L through time, 2D IDDES simulation with 90° AoA.

The main value of the force coefficients are that $C_D = 3.378$ and $C_L = 0.106$. However, the experimental data is that $C_D = 1.800$ and $C_L = 0.090$. Thus, C_D and C_L are separately overestimated by 87.7% and 17.8%.

One probable reason to explain the disagreement is that for 90° condition, the flow has a notable 3D character. So when performing a 2D simulation, the flow in the z-direction, i.e. the longitudinal direction, can not be simulated.

4.2 Preliminary 3D simulation

After finding that the IDDES results from the 2D simulation are not consistent with the experimental data, the reason is first thought to be that some 3D flow characters are not detected by 2D simulation. Therefore, the 3D IDDES simulation for a uniform 3D foil is performed.

4.2.1 Mesh and boundary conditions

The 3D IDDES simulation is firstly performed on two meshes, a coarse one with 1,241,700 cells and a fine one with 5,925,540 cells. The fine mesh is based on the mesh used in the 2D simulation, as figure 4.8 shows. In the z direction, the span wise length is 0.3 times the chord length and 60 layers are generated.

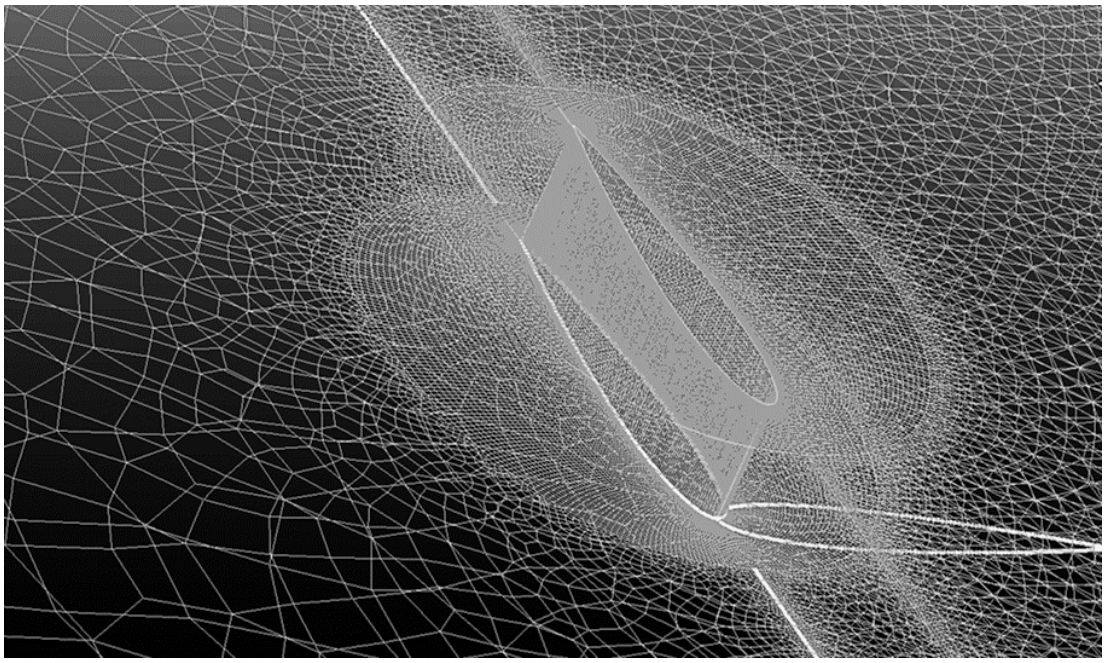

Figure 4.8: The fine mesh with 5,925,540 cells used in preliminary 3D simulation.

Table 4.2 shows the setting of the boundary condition. Different from the 2D simulation in section 4.1, the front and back panels are set to be cyclicAMI, so that the foil can be considered to have an infinite length. k at wall is set to be a fixed value as 0 because of the low y^+.

Table 4.2: 3D boundary condition settings.

	Foil	Front and Back	Top and Bottom	Inlet	Outlet
P	zeroGradient	cyclicAMI	zeroGradient	zeroGradient	fixedValue uniform 0
U	fixedValue uniform (0 0 0)	cyclicAMI	slip	fixedValue uniform (10 0 0)	zeroGradient
k	fixedValue uniform 0	cyclicAMI	slip	fixedValue uniform 0.047633	inletOutlet uniform 0.047633
omega	omegaWallFunction	cyclicAMI	slip	fixedValue uniform 264.63	inletOutlet uniform 264.63
nut	nutkWallFunction	cyclicAMI	slip	calculated	calculated

4.2.2 DES field

The results of the two cases are shown in the following figures and tables. The DES fields of the calculation domain are shown in figure 4.9. The flow in the red region is calculated by the LES model, while it is calculated by the RANS model in the blue region. The turbulence model is IDDES. In the URANS region, the $k-\omega$ SST model is applied. The LES length-scale delta is calculated by IDDESDelta. It can be found that all the boundary layer is in the RANS region and most of the vortices

happen in the LES region. The distribution of the DES field from the 3D simulation is similar to that from 2D simulation.

In the downstream region far away (more than 10 times of the chord length) from the foil, although there are still vortices in these areas, the flow is calculated by the RANS model, as figure 4.9 shows. The vortices have been dissipated, and since they are far away from the foil, the influence on the loading condition of the foil is not significant.

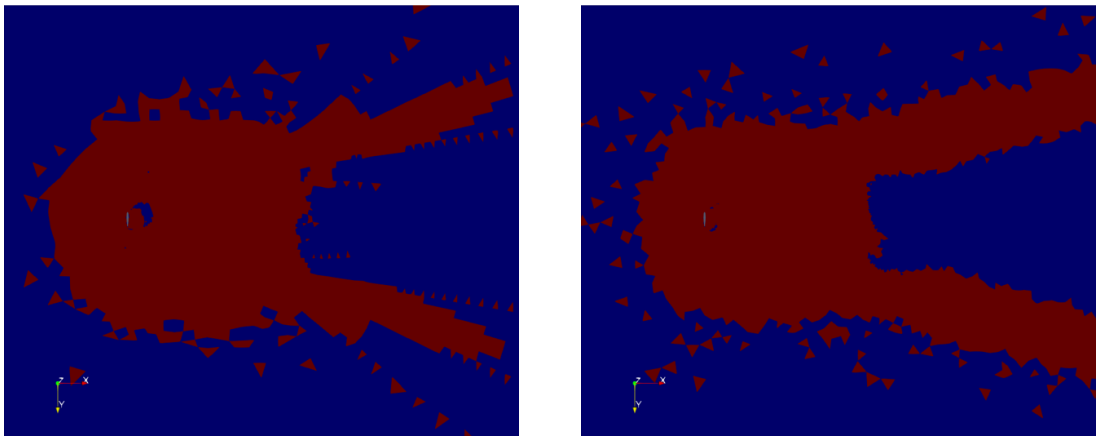

(a) Coarse mesh, $t = 2.5$ s.

(b) Fine mesh, $t = 2.5$ s.

Figure 4.9: Development of the DES fields, preliminary 3D IDDES simulation.

4.2.3 Force coefficients

Figure 4.10 shows C_D and C_L variations with time. Similar to results from the 2D IDDES simulation in section 4.1, periodic oscillations and small fluctuations can still be found. The total simulation time is not enough to get a precise mean value of the coefficients, but it's obvious that both C_D and C_L are overestimated. Although the simulation sequence is too short to define the shedding frequency, it appears that there is difference between meshes. It can also be found that simulation based on the fine mesh predicts more fluctuation. It's because that more details of the flow field can be predicted by using more precise meshes. Table 4.3 summarizes the roughly mean value of C_D and C_L. A

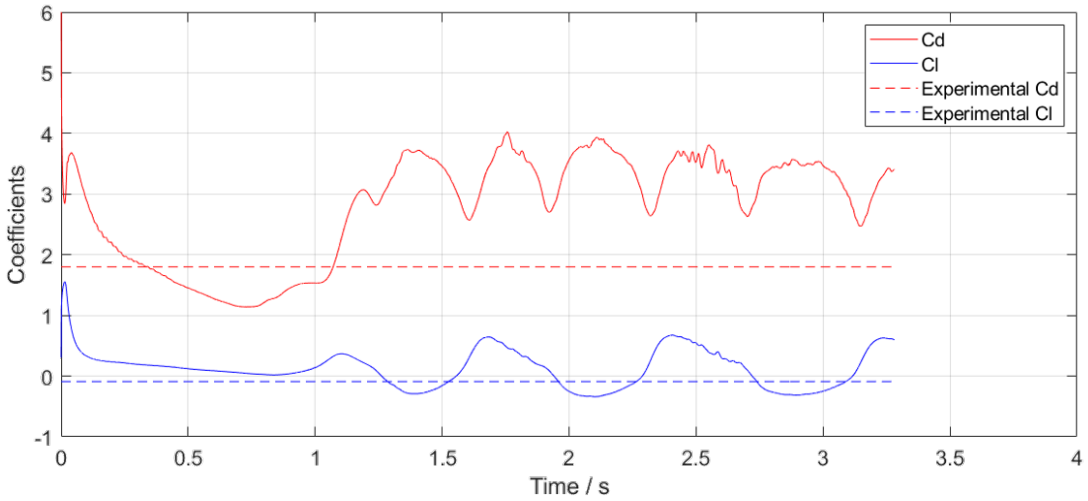

(a) Results of the coarse mesh.

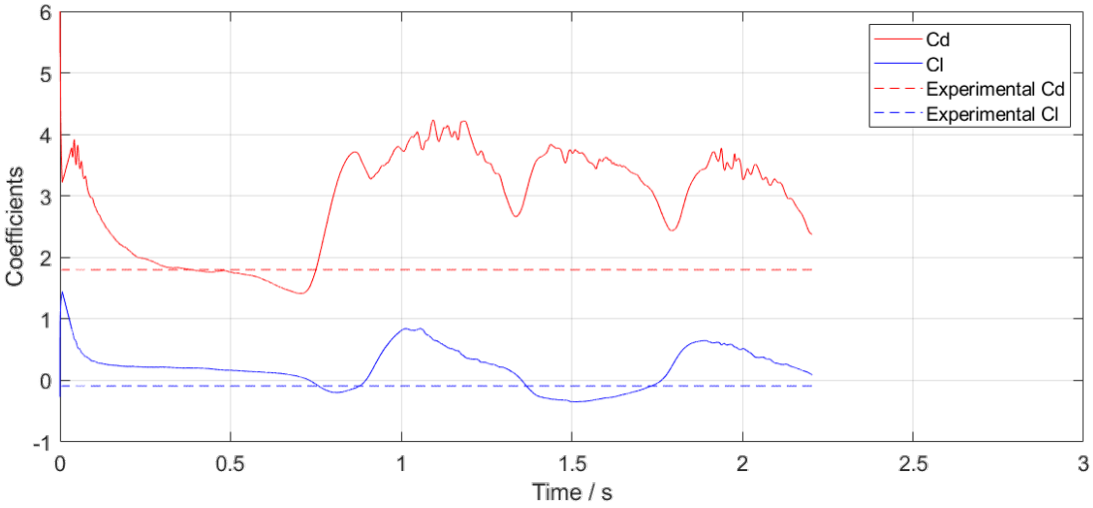

(b) Results of the fine mesh.

Figure 4.10: Force coefficients, preliminary 3D IDDES simulation.

Table 4.3: Mean value of C_D and C_L, preliminary 3D IDDES simulation.

	Coarse mesh	Fine mesh	Experimental
C_D	3.114	3.392	1.800
C_L	0.103	0.167	0.090

4.2.4 Flow field

Figure 4.11 and 4.12 show the pressure (p/ρ) distribution throughout the domain at different time. In the figures, quantities of low-pressure areas that reflect the vortices can be seen in the downstream region. The results show the vortex street, which is similar to that of 2D simulation in section 4.1. Vortices at the leading

edge and the trailing edge develop one after another. These vortices will sustain for several seconds and gradually dissipate.

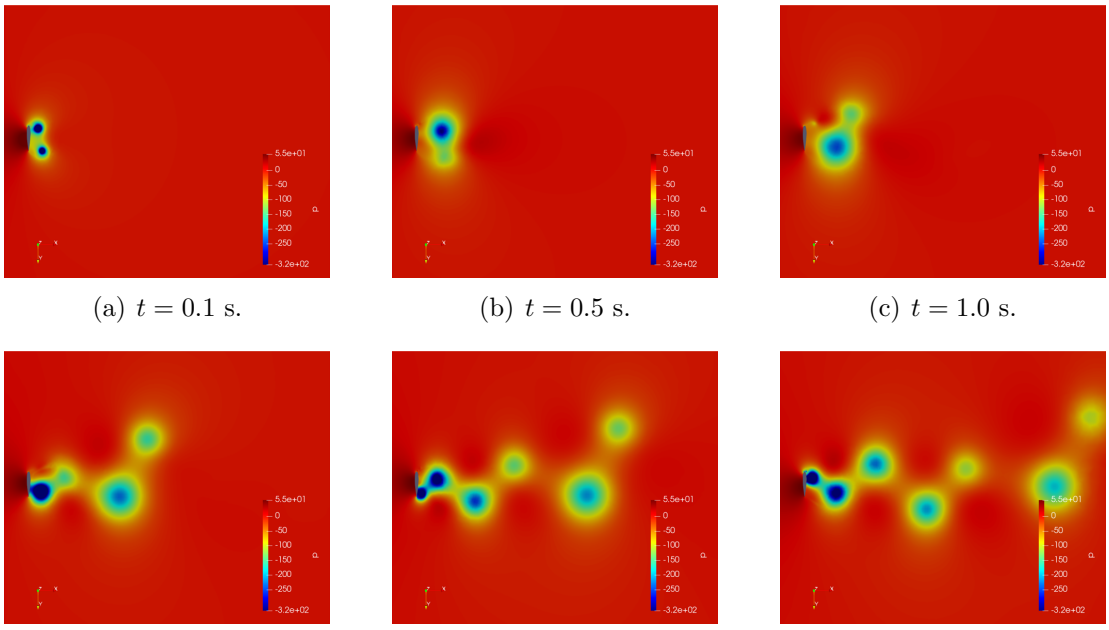

(a) $t = 0.1$ s. (b) $t = 0.5$ s. (c) $t = 1.0$ s.

(d) $t = 1.5$ s. (e) $t = 2$ s. (f) $t = 2.5$ s.

Figure 4.11: Pressure (p/ρ) distribution through time, preliminary 3D IDDES simulation with the coarse mesh.

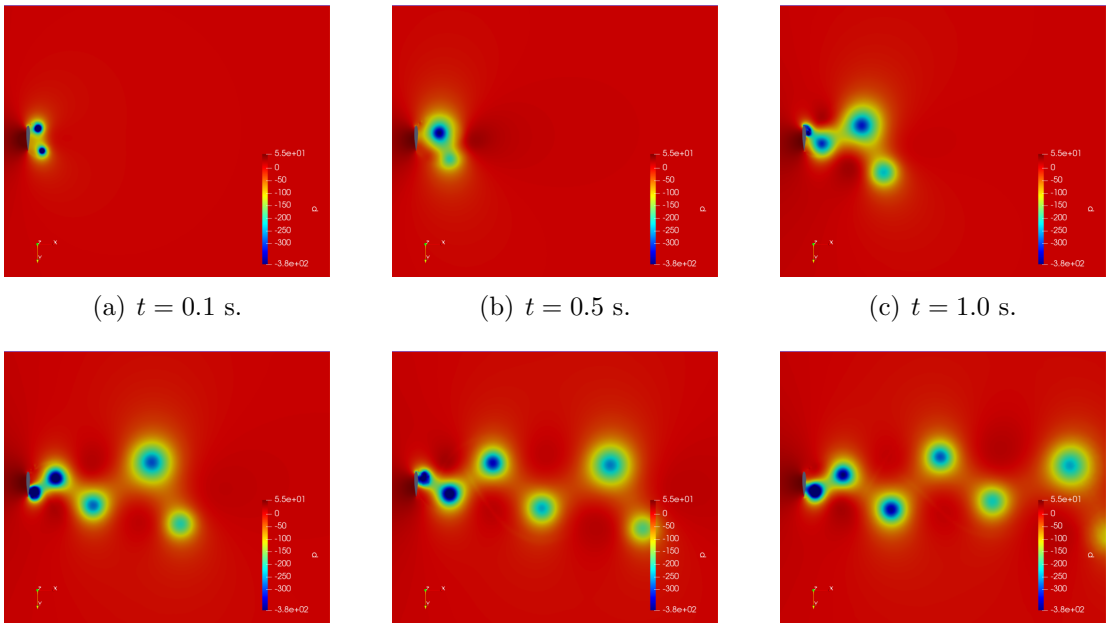

(a) $t = 0.1$ s. (b) $t = 0.5$ s. (c) $t = 1.0$ s.

(d) $t = 1.5$ s. (e) $t = 2$ s. (f) $t = 2.5$ s.

Figure 4.12: Pressure (p/ρ) distribution through time, preliminary 3D IDDES simulation with the fine mesh.

In steady state simulations, the velocity magnitude of the flow in the downstream region is always very low, as figure 4.2 shows. However, the IDDES simulations give different results. The velocity magnitude of the flow in the downstream region is time-variant because of the vortex street. Although the results do not agree with the experimental data very well, obvious z-direction flow is predicted. Figure 4.13 shows the distribution of velocity in z-direction. The maximum value of the velocity in the z direction is in the same order of magnitude as velocity in x and y direction. Significant U_z occurs in the downstream region close to the foil.

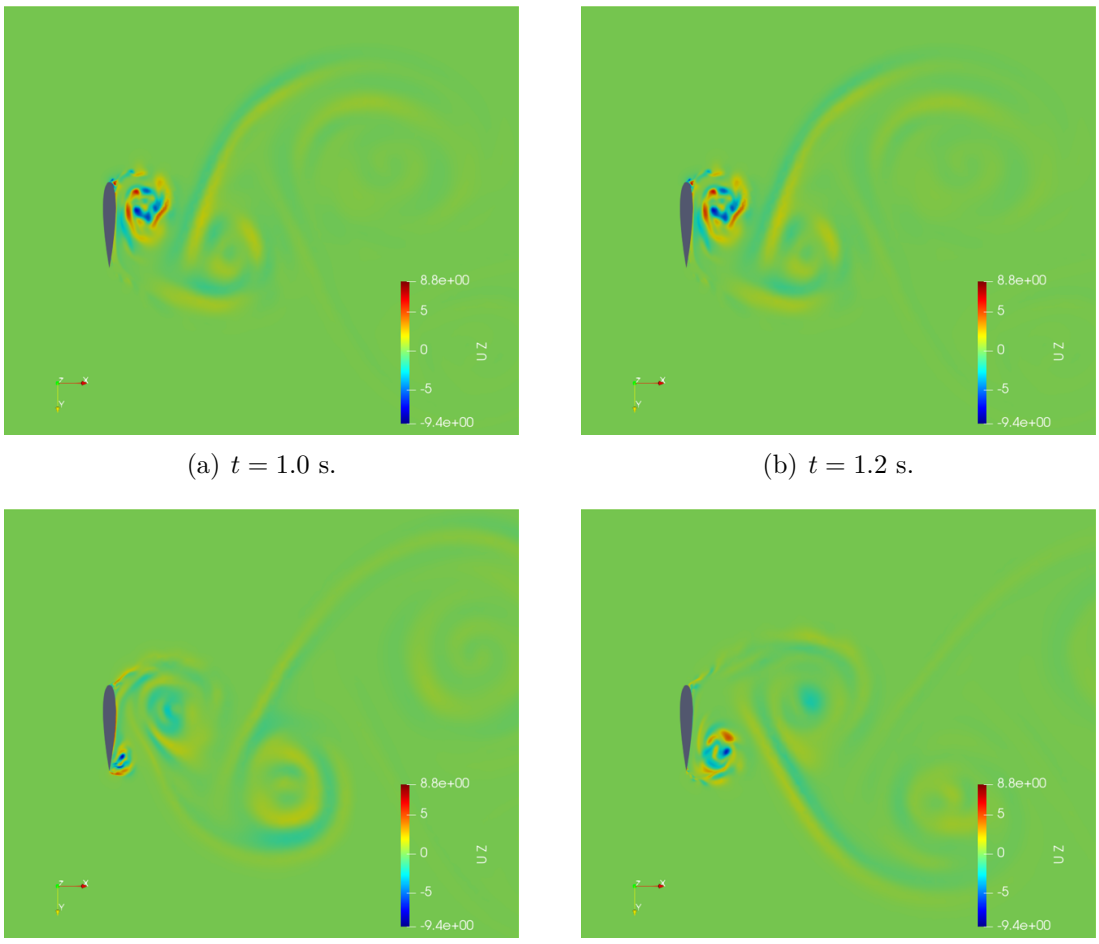

(a) $t = 1.0$ s. (b) $t = 1.2$ s.

(c) $t = 1.4$ s. (d) $t = 1.6$ s.

Figure 4.13: Distribution of velocity in z-direction, preliminary 3D IDDES simulation with the fine mesh.

Figure 4.14 and figure 4.15 show the distribution of vorticity and Q which indicates the vorticities of the flow. The results based on the fine mesh provide a more complex vortex structure. In the results of fine mesh, not only the vortices, but also the "belts" accompanying to them can be seen. This phenomenon can not be detected from the results of the coarse mesh.

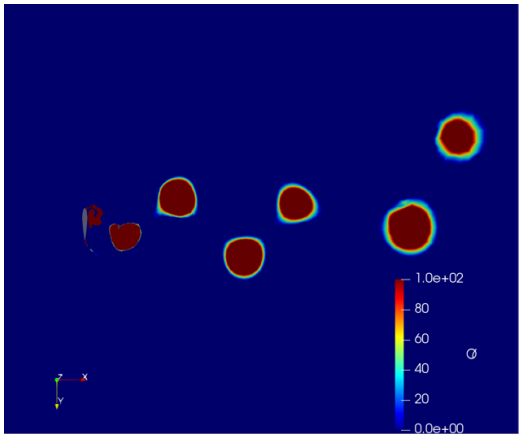

(a) Coarse mesh, $t = 2.5$ s.

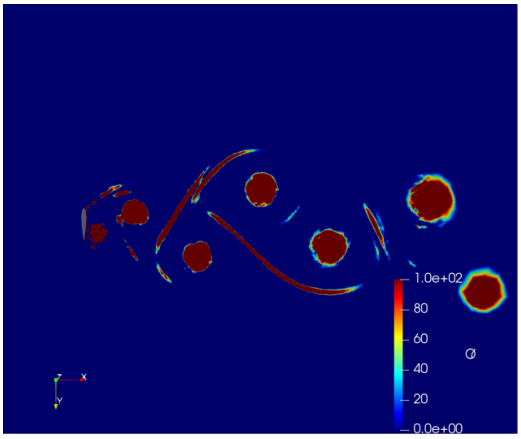

(b) Fine mesh, $t = 2.5$ s.

Figure 4.14: Distribution of Q, preliminary 3D IDDES simulation.

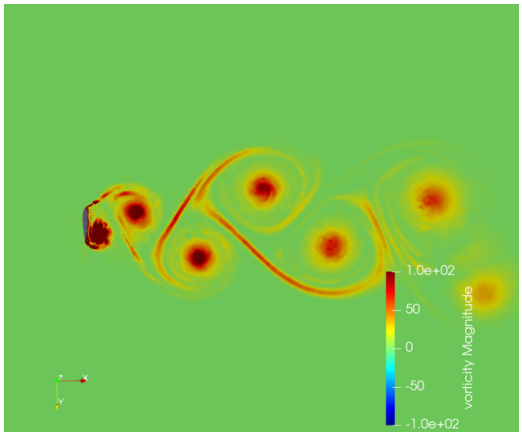

(a) Magnitude.

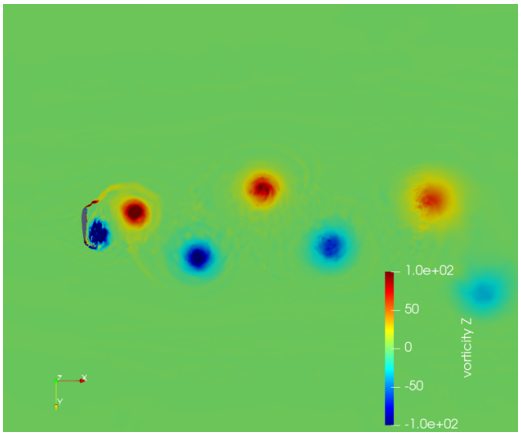

(b) z direction.

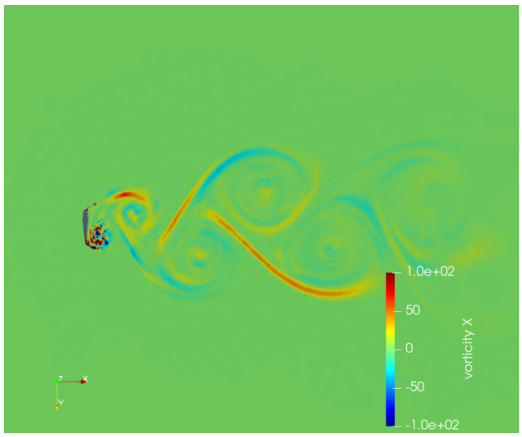

(c) x direction.

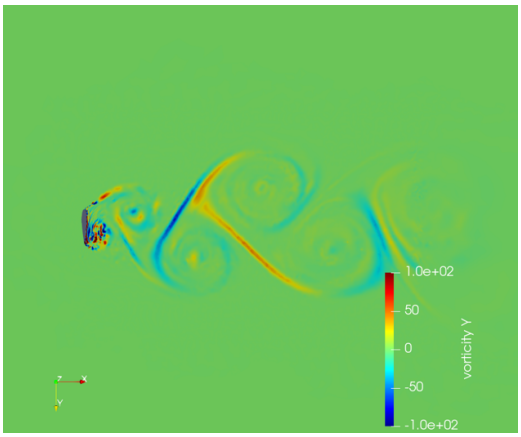

(d) x direction.

Figure 4.15: Distribution of vorticity in each direction, preliminary 3D IDDES simulation with the fine mesh at $t = 2.2$ s.

Figure 4.16 presents the distribution of velocity in the z-direction throughout the contour of $Q = 10$. It can be easily found that there is an obvious 3D flow structure at the downstream field close to the foil. This is also the region where the maximum value of velocity in the z-direction happens. However, in the downstream region far away from the foil, the longitudinal flow is unapparent.

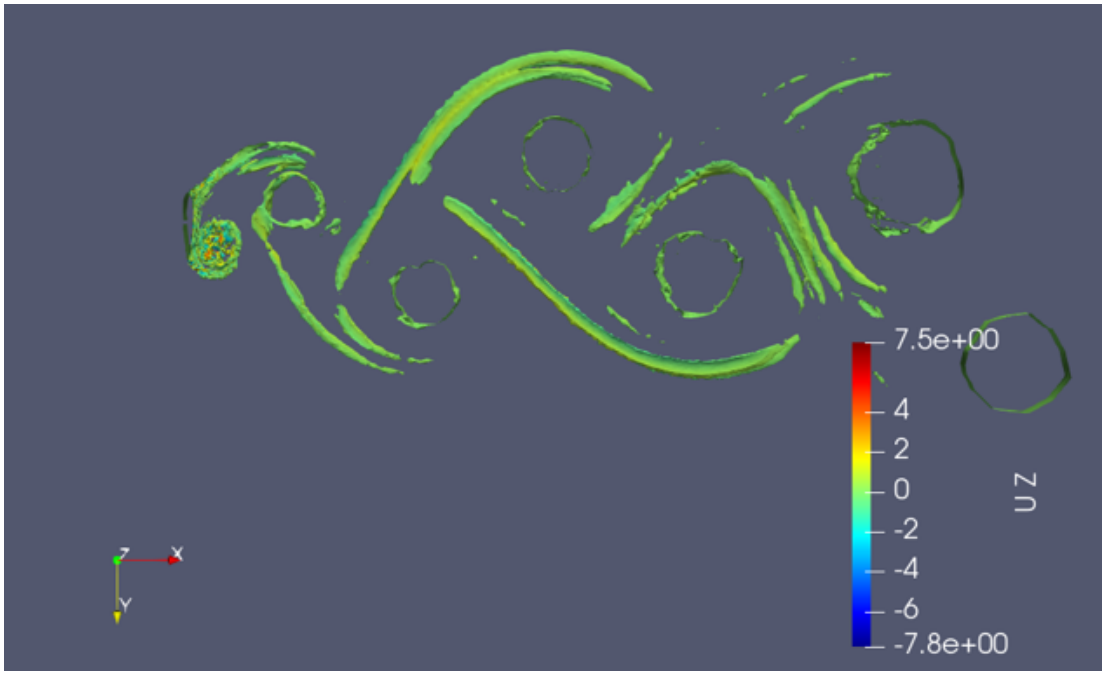

(a) Overview.

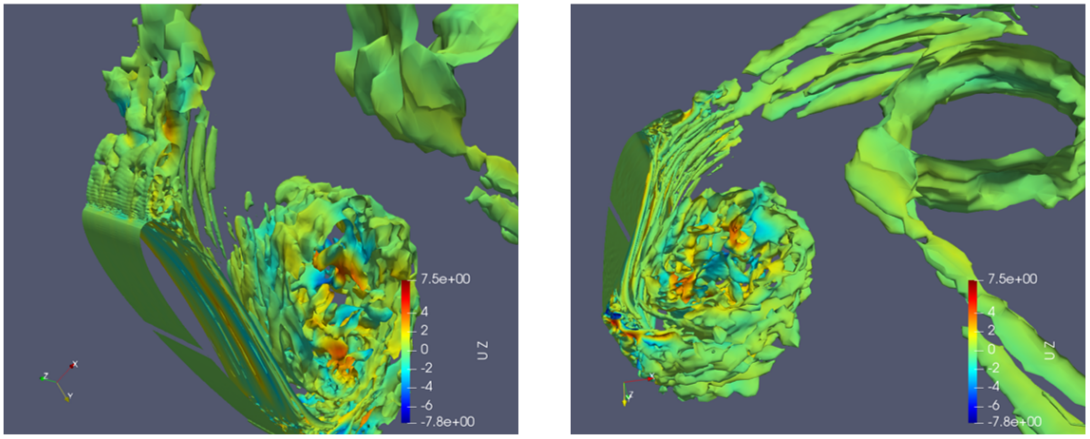

(b) Zoom close to the foil.

Figure 4.16: Distribution of U_z throughout the contour of $Q = 10$, preliminary 3D IDDES simulation with the fine mesh at $t = 2.2$ s.

In 2D simulations, small vortices, which are considered to be the primary reason for the fluctuation of C_D and C_L, were found at the leading edge as figure 4.17 shows. This phenomenon is also detected in the 3D simulation of the fine mesh as figure 4.18 shows. These vortices do not develop together with the mean vortices (the large

vortices which compose the vortex street). Instead, they dissipate quickly.

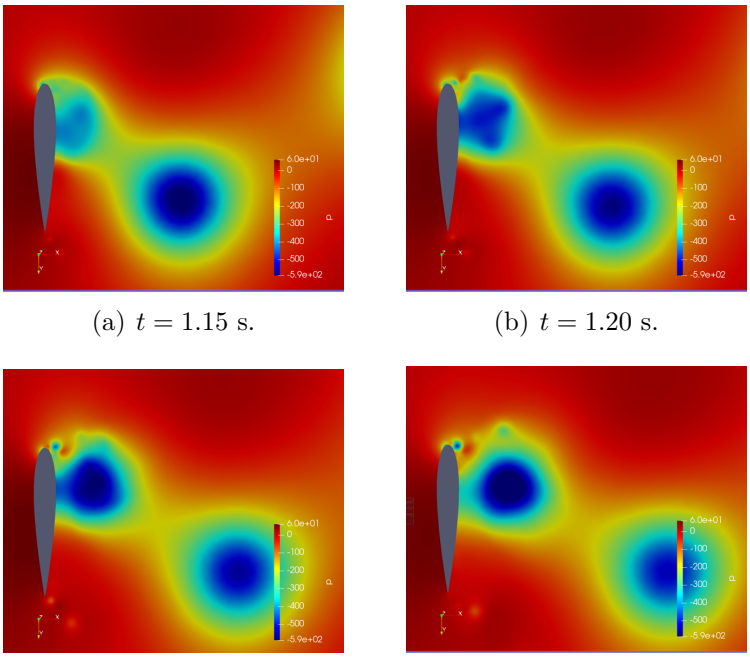

(a) $t = 1.15$ s. (b) $t = 1.20$ s.

(c) $t = 1.25$ s. (d) $t = 1.30$ s.

Figure 4.17: Small vorticities at the leading edge, 2D IDDES simulation with 90° AoA.

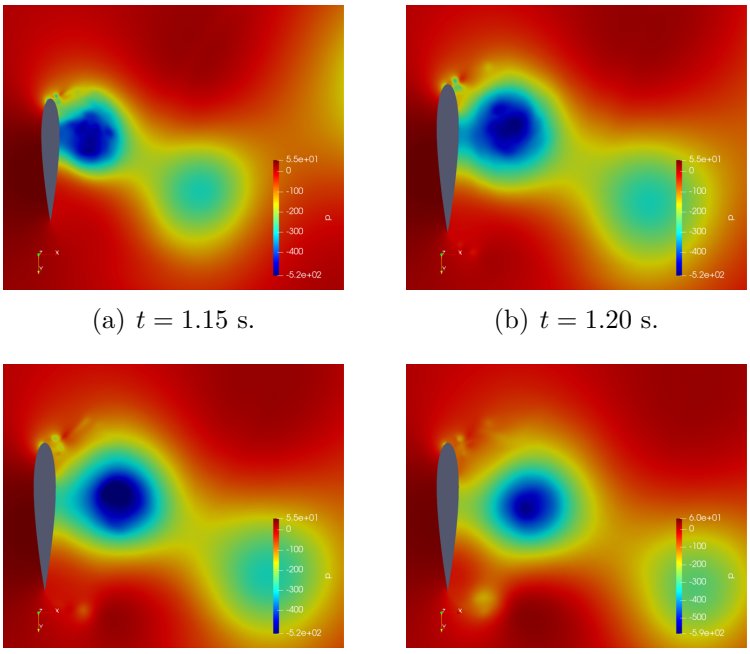

(a) $t = 1.15$ s. (b) $t = 1.20$ s.

(c) $t = 1.25$ s. (d) $t = 1.30$ s.

Figure 4.18: Small vorticities at the leading edge, preliminary 3D IDDES simulation with 90° AoA.

4.3 Mesh analysis and scheme study

From the preliminary 3D simulation, the force coefficients C_D and C_L are overestimated and do not agree with the experimental data well.

One problem of the coarse mesh is that the y^+ value along the foil is too high (larger than 5), which will give bad prediction in the boundary layer. But for the fine mesh, the y^+ is usually less than 1. Although sometimes the value of y^+ will be higher than 1 in some local regions, as figure 4.20 shows, it will improbable lead to such huge overestimation. Some other reasons for the inaccuracy are discussed in this section.

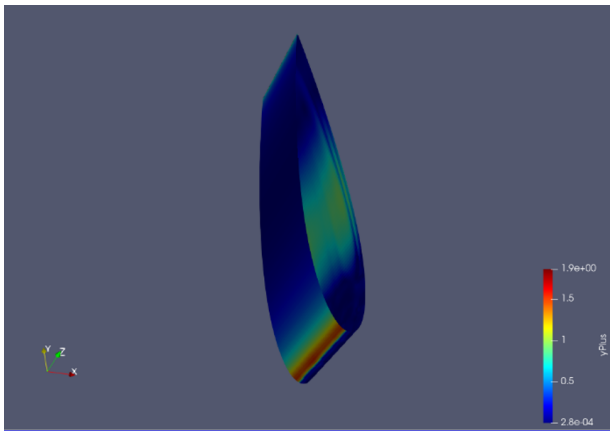

Figure 4.19: Distribution of y^+, preliminary 3D IDDES simulation with the fine mesh at $t = 2.2$ s.

To find the reason for the overestimation, mesh analysis and scheme study are implemented to see if the fineness of the mesh reaches the mesh independence and if the scheme applied is accurate enough.

4.3.1 Steady state analysis

7 structured meshes and 6 unstructured meshes are used for the mesh analysis. The 3D simulation cases in section 4.2 were using unstructured mesh for the downstream region. Thus, mesh analysis for the unstructured mesh is firstly carried out. RANS simpleFoam simulation is executed for each mesh.

Figure 4.20 shows an example of the unstructured mesh. The boundary layer and the region attached to it is structured, while the other parts of the domain, including the downstream region, are unstructured.

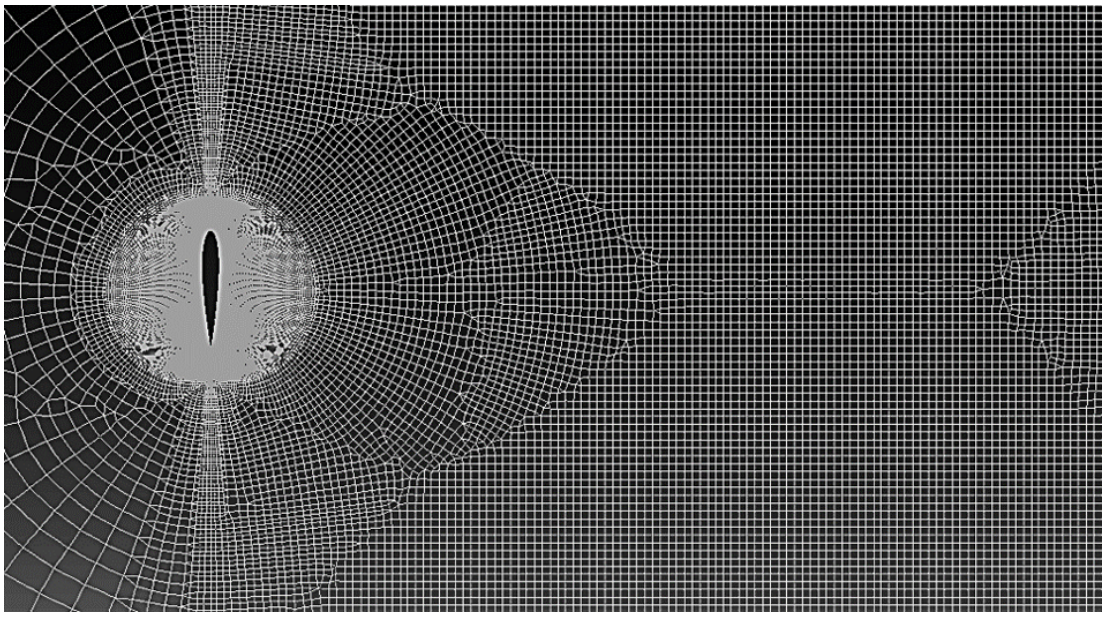

Figure 4.20: Example of an unstructured mesh, mesh 1-4.

The simulations are carried out by using the $k-\omega$ SST model and the SIMPLE algorithm. The initial 2000 steps are using a quite diffusive scheme, the linear upwind grad(U) scheme for $\nabla \cdot (\rho UU)$. After 2000 steps, the limited linear scheme, which is more accurate, is used for it. Table 4.4 summarized the force coefficients as the results of different meshes. The mean values are calculated from the steps using the limited linear scheme. It can be seen that the drag force coefficients, C_D, are always underestimated, just like what is obtained in section 4.1.

Table 4.4: C_D and C_L from different unstructured mesh sizes.

Mesh	Number of cells	Mean C_D	Mean C_L
1-1	23,606	1.3527	0.1017
1-2	50,597	1.3268	0.1060
1-3	65,100	1.3144	0.1042
1-4	87,364	1.3288	0.1055
1-5	109,295	1.3197	0.1008
1-6	117,285	1.3137	0.1010

From the results, the mean value of C_D and C_L can be regarded converged after the number of cells is larger than 110,000. The variation of C_D and C_L with the time steps is shown in figure 4.21. From the figure, it can be easily seen that the limited linear scheme gives much more stable and accurate results than the linear upwind scheme. Besides, the linear upwind scheme will probably overestimate the coefficients in this case, especially for C_D. Therefore, one probable reason for the overestimation of the coefficients is from the scheme with low accuracy.

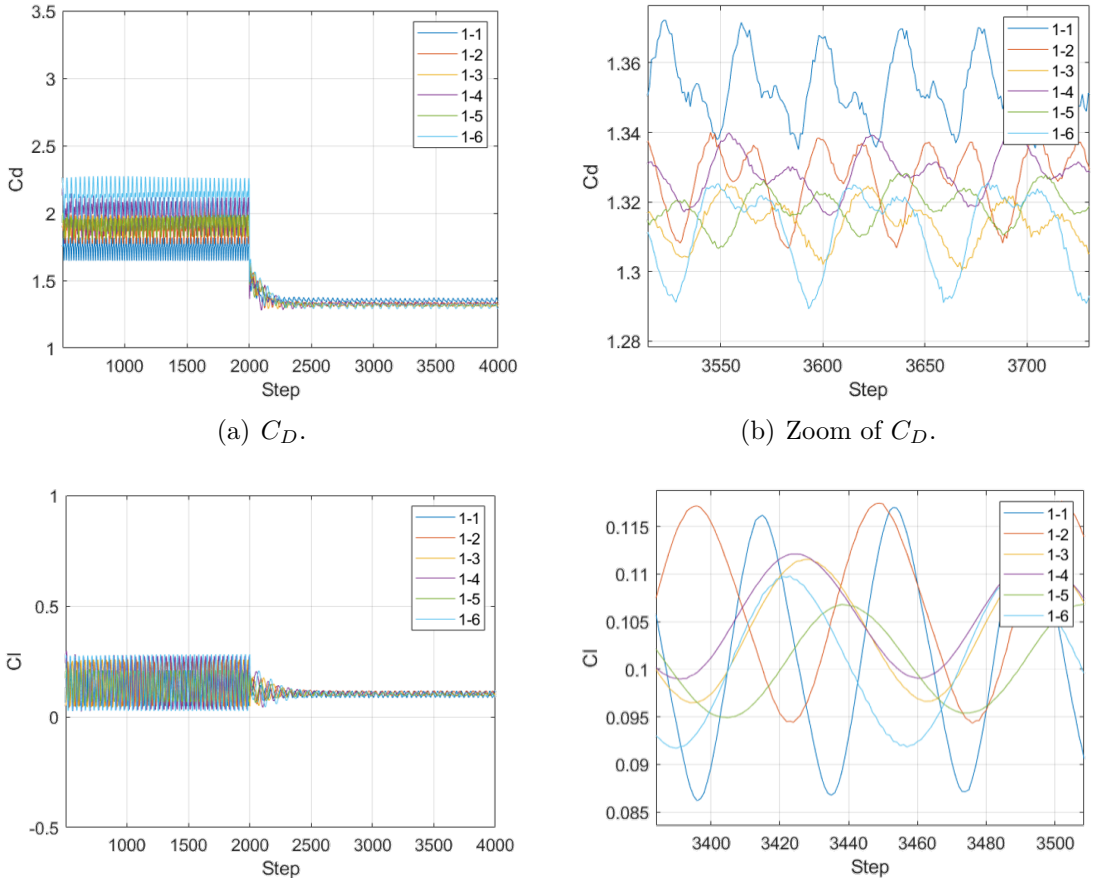

(a) C_D.

(b) Zoom of C_D.

(c) C_L.

(d) Zoom of C_L.

Figure 4.21: Variation of C_D and C_L with the time steps for unstructured meshes.

If schemes with a higher order of accuracy were applied, the results would probably be more accurate. However, schemes with a high order of accuracy have stricter requirements on the mesh. The mesh quality may need to be improved, which will make the simulation case more unstable and easily to get diverged. For this case, as can be seen from the pressure distribution in figure 4.24 from the limited linear scheme, the accuracy of the scheme is considered to be enough.

Although unstructured meshes can reach the mesh independence, usually structured meshes are more controllable and provide more convincing results, as subsection 2.4.3 mentions. Thus, a series of structured meshes is also analyzed in the same way. Figure 4.22 shows an example of a structured mesh. All the domains, including the boundary layer (and its attached region), the downstream region, and outer parts, are using structured mesh.

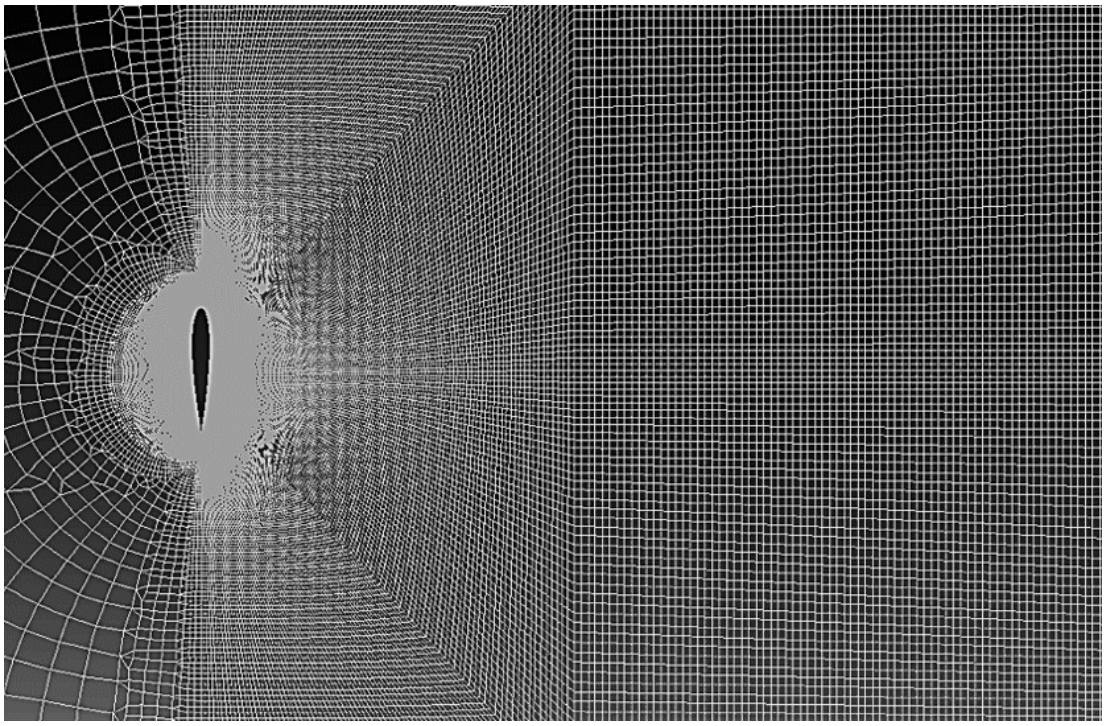

Figure 4.22: Example of a structured mesh, mesh 2-3.

The simulation is carried out by using steady state RANS simulation, i.e. simpleFoam in OpenFOAM. The first 2000 steps are using the linear upwind grad(U) scheme for $\nabla \cdot (\rho UU)$. After the 2000 steps, the limited linear scheme is used for it. Table 4.5 shows the results from different meshes. The mean value is calculated from the steps using the limited linear scheme.

Table 4.5: C_D and C_L from different structured mesh sizes.

Mesh	Number of cells	Mean C_D	Mean C_L
2-1	10,231	1.4291	0.0971
2-2	20,490	1.4554	0.1043
2-3	40,159	1.4387	0.0997
2-4	60,185	1.3438	0.1003
2-5	79,752	1.3442	0.1005
2-6	97,884	1.3163	0.0987
2-7	120,292	1.3738	0.1036
2-8	150,313	1.3906	0.1031
2-9	201,236	1.3878	0.1045

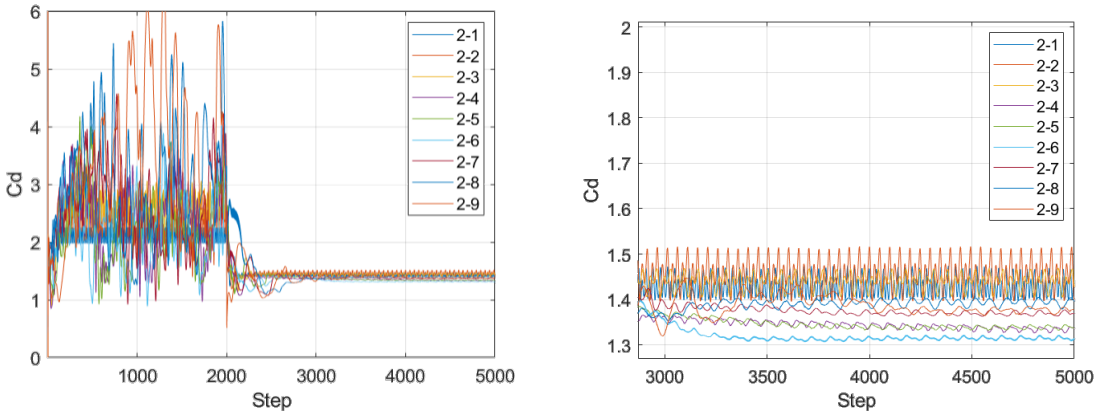

(a) C_D.

(b) Zoom of C_D.

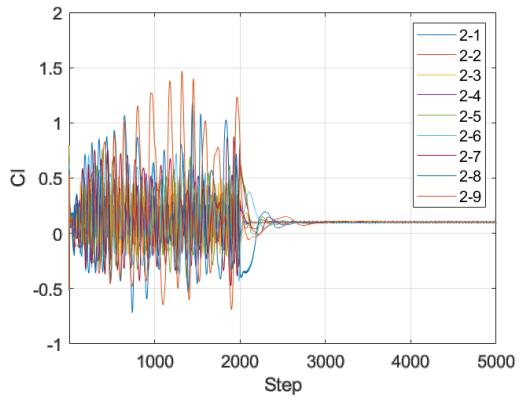

(c) C_L.

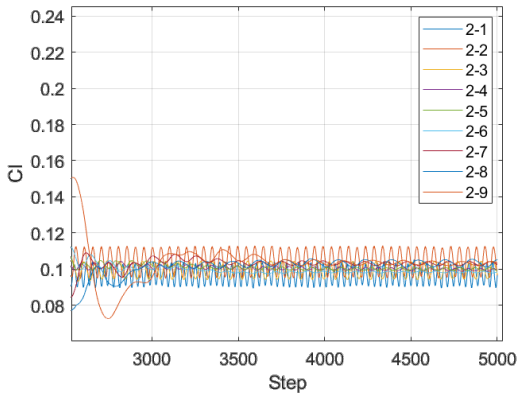

(d) Zoom of C_L.

Figure 4.23: Variation of C_D and C_L with the time steps for structured meshes.

It seems that both C_D and C_L get converged after the number of cells is larger than 120,000. But the results are different from the results from unstructured meshes, as table 4.4 presents. The results from structured meshes are about 4.5% larger than the results from unstructured meshes.

Figure 4.23 shows the variation of C_D and C_L with the time steps. Similar to the analysis results from unstructured meshes, the oscillation of force coefficients can still be found.

In figure 4.23, the coefficients have larger fluctuations than the results from unstructured meshes. With the refinement of the meshes, the amplitude of fluctuation becomes smaller. The reason for the larger fluctuation may be that the continuity between different parts are not solved very well, since the structured meshes are divided into several parts when being generated. The results also support the point that the limited linear scheme gives more accurate results and the linear upwind scheme may overestimate the coefficients. Figure 4.24 shows the pressure (p/ρ) distribution from the two schemes, which indicates that only when using the limited linear scheme, the results reach a more steady state. The scheme study is also mentioned in subsection 4.3.4.

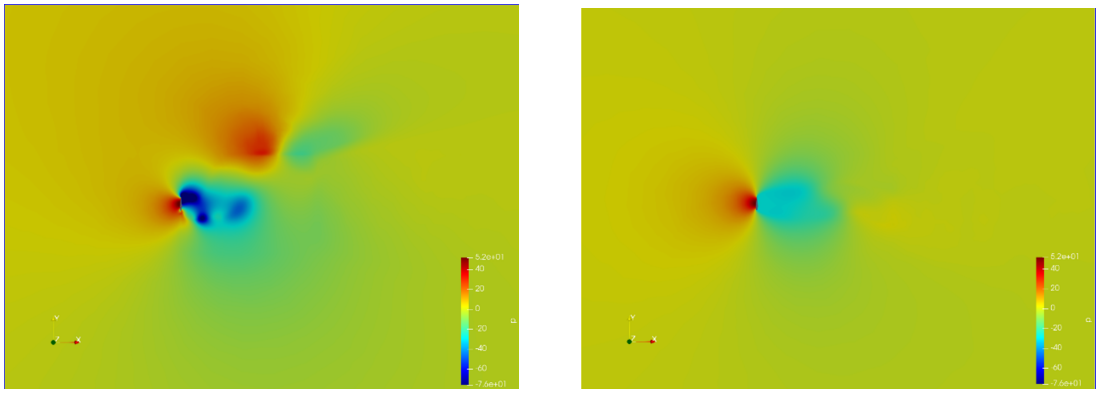

(a) Results using linear upwind scheme. (b) Results using limited linear scheme.

Figure 4.24: Comparison between linear upwind and limited linear schemes.

Figure 4.25 shows the coefficients with the number of cells.

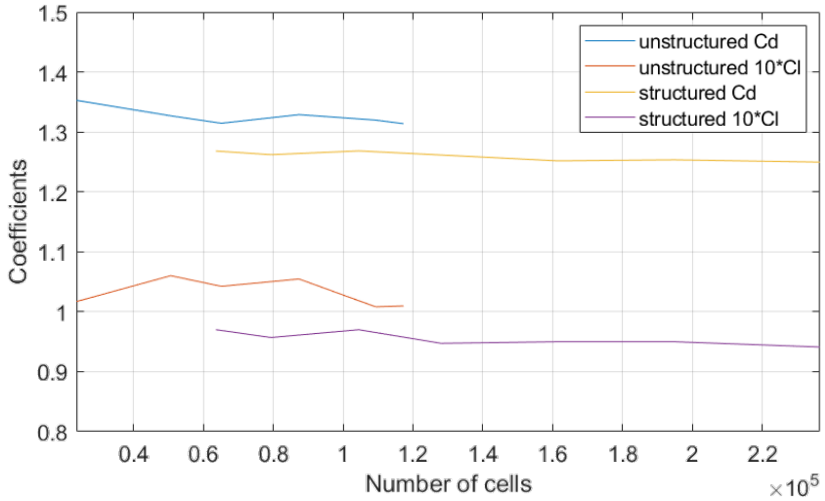

Figure 4.25: Comparison between different mesh sizes.

In figure 4.25, because the force coefficients from the structured meshes converged better than the unstructured meshes. Structured meshes are applied in the final simulation case of a uniform 3D foil, due to its controllability and adjustability. Besides, though the URANS simulation is a bit questionable for this case, it is acceptable.

4.3.2 Unsteady state analysis

In the IDDES simulation, the boundary layer is simulated by the unsteady RANS model. Thus, it's necessary to check the mesh independence by running unsteady state simulations, i.e. pimpleFoam in OpenFOAM. For LES models, the mesh is hard to reach independence. In general, with the refinement of the grid, more and

more fine vorticity structures will be found. Therefore, unsteady RANS simulation is performed for different structured and unstructured meshes.

Figure 4.26 shows the force coefficients from the unstructured mesh analysis through time steps. The mean values of C_D and C_L are summarized in table 4.6. The results support that after the number of cells is larger than around 110,000, the mesh reaches mesh independence regarding the force coefficients.

Table 4.6: C_D and C_L from different meshes.

Mesh	Number of cells	C_D	C_L
1-1	23,606	3.1969	0.1038
1-2	50,597	3.2415	0.0922
1-3	65,100	3.2959	0.0867
1-4	87,364	3.6957	0.0952
1-5	109,295	3.2745	0.0833
1-6	117,285	3.2921	0.0835

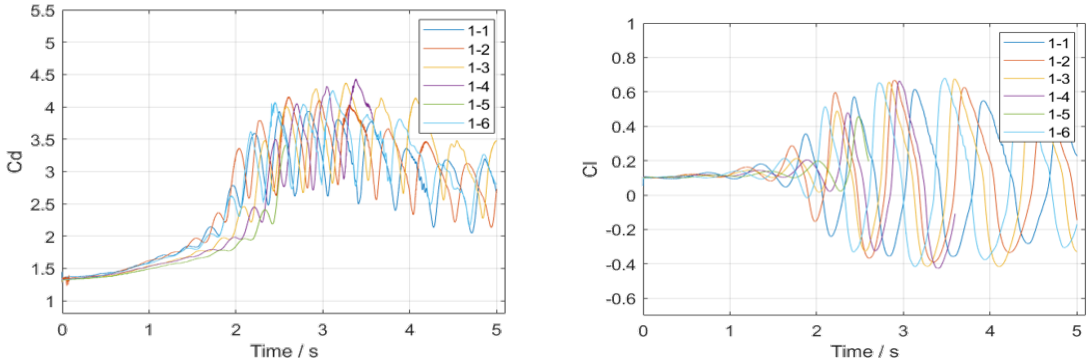

(a) C_D. (b) C_L.

Figure 4.26: Force coefficients through time from different meshes for unsteady state.

A fast Fourier transform (FFT), which is an algorithm that converts a signal from its time domain to a representation in the frequency domain, is performed to analyze the frequency of the vortex shedding from different meshes. Though the mesh reaches mesh independence in the sense of force coefficients, the FFT analysis does not give very ideal results. The peaks are not clear and the values are very small. Perhaps much more time steps are needed to give clear FFT results. Figure 4.27 shows the FFT analysis results of unsteady state mesh analysis with unstructured meshes.

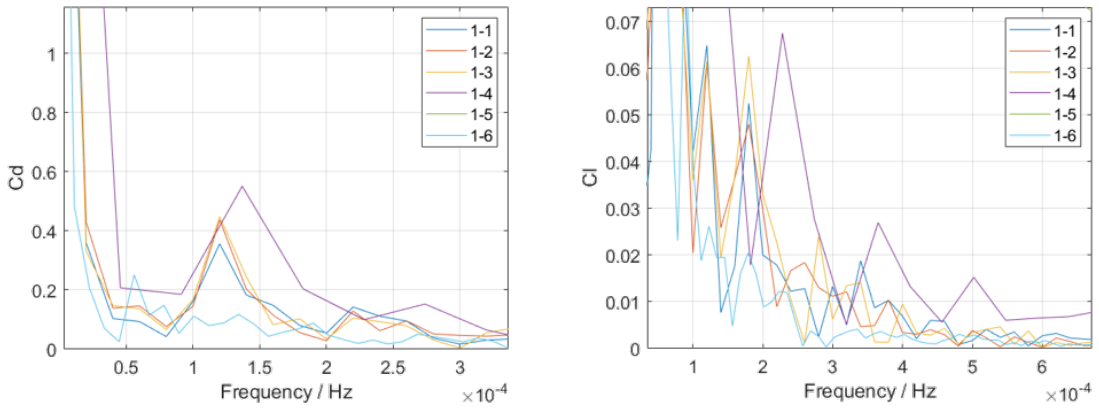

(a) C_D. (b) C_L.

Figure 4.27: FFT analysis for unsteady state mesh analysis.

Unsteady mesh analysis is also carried out for structured meshes. Figure 4.28 shows the force coefficients from the unstructured mesh analysis through time. For each mesh, the lift force coefficient shows a similar amplitude of oscillation. On the other hand, the drag force coefficient shows more fluctuation.

The FFT analysis of the force coefficients, C_D and C_L, from unsteady simulations with structured meshes is presented in figure 4.29 and 4.30. The peaks of the results from the FFT analysis are summarized in table 4.7. It is noticed that regardless of the coefficient chosen, the main frequency, which is the vortex shedding frequency, remains constant at 1.25 Hz. The results from the mesh 2-6 are quite strange, which may because of discontinuity or inappropriate y^+. After removing the data from mesh 2-6, it can be obtained that the frequencies of the peaks become similar when the number of cells is larger than 80,000, i.e. finer than mesh 2-5.

Table 4.7: Peak values of C_D and C_L from FFT analysis, structured mesh unsteady-state simulations.

Mesh	C_D				C_L	
	First peak		Second peak		First peak	
	Frequency	Value*100	Frequency	Value*100	Frequency	Value*100
2-1	1.25	8.26	2.50	33.62	1.25	32.98
2-2	1.00	5.21	2.25	27.45	1.25	33.23
2-3	1.25	6.15	2.25	34.52	1.25	30.71
2-4	1.00	12.34	2.25	25.47	1.25	37.40
2-5	1.25	14.62	2.25	23.89	1.25	35.32
2-6	1.25	14.02	2.50	9.07	1.50	27.27
2-7	1.25	12.35	2.25	24.66	1.25	37.99
2-8	1.25	8.73	2.25	27.63	1.25	32.39
2-9	1.25	7.50	2.25	25.40	1.25	35.76

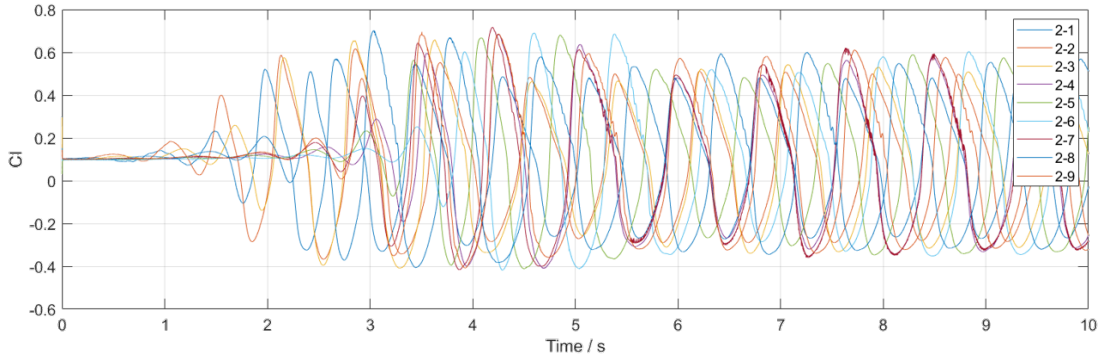

(a) C_L.

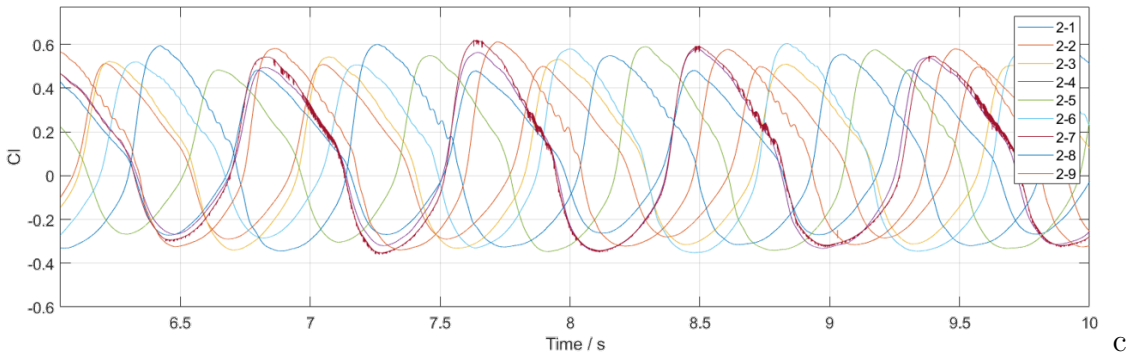

(b) Zoom of C_L.

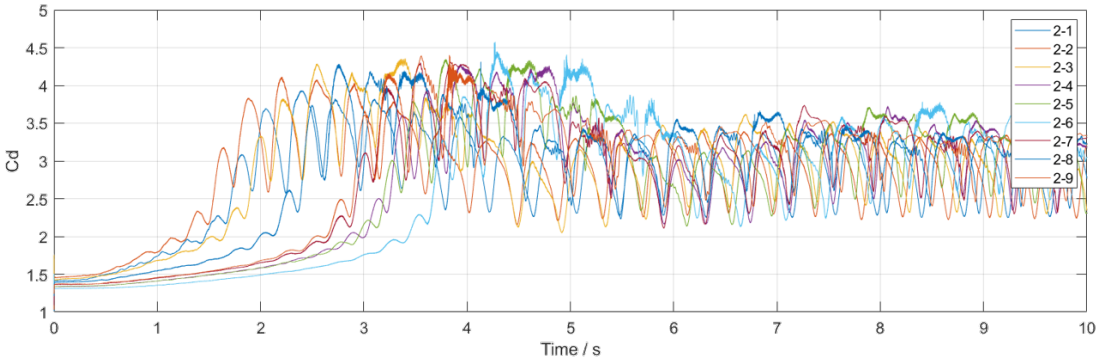

(c) C_D.

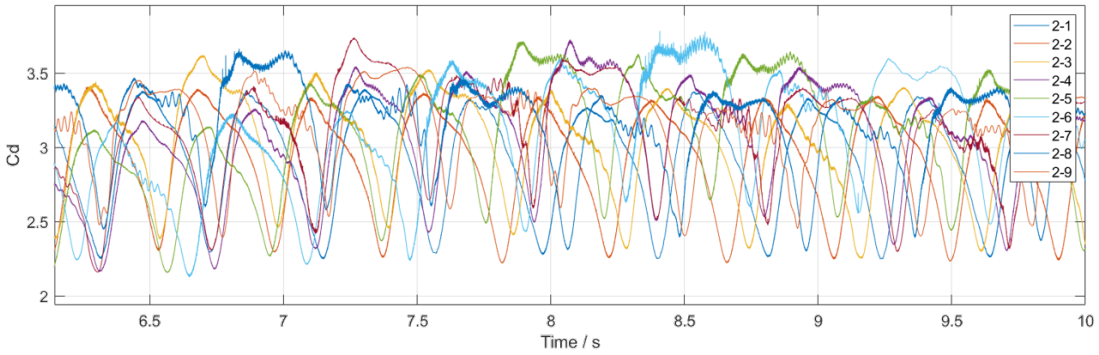

(d) Zoom of C_D.

Figure 4.28: Force coefficients from unsteady mesh analysis with structured meshes.

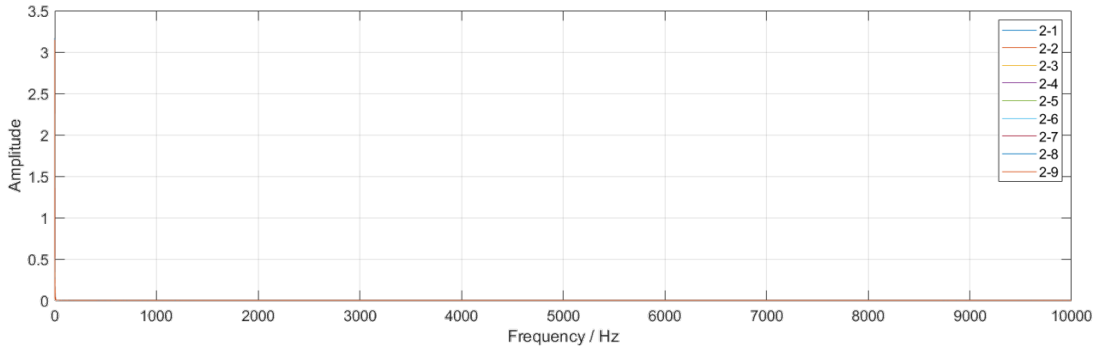

(a) C_D FFT.

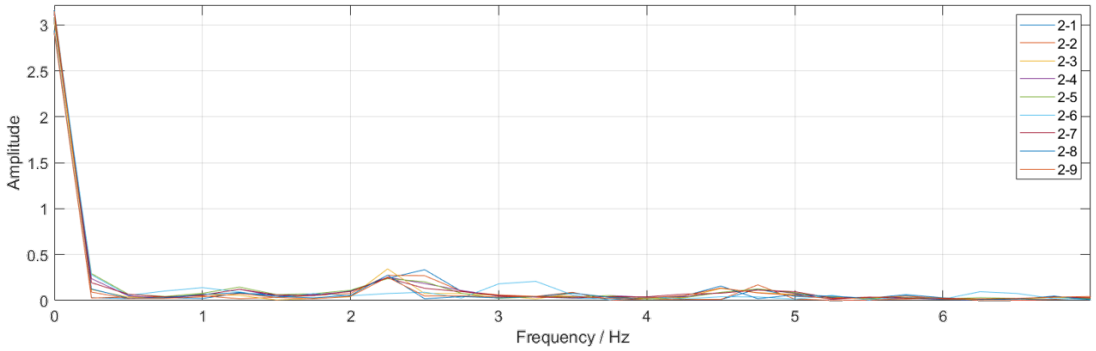

(b) Zoom of C_D FFT.

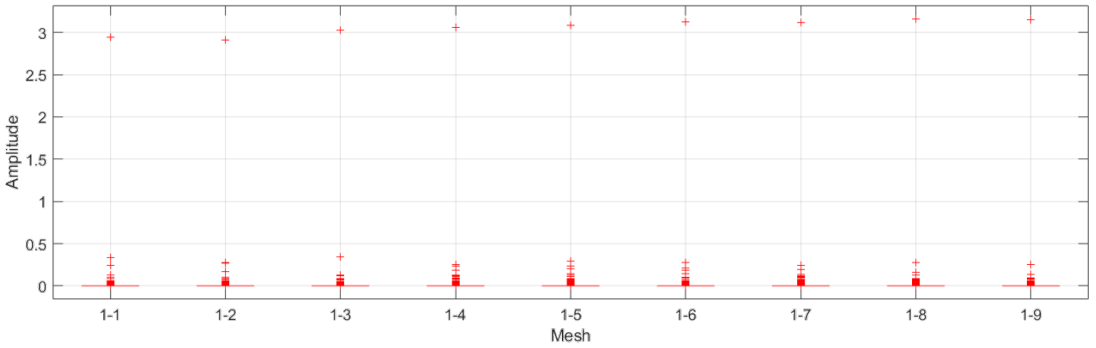

(c) C_D FFT boxplot.

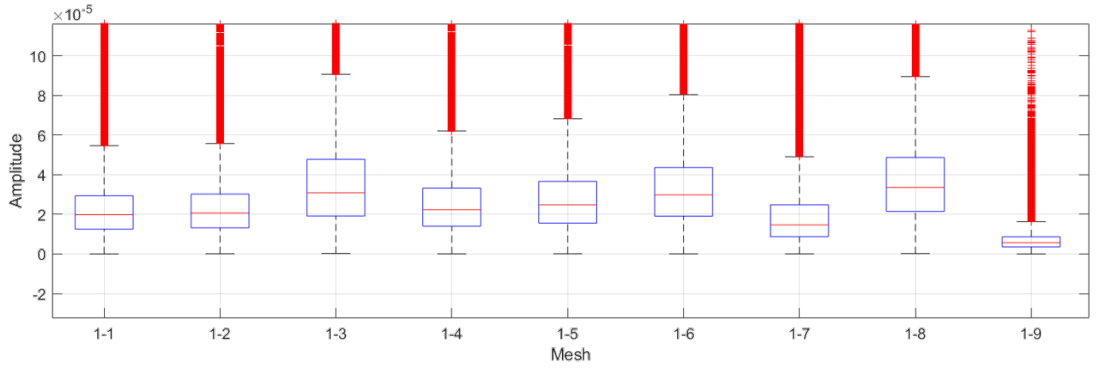

(d) Zoom of C_D FFT boxplot.

Figure 4.29: FFT analysis of C_D from unsteady mesh analysis with structured meshes.

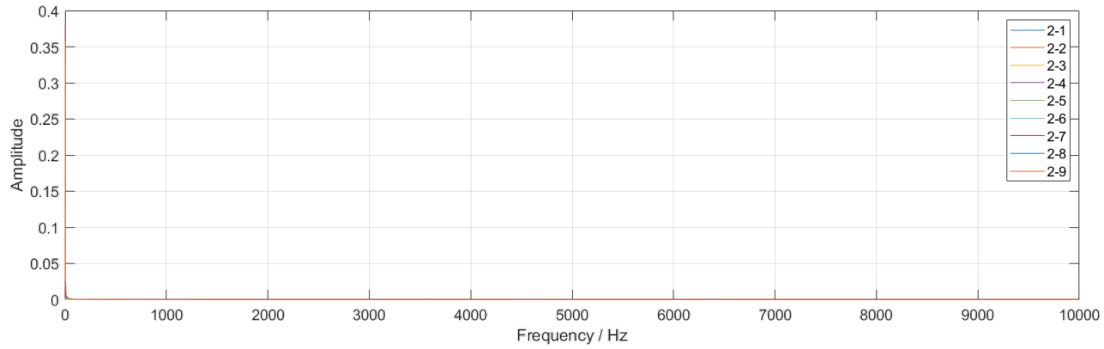

(a) C_L FFT.

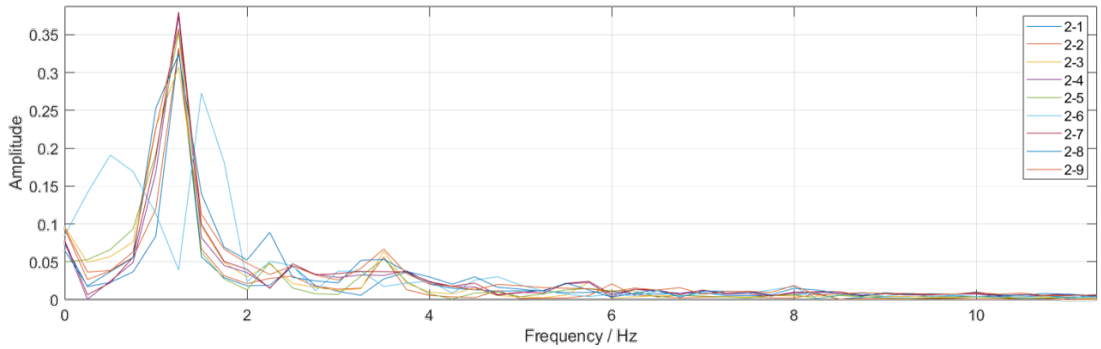

(b) Zoom of C_L FFT.

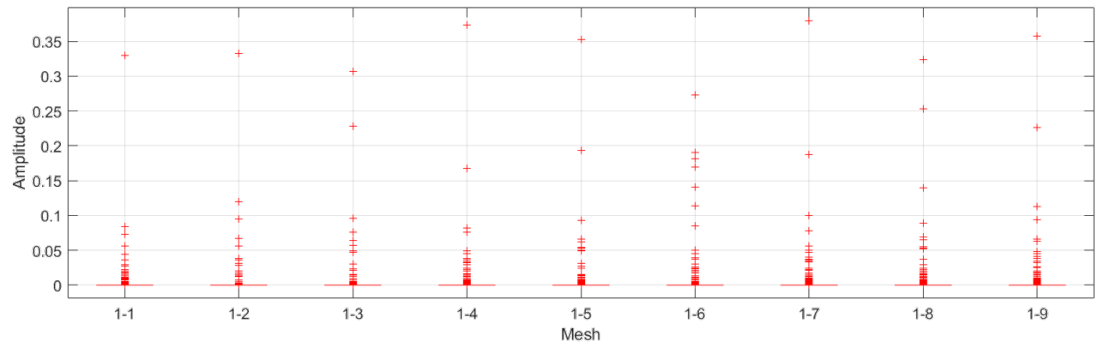

(c) C_L FFT boxplot.

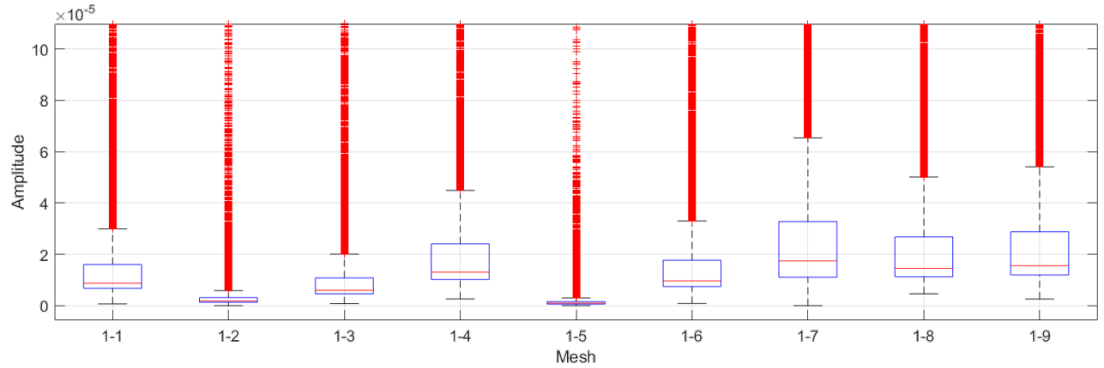

(d) Zoom of C_L FFT boxplot.

Figure 4.30: FFT analysis of C_L from unsteady mesh analysis with structured meshes.

4.3.3 Scheme-revised simulation

From the scheme study in section 4.3, it is obtained that the accuracy of schemes will have a significant influence on the deep stall simulation. In section 4.3, the drag force coefficients, C_D, are overestimated when using schemes with a low order of accuracy. Thus, the schemes are modified. The scheme for $\nabla \cdot \rho UU$ is changed from linear upwind to limited linear, and the time scheme is changed from Euler (first-order accuracy) to backward (second-order accuracy). The simulation case of the fine mesh is re-run.

In this case, the Courant number in the LES region is less than 1, and y^+ is less than 1 most of the time.

However, the simulation still overestimates the force coefficients. Figure 4.31 presents the force coefficients through time, and table 4.8 summarizes the mean value of C_D and C_L. Though the force coefficients become closer to the experimental data compared with previous results in section 4.2, the disagreement still cannot be ignored.

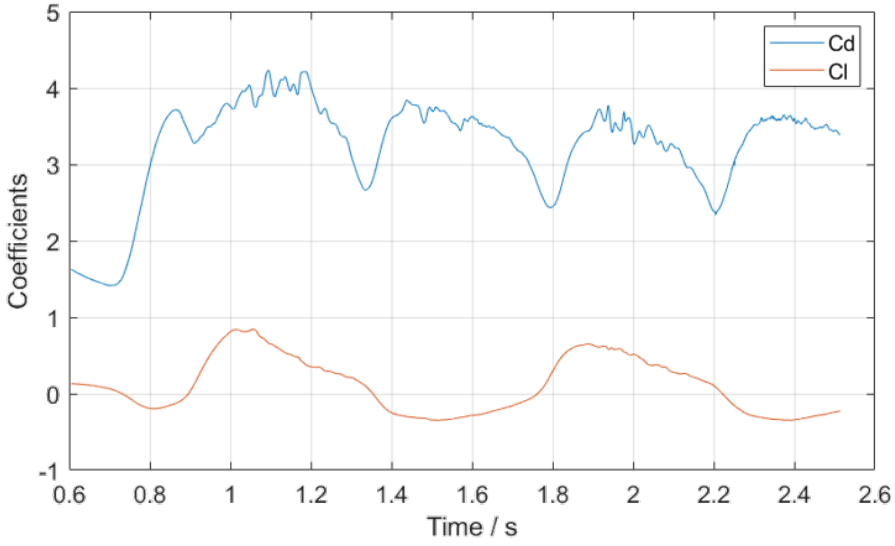

Figure 4.31: Force coefficients through time after scheme modification.

Table 4.8: C_D and C_L after scheme modification.

Coefficients	Simulation before revision	Simulation after revision	Experiment	Difference
C_D	3.392	3.124	1.800	74%
C_L	0.167	0.127	0.090	41%

This case indicates that though scheme accuracy and 2D mesh independence have an influence on the results, they are not the most important reason for the overestimation.

4.3.4 3D mesh analysis

In order to check if the cell size in z direction is fine enough, 3D mesh analysis is also executed. Based on unstructured mesh 1-5, two 3D meshes are generated with 60 and 120 layers in the z direction. The total height, i.e. the longitudinal length, of the foil is the same as the chord length i.e. 1m.

In 2D mesh analysis, it is found that the accuracy of the schemes has a significant influence on the results. This phenomenon is also found in the 3D analysis. Figure 4.32 shows the pressure (p/ρ) distribution at the front panel from linear upwind and limited linear schemes. It can be seen that when using the linear upwind scheme, there are some regions with extremely low pressure, which will cause high drag force coefficients. This situation does not exist when the limited linear scheme is applied. Thus the simulation will be more reasonable when using limited linear schemes.

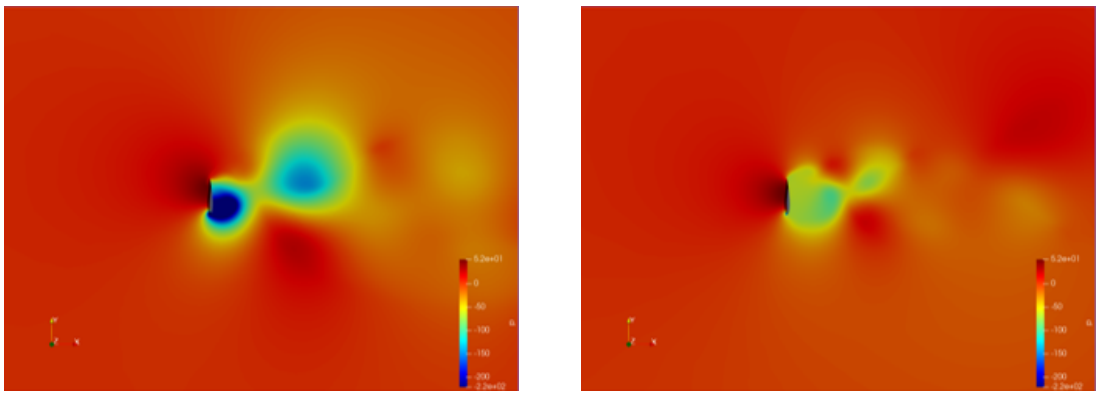

(a) Results using linear upwind scheme. (b) Results using limited linear scheme.

Figure 4.32: Comparison between linear upwind and limited linear schemes.

One of the problems that 3D simulation faces is that there are always cells with high aspect ratio. To solve this, controlling $y^+ < 1$ is given up, instead, y^+ is made to be larger than 30. Then, the boundary condition of K at wall needs to be changed to be kqrWallFunction.

Another probable reason for the inaccuracy might be the mesh at both the trailing edge and the leading edge is not fine enough, which results in the high Courant number at edges.

4.4 Final 3D simulation

In section 4.3, results and cause analysis for inaccuracy are presented. The possible reasons are listed as: y^+ at wall is inappropriate; mesh is not fine enough to reach its independence; the scheme is not accurate enough; aspect ratio of cells is too high; the condition is not the same as experiments. A final 3D simulation is performed after solving all the problems mentioned above.

4.4.1 Mesh refinement

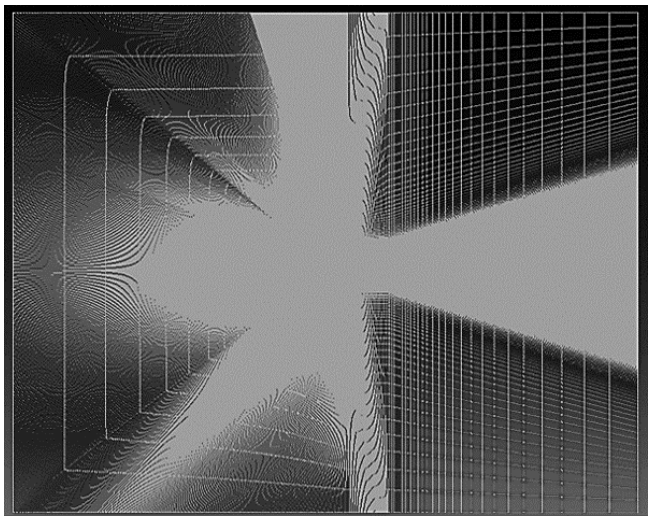

(a) Entire domain.

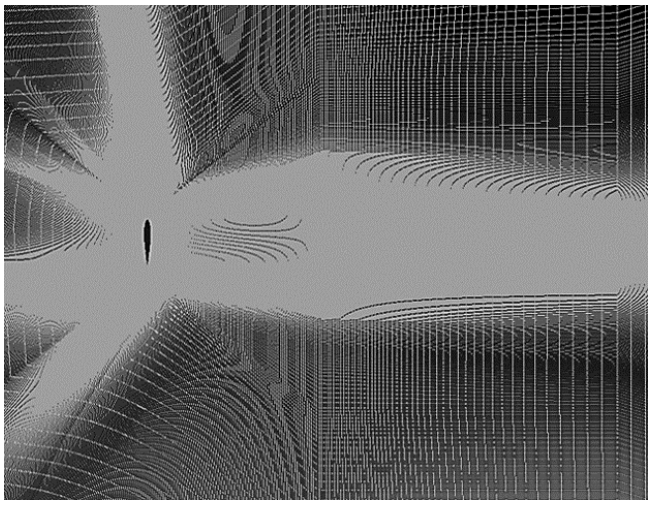

(b) Downstream region.

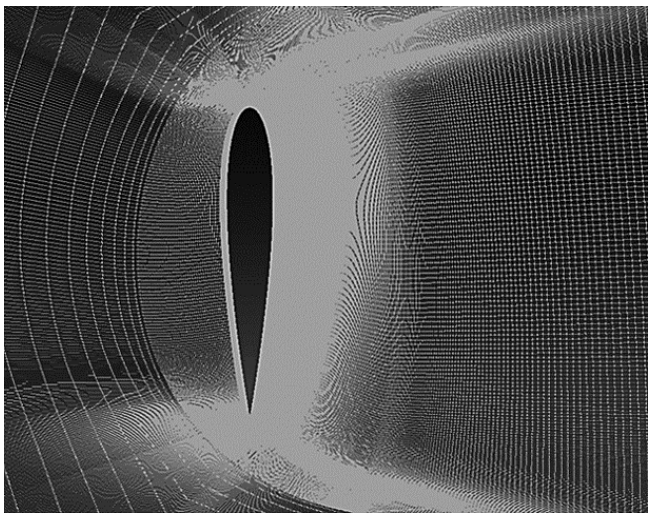

(c) Close to the foil.

Figure 4.33: Mesh used for the final 3D uniform simulation.

J. S. Park (2017) indicated that when doing simulation for deep stall foils, the height (length in z direction) should be quite larger than the chord length [42]. Otherwise, the force coefficients may be overestimated. According to the reference, to get accurate force coefficients, the ratio between the longitudinal length and the chord length is better to be larger than 4. But the experiment data which is compared with the simulation results is based on a foil with $height/chordlength = 2.33$. Therefore, the final simulation is trying to follow the experiments, with the ratio of height and chord length as 2.33. The front and back boundary is changed to be walls instead of cyclic.

For the new mesh, all of the domain is structured, as figure 4.33 shows. It can be seen that the mesh at the two tips is refined compared with the previous mesh as figure 4.8. The total number of cells is 24,148,320. In z direction, 120 layers are evenly set. Wall functions are applied as the wall normal resolution on the side walls.

4.4.2 Steady state results

A simulation of steady state with the $k-\omega$ SST model is performed to provide the initial condition for IDDES.

The simulation is initialized with a more diffusive scheme, i.e. linear upwind for the $\nabla \cdot \rho UU$ term for the first 700 time steps. After that, a more accurate scheme, limited linear, is used and the force coefficients C_D and C_L are collected. The predicted mean values of C_D and C_L are 1.562 and 0.150, with a relative difference of -13.2% and 66.7% compared with experimental measurements.

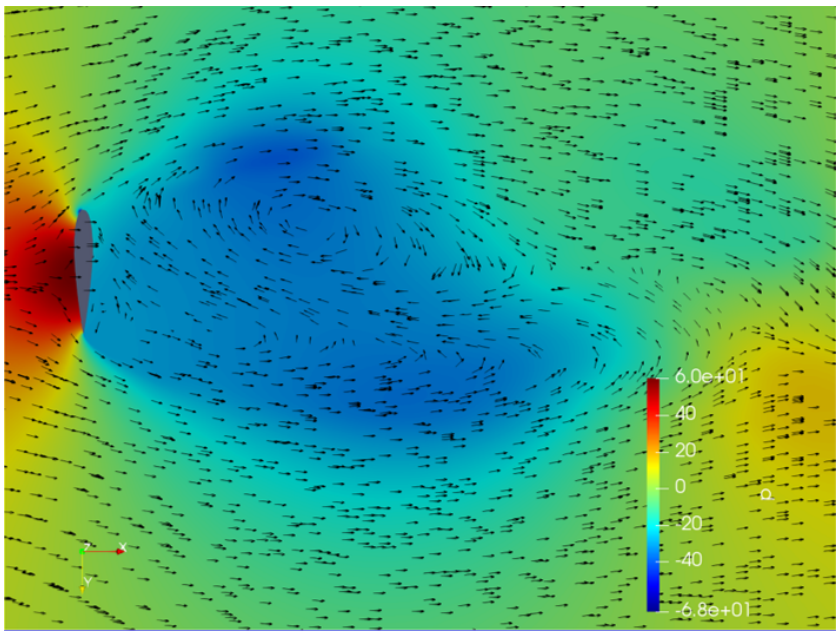

Figure 4.34: Pressure (p/ρ) and velocity direction distribution, final 3D steady state RANS simulation.

The pressure (p/ρ) distribution and the vectors which represent the velocity direction at the foil center panel are shown in figure 4.34. Added mass can be found in front of the foil, and vortices occur with low-pressure region in the downstream. The flow field is similar to the 2D simulation results, which can be seen in section 4.1.

Figure 4.35 shows the velocity distribution, significant flow in z direction can be detected. Compared with results in subsection 4.2.4, flow in the longitudinal direction not only appears in the attached region around the foil, but also in far downstream fields.

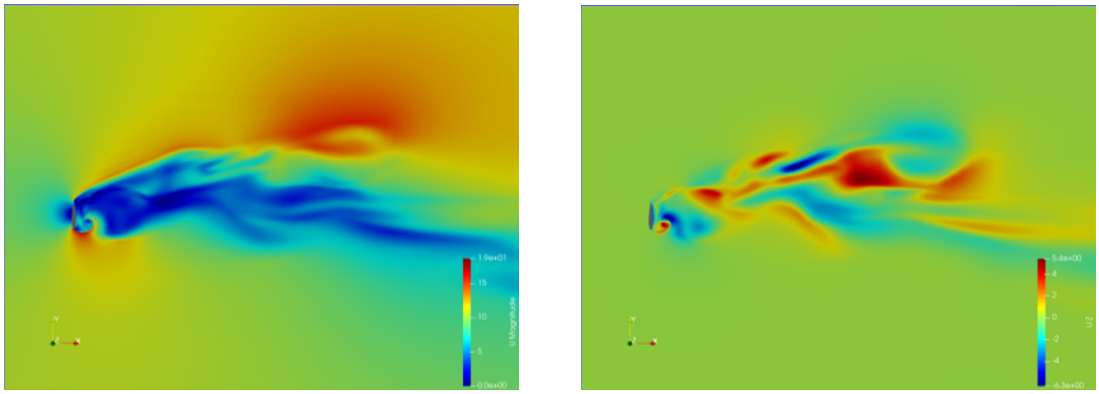

(a) Magnitude. (b) Z direction.

Figure 4.35: Velocity distribution, final steady state 3D simulation.

4.4.3 IDDES simulation results

The IDDES simulation is based on the same process as the re-run case in subsection 4.3.3. Since the mesh is rather fine and with maintaining the Courant number in the LES region less than 1, it is too time-consuming, and only limited results are generated.

The variation of the force coefficients through time is noticed in figure 4.36. In the limited time, the mean value of the force coefficients are $C_D = 1.725$ and $C_L = 0.117$. The difference of C_D to the experimental data is -4.2 %, and 3.2 % for C_L. The overestimation of C_D does no longer exist, and the deviation from the experimental data is now acceptable.

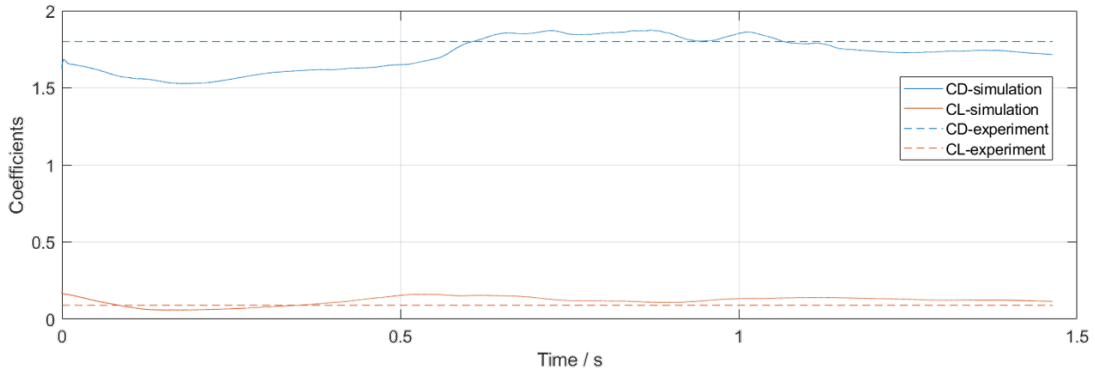

Figure 4.36: Force coefficients with time, final 3D IDDES simulation.

The development of the DES field is shown in figure 4.37. The boundary layers are in the RANS region, which presented in blue, and most of the flow separation and vortices are calculated by the LES model, which is shown in red in the figure.

(a) $t = 0.25$ s. (b) $t = 0.70$ s. (c) $t = 1.15$ s.

Figure 4.37: Velocity distribution.

Figure 4.38 and figure 4.39 show the pressure (p/ρ) distribution and the surface LIC at different time. Figure 4.40 shows Q around the foil at the foil center plane at different times. The development of the vortex street can be easily seen in both the three figures. Compared with the previous simulation cases in section 4.2, the flow field shows a much more complex vorticity structure. Quantities of small vortices can be found around the foil.

From the surface LIC results, significant flow separation can be seen in the downstream field. The flow separation can also be found in figure 4.41 which shows the 3D vector plot of the velocity field. When $t = 1.15$ s, the main vortices break into several small vortices. Meanwhile, the vortices dissipate more quickly than the preliminary 3D simulation cases, which is probably because of the influence of the front and back wall. The pressure (p/ρ) distribution at different distances from the back wall is shown in figure 4.42. For the slice at 99% of the chord length, the main vortices are quite complete, while the main vortices become broken for slices close to the foil center plane.

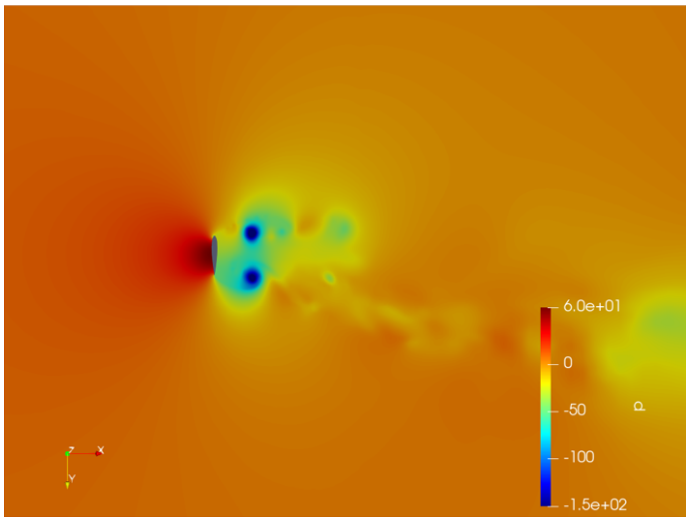

(a) $t = 0.25$ s.

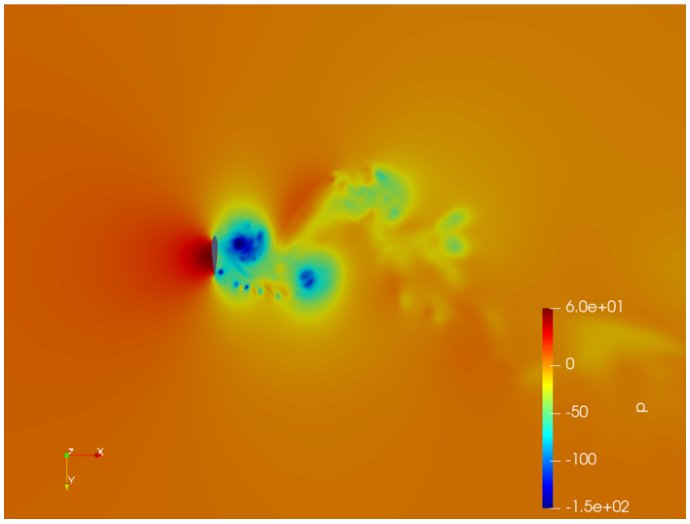

(b) $t = 0.70$ s.

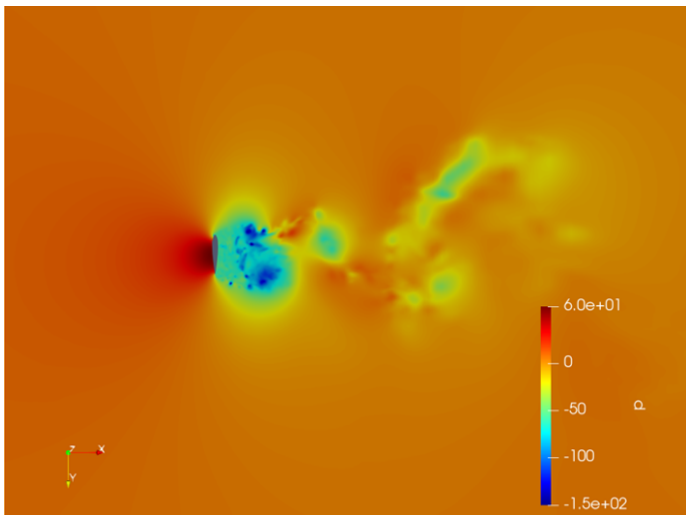

(c) $t = 1.15$ s.

Figure 4.38: Pressure (p/ρ) distribution at the foil center plane, final 3D IDDES simulation.

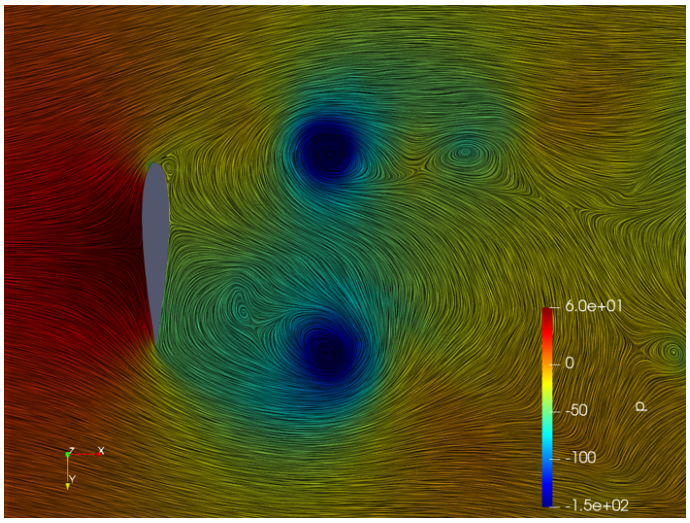

(a) $t = 0.25$ s.

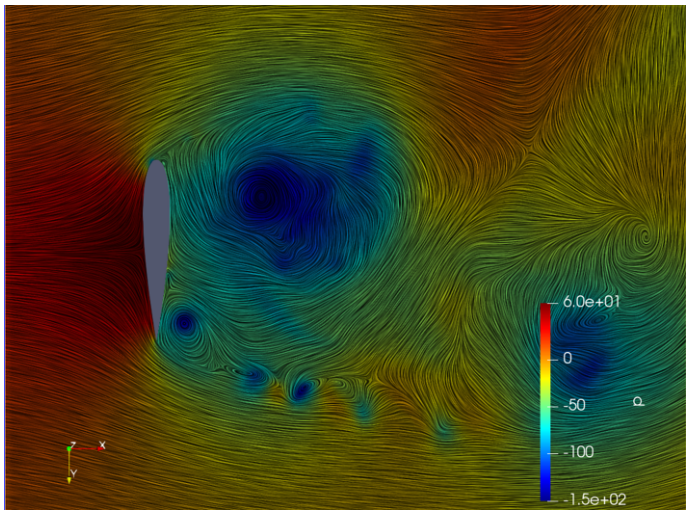

(b) $t = 0.70$ s.

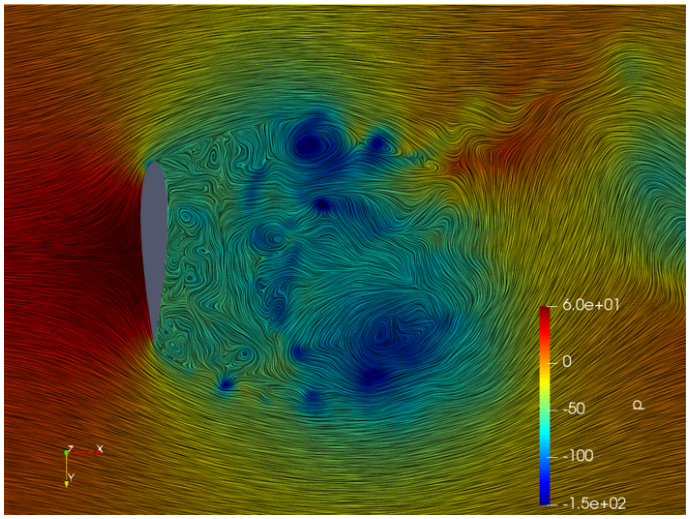

(c) $t = 1.15$ s.

Figure 4.39: Zoom of pressure (p/ρ) distribution and the surface LIC at the foil center plane, final 3D IDDES simulation.

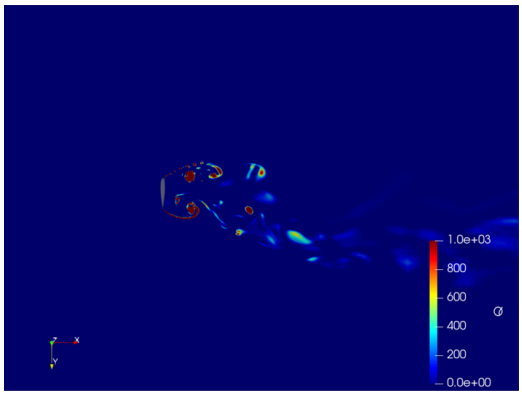

(a) $t = 0.25$ s.

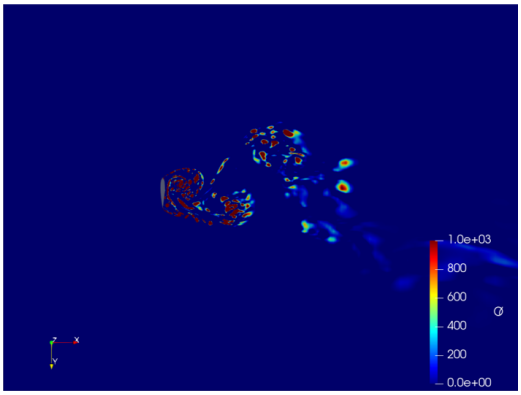

(b) $t = 0.70$ s.

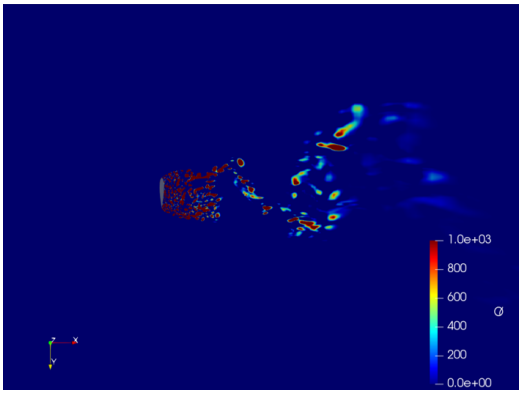

(c) $t = 1.15$ s.

Figure 4.40: Distribution of Q, final 3D IDDES simulation.

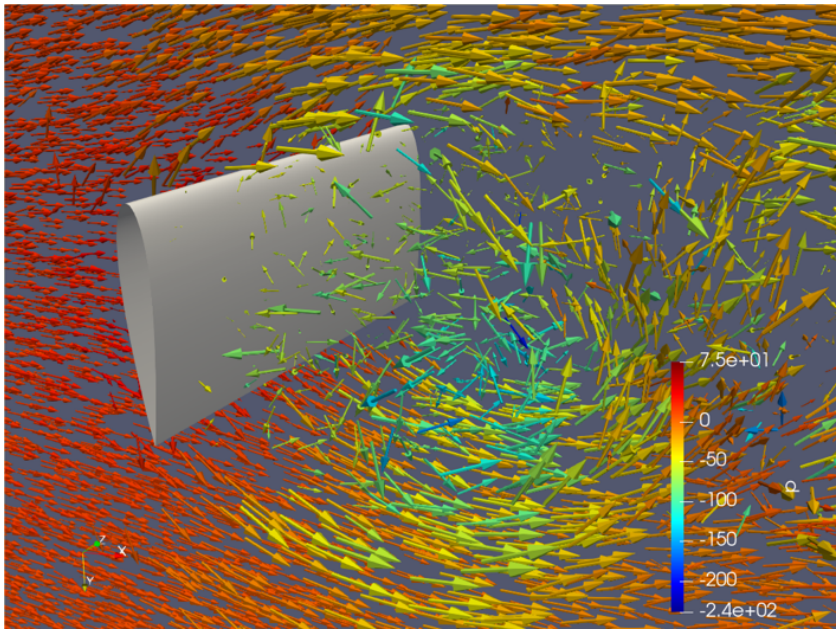

Figure 4.41: 3D velocity vector plot, final 3D IDDES simulation.

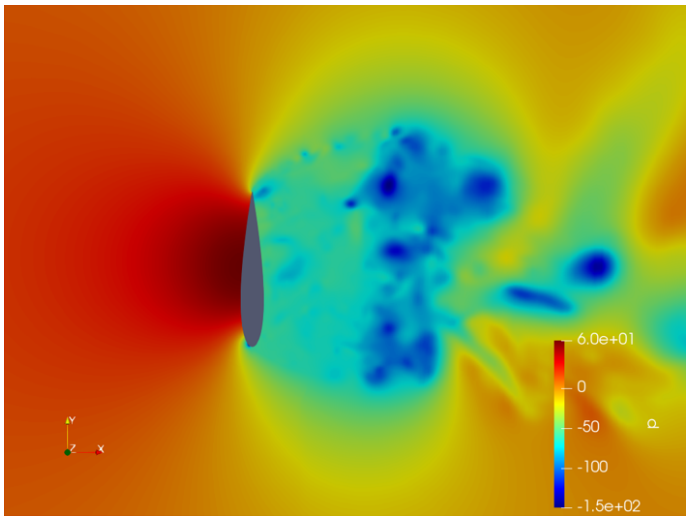

(a) $y = 70\%$ chord length.

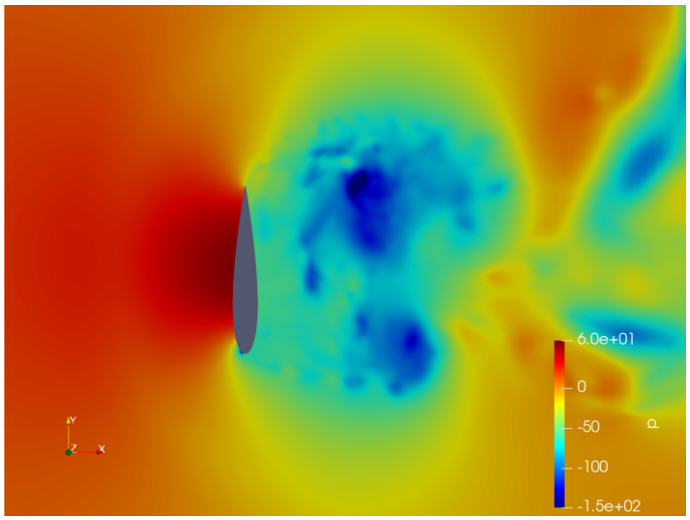

(b) $y = 90\%$ chord length.

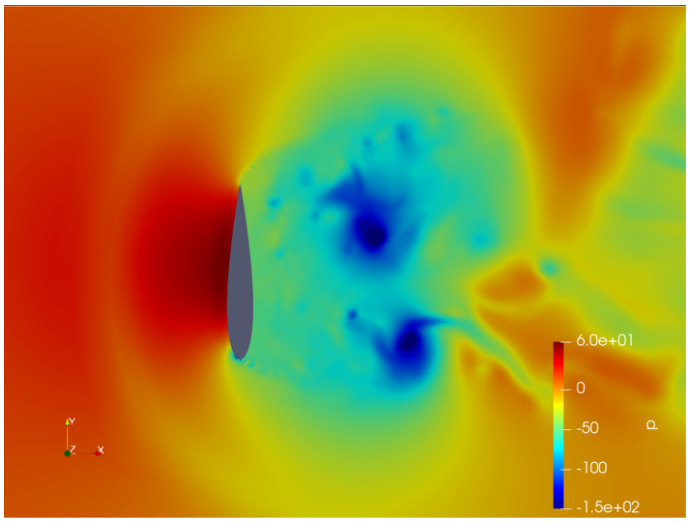

(c) $y = 99\%$ chord length.

Figure 4.42: Distribution of Q, final 3D IDDES simulation.

The pressure (p/ρ) distribution at different slices behind the foil with $t = 1.25$ m is presented in figure 4.43. The white frame in the figure refers to the projection of the foil in x direction, i.e. the inlet flow direction. It can be seen that the longitudinal pressure distribution is not uniform. Though the foil is uniform and symmetric, the flow field is quite irregular. The width of the irregular flow filed is almost the same as the chord length when $x = 1$ m, i.e. 10 % of the chord length. However, the irregular flow field will become wider as the distance from the foil is getting larger and larger.

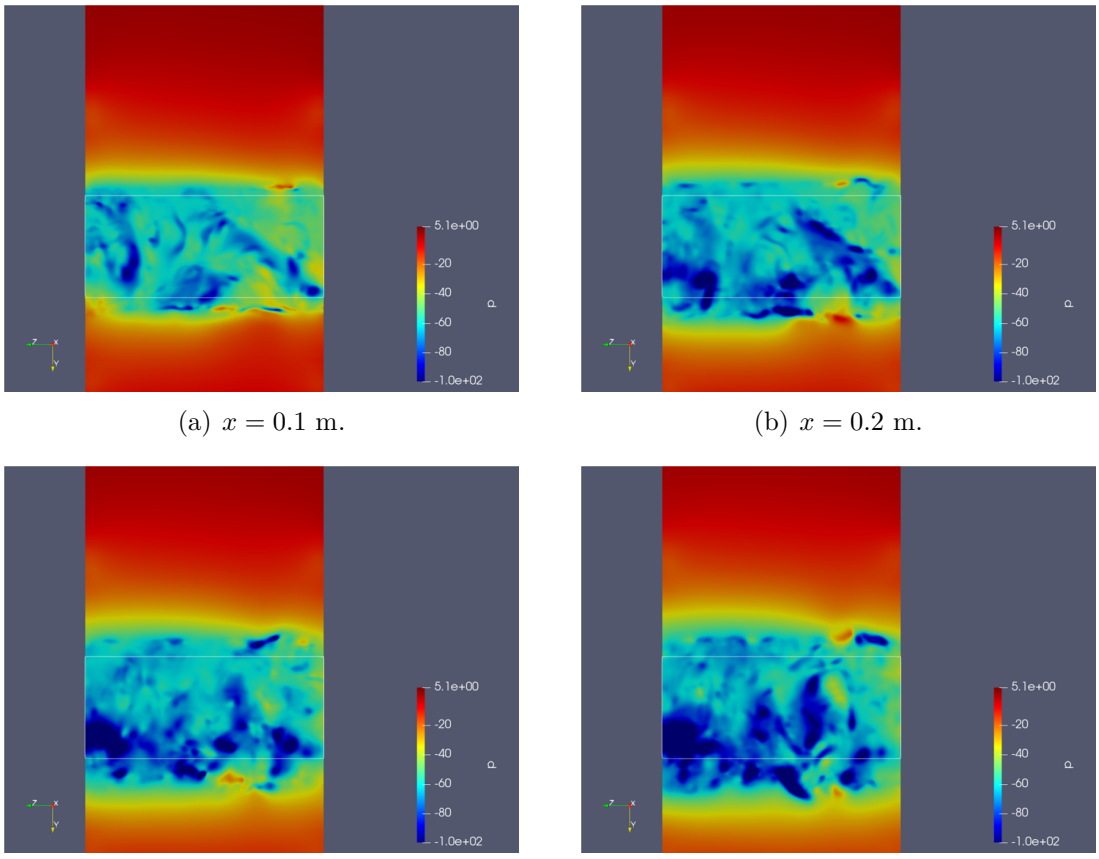

(a) $x = 0.1$ m. (b) $x = 0.2$ m.

(c) $x = 0.3$ m. (d) $x = 0.4$ m.

Figure 4.43: Pressure distribution at different slices behind the foil.

Figure 4.44 shows the velocity distribution at the foil centre plane with $t = 1.15$ m. Similar to the results from the preliminary 3D simulation in section 4.2, the velocity in the z direction is in the same order of magnitude as velocity in the x and y directions. However, the longitudinal flow not only appears in the region tightly attached with the foil, but also the downstream region far away from the foil, which is also revealed by steady state simulation in subsection 4.4.2.

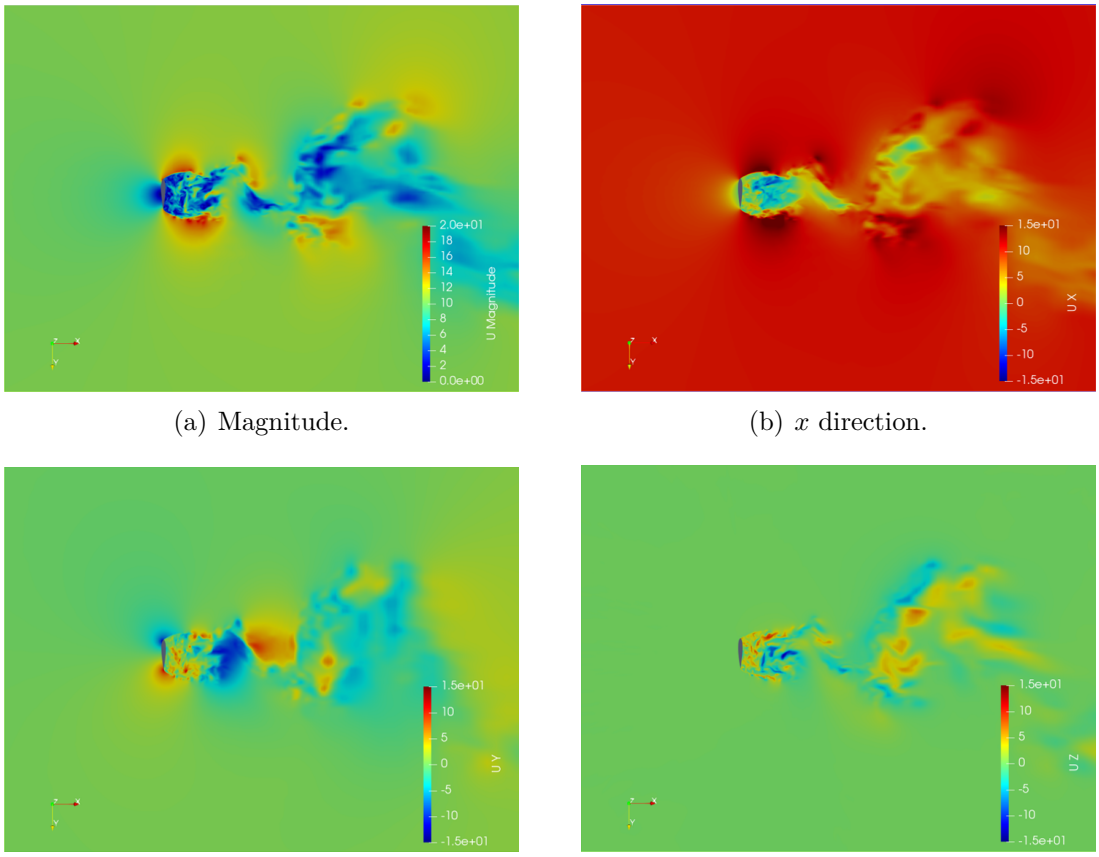

(a) Magnitude.

(b) x direction.

(c) y direction.

(d) z direction.

Figure 4.44: Velocity distribution, final 3D uniform IDDES simulation.

The predicted vorticity, as shown in figure 4.45, is found to be stronger than in figure 4.15 which is predicted using a short foil span. This indicates that with the inclusion of a longer foil in the simulation, the prediction of 3D flow structures will be different which will lead to different force predictions.

Figure 4.46 shows the distribution of pressure (p/ρ) and velocity in z direction throughout the contour of $Q = 50$. The low-pressure phenomenon at the suction side is milder, and the 3D flow structure is more complex than the previous simulation results in section 4.2.

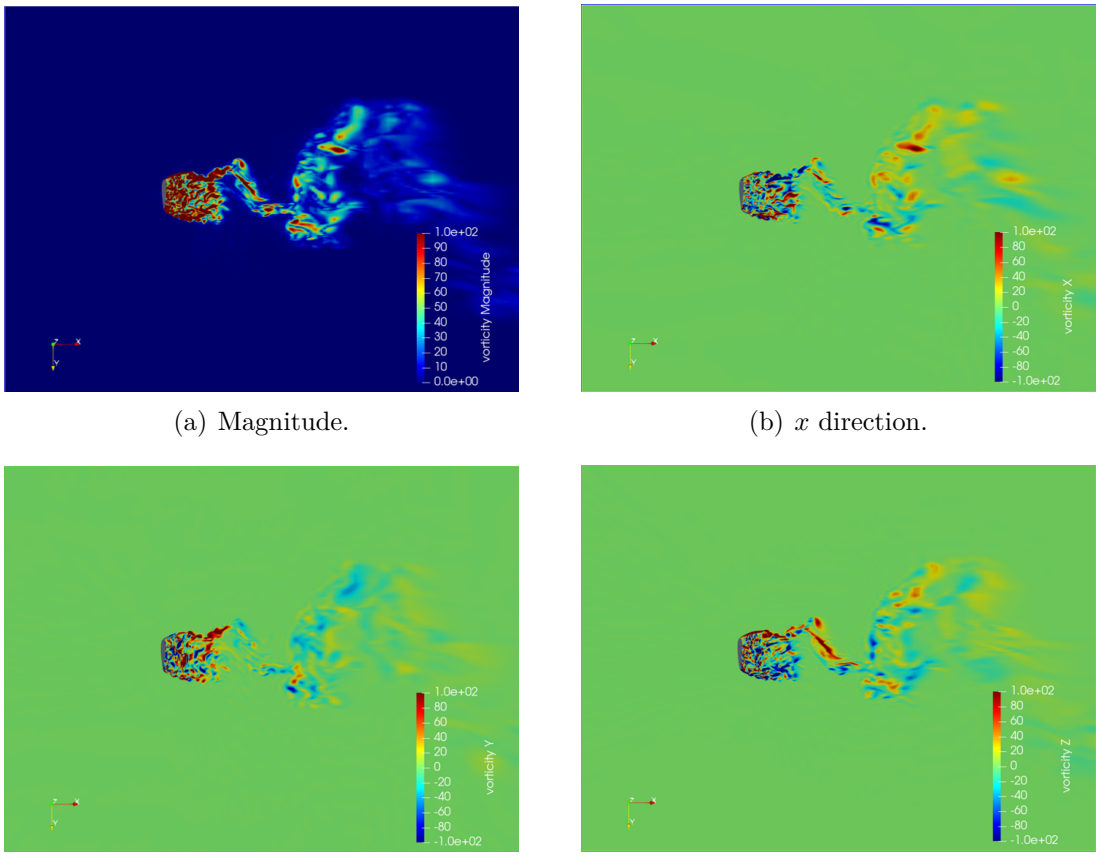

(a) Magnitude. (b) x direction.

(c) y direction. (d) z direction.

Figure 4.45: Vorticity distribution, final 3D uniform IDDES simulation.

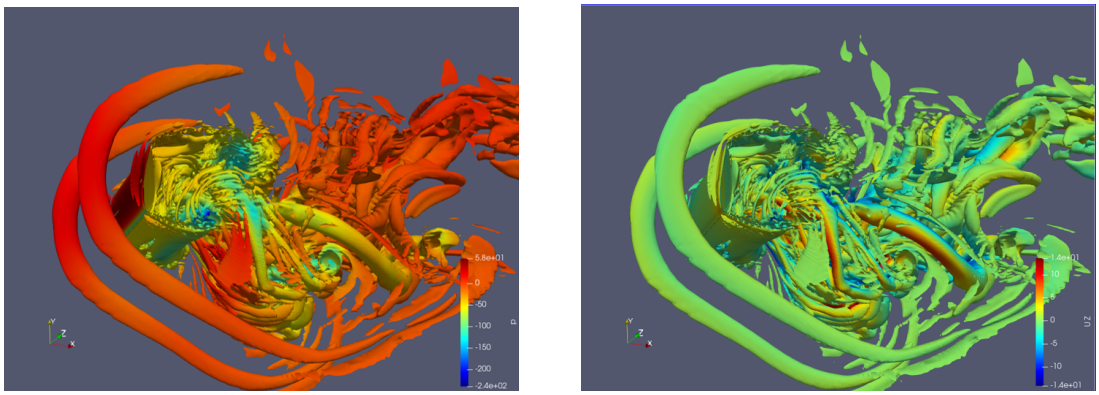

(a) Pressure. (b) Velocity in z direction.

Figure 4.46: Pressure and velocity in z direction throughout the contour of $Q = 50$ with $t = 1.15$ s, final 3D uniform IDDES simulation.

The overestimation of force coefficients is lightened from this case. The ignorance of the influence from the sidewalls, i.e. the wall at the front and back panel, is considered as the probable reason to the overestimation. Nevertheless, it must be

admitted that since the limitation of time steps, it cannot be firmly believed that this mesh and simulation process is perfect, though the results have much better agreement with the wind tunnel experiment results than the preliminary simulation cases.

From the final simulation case of the uniform 3D foil, significant influence from the front and back walls is discovered. Although the simulation follow the condition of the experiments and the results fit the experimental data quite well, the predicted flow field may not be representative of a foil under the extreme condition. Usually people are interested in the force coefficients and other feature of the flow field without the influence from sidewalls. Thus, simulations based on a uniform 3D foil with infinite span wise length may have more reference value.

4.5 Interactions between two foils

A 2D simulation is carried out to give a rough prediction on the interaction between two foils. The case is based on two foils both with a 90° angle of attack and different distances in between. The Reynolds number in this section is all set to be 1e7, based on the chord length.

Figure 4.47 show the pressure (p/ρ) distribution of each simulation case with the distance between the two foils from 1.0 × chord length to 3.5 × chord length. When the distance between the two foils is less than 2.0 × chord length, the pressure distribution is quite stable. There is a relatively uniform low-pressure area between the two foils. Nevertheless, when the distance between the two foils is larger than 2.5 × chord length, some unstable low-pressure region will occur between the two foils, and the loading condition of the 2-foil system will show its volatility.

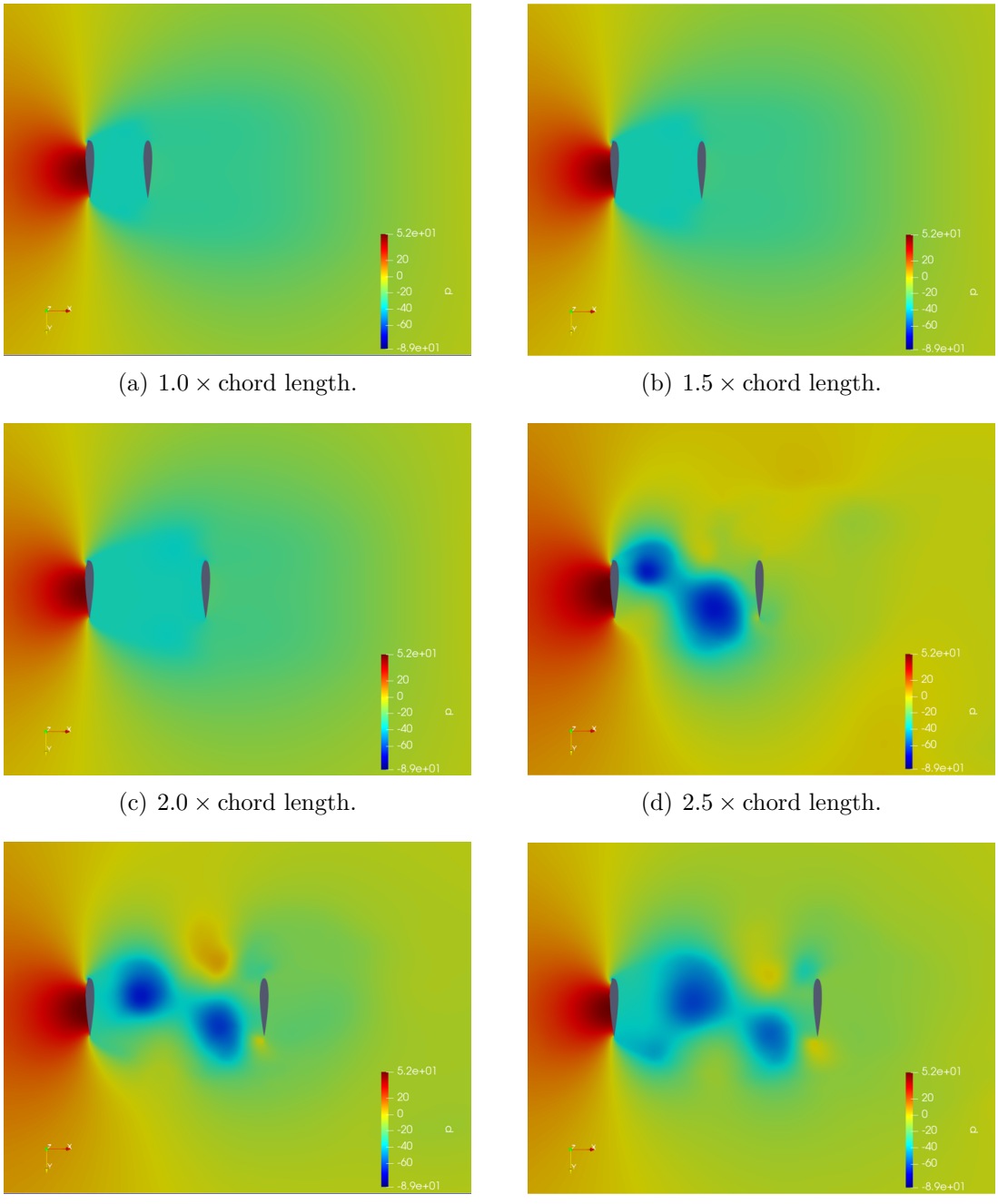

(a) 1.0 × chord length.

(b) 1.5 × chord length.

(c) 2.0 × chord length.

(d) 2.5 × chord length.

(e) 3.0 × chord length.

(f) 3.5 × chord length.

Figure 4.47: Pressure (p/ρ) distribution, 2D steady state RANS simulation for 2 foils with different distances in between.

Since the flow field of these simulation cases with deep stall foils has lots of unsteady characters. In purpose of predicting the flow separation and vorticities, IDDES simulations are carried out. Figure 4.48 and figure 4.49 show the pressure (p/ρ) distribution of the flow field at different time. Compared with the simulation results of a single foil, the downstream domain of the 2-foil system shows more irregular and complex characters. For the system with the distance between the two foils less

than the chord length, the pressure between the two foils is quite stable. However, for systems with the distance between the two foils more than two times of the chord length, obvious shedding vortices develop not only in the downstream region, but also the region between the two foils. These vortices lead to the significant oscillation of the loading condition on the 2-foil system.

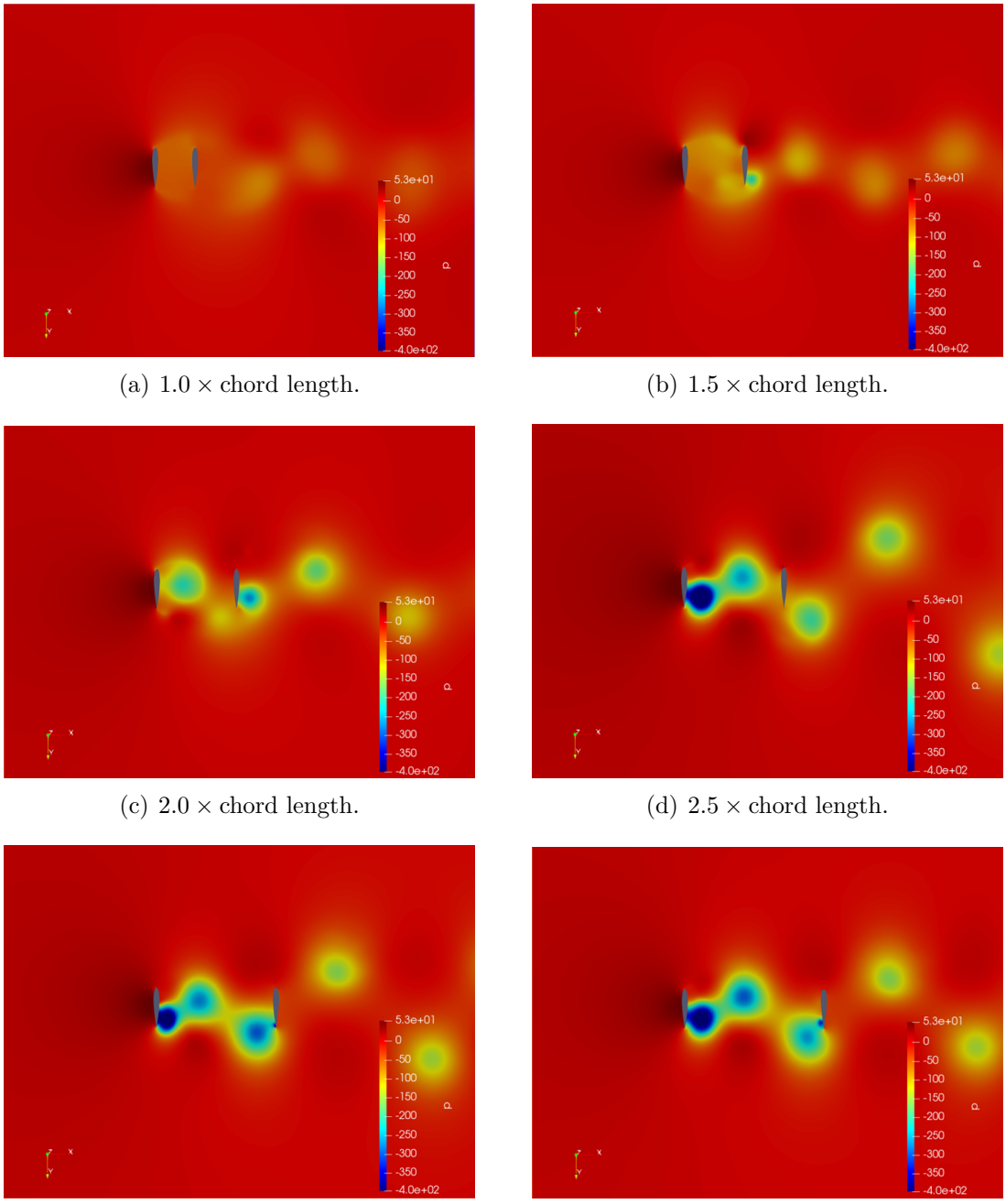

(a) 1.0 × chord length.

(b) 1.5 × chord length.

(c) 2.0 × chord length.

(d) 2.5 × chord length.

(e) 3.0 × chord length.

(f) 3.5 × chord length.

Figure 4.48: Pressure (p/ρ) distribution, 2D IDDES simulation for 2 foils with different distances in between at $t = 4$ s.

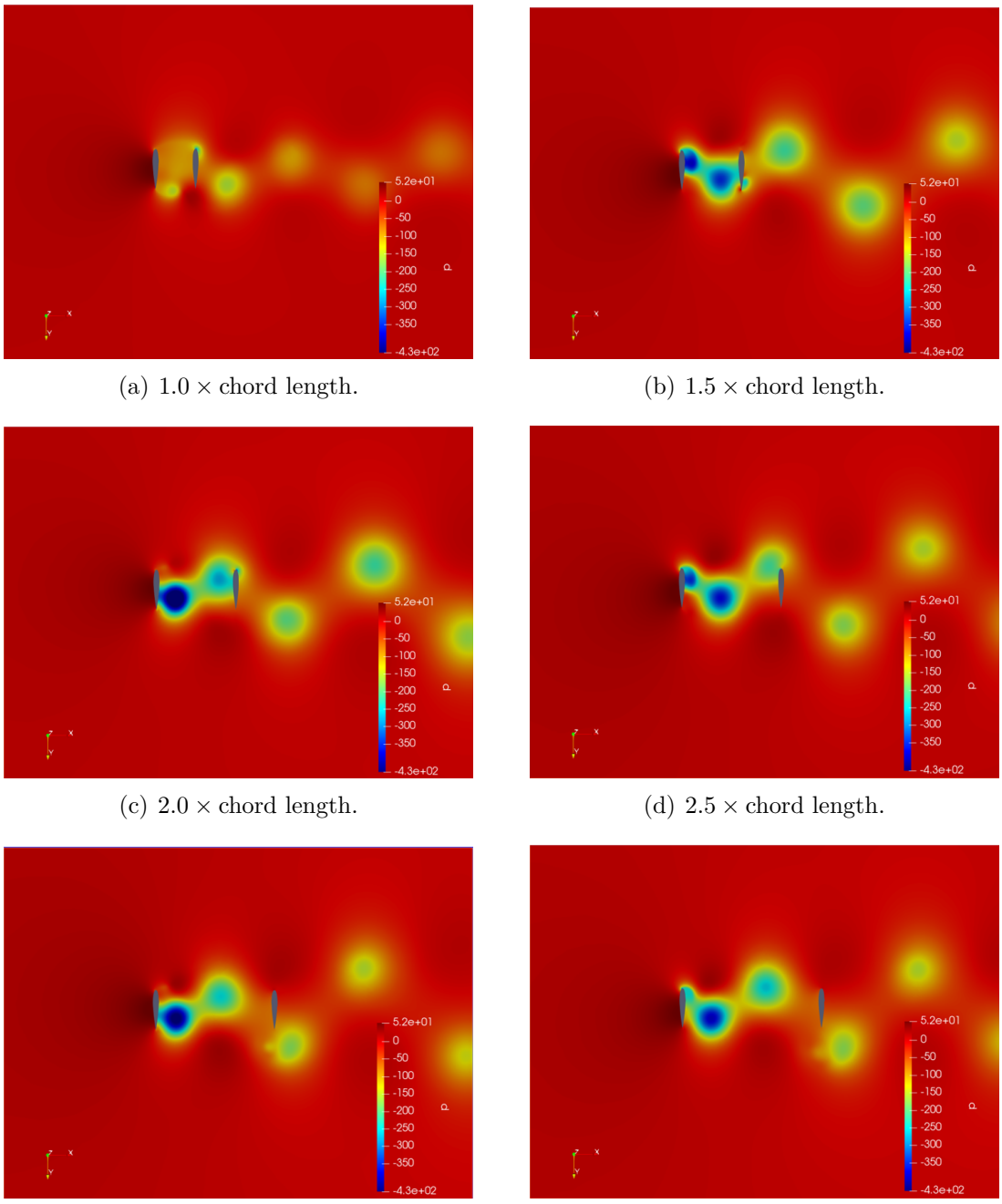

(a) 1.0 × chord length.

(b) 1.5 × chord length.

(c) 2.0 × chord length.

(d) 2.5 × chord length.

(e) 3.0 × chord length.

(f) 3.5 × chord length.

Figure 4.49: Pressure (p/ρ) distribution, 2D IDDES simulation for 2 foils with different distances in between at $t = 5$ s.

From an engineering perspective, a problem may occur that if the vorticities generated by the two foils overlap together. The strength of the vortex will be much amplified, which leads to a lower pressure zone behind the foil compared to the situation with a single foil. Then the system of the two foils will suffer from very a large drag force. Another problem may be the vortex-induced vibration. If the frequency of the vorticities is similar to the vibration frequency of the foil itself, the

foil will vibrate in a very large amplitude. Then the structure of the foil may be destroyed.

5

Conclusion and future work

5.1 Conclusion

For the studied cases under the low angles of attacks, the vorticity is not significant. From the simulation results, the pressure distribution along the foil agrees with the experimental data very well. In the sense of force coefficients, although the relative difference of drag force coefficients is quite large, the absolute difference is minute. Thus, the simulation can be considered to provide credible and reasonable results. The steady state and unsteady state simulations give similar results, so the flow is quite steady when the angle of attack is low. Since the unsteady simulations using URANS and DDES model also give similar results, the large eddy vorticities and flow separation are not significant under low angles of attack conditions. Although it is still uncertain whether the flow has significant 3D characters, the 2D simulation is enough to get quite accurate results in the sense of force coefficients.

For the NACA-0015 foil, the critical angle of attack is around 16°. When the angle of attack is larger than 16°, significant flow separation will appear on the suction side of the foil close to the trailing edge. The stall and the reduction on the lift coefficient generated by a foil as angle of attack increases happen at that angle of attack. The simulations based on RANS models cannot give accurate prediction when the angle of attack is larger than 16°. On the other hand, DES type models are suggested for these conditions since these models have better behavior in simulating the flow separation.

For the extreme conditions, i.e. the condition with an angle of attack as 90°, the most important characters of the flow field around the foil with high angle of attack are unsteady feature, vorticity, and 3D structure. The flow field has very significant unsteady feature, so steady-state simulations cannot give accurate prediction. The vortices develop one after another at the two tips of the foil, which compose the vortex street, and then dissipate in the downstream region. The vorticities cause a motional low-pressure region behind the foil and lead to the fluctuation of loading conditions. Obvious 3D flow occurs around the foil, which has a significant impact on the force condition of the foil.

The CFD simulations on foils with large angles of attack are quite difficult and many problems need to be properly solved. The most important difficulty for a deep stall

foil is the 3D flow structure. For simulations on a uniform 3D foil with infinite span length, the longitudinal height should be large enough, otherwise overestimation happens easily when the ratio between the height of the foil and the chord length is not appropriate. For wind tunnel experiments target on a deep stall foil, it is also important to make the foil long enough in the span wise to reduce the impact from the sidewalls.

It should be noticed that the study on the interaction between multi foils is based on 2D simulations and thus not quantitative relevant. For the interaction between multi foils, a more irregular and complex vortex street is clear in the downstream region, and it will separate into a larger domain compared with the single foil case. For two foils with the angle of attack as 90° and the distance less than 1.5 times the chord length in between, a quite stable low-pressure region with low velocity will occur between the two foils. However, if the distance between the two foils is larger than 1.5 times the chord length, the vortex street generated by the front foil will have remarkable influence on the next foil. In that situation, vortex induced oscillation may happen. For a wind-assisted propulsion ship under extreme conditions with more than one wingsail, the propulsive force generated by each wingsail is different. Thus, the propulsive force of the whole system of wingsails can not be simply considered as production of the force generated by one wingsail and the number of wingsails.

5.2 Future work

Due to the limitation of time, mesh refinement in the longitudinal direction is not analyzed. It's still not clear if the 3D mesh has completely reached its mesh independence. Thus, a detailed 3D mesh analysis can be carried out.

It's found that when running simulations for a deep stall foil, the ratio between the longitudinal span and chord length has a remarkable influence on the simulation results. Although the full span as the experiment is used as the final simulation case in this thesis, usually people are interested in the loading condition and flow feature without the influence from sidewalls. Simulations on a uniform foil with infinite span length has reference value. Several simulation cases can be performed to see how this ratio affects the simulation results.

For all the 90° angle of attack simulation cases in this thesis, the $k-\omega$ SST IDDES model is used for the unsteady states. Some other methods like LES and DNS are also suitable for this largely separated flow. Though these methods may have higher requirements on the numerical meshes or be more time-consuming, they may provide more accurate results than IDDES.

In the final case, the y^+ is set to be higher than 30 instead of being lower than 1. The total number of cells is saved by doing this, but some information may get lost in the boundary layers. A case with y^+ less than 1 can be carried out.

After getting reliable results, the simulation process can be used to predict the force

condition of realistic foil models, i.e. the wingsail, which is in the initial plan of this project. The propulsive force and the influence on the stability of the hull can also be estimated.

A series of simulations can also be carried out to research deeply into the interaction between foils. The vortex induced oscillations can be analyzed.

Bibliography

[1] M. Gimbutas. *The Goddesses and Gods of Old Europe, 6500-3500 BC, Myths and Cult Images*. University of California, 1982.

[2] D. Potts. *A companion to the archaeology of the ancient Near East*. John Wiley & Sons, 2012.

[3] J. C. Darnell. *The Wadi of the Horus Qa-a: a tableau of royal ritual power in the Theban Western Desert*. na, 2011.

[4] W. Mahdi. The dispersal of austronesian boat forms in the indian ocean. *Archaeology and language III: Artefacts, languages and texts*, pages 144–179, 1999.

[5] P. Johnstone. *The sea-craft of prehistory*. Psychology Press, 1988.

[6] I. C. Campbell. *The lateen sail in world history*. JSTOR, 1995.

[7] R. Dick-Read. *The phantom voyagers: Evidence of Indonesian settlement in Africa in ancient times*. Thurlton, 2005.

[8] F. Castro, N. Fonseca, T. Vacas, and F. Ciciliot. A quantitative look at mediterranean lateen-and square-rigged ships (part 1). *International Journal of Nautical Archaeology*, 37(2):347–359, 2008.

[9] G. Atkinson, H. Nguyen, and J. Binns. Considerations regarding the use of rigid sails on modern powered ships. *Cogent Engineering*, 5(1):1543564, 2018.

[10] I. M. Viola, M. Sacher, J. Xu, and F. Wang. A numerical method for the design of ships with wind-assisted propulsion. *Ocean Engineering*, 105:33–42, 2015.

[11] C. J. Satchwell. Applications of windship technology in the design and operation of wind-propelled ships. In *Regional Conference on Sail-Motor Propulsion*, 1985.

[12] G. M. Atkinson and J. Binns. Power profile for segment rigid sail. *Journal of Marine Engineering & Technology*, 17(2):99–105, 2018.

[13] K. E. Hansen, M. R. Bloch, and O. V. Jens. Modern windships. *Copenhagen:*

Knud E Hansen, 2000.

[14] L. Bergeson, G. L. Clemmer, J. E. York, A. P. Bates, and J. H. Mays. Wind propulsion for ships of the american merchant marine. *NTIS, SPRINGFIELD, VA, 1981, 276*, 1981.

[15] E. Rizzuto and C. G. Soares. *Sustainable Maritime Transportation and Exploitation of Sea Resources*. CRC Press, 2011.

[16] M. Traut, P. Gilbert, C. Walsh, A. Bows, A. Filippone, P. Stansby, and R. Wood. Propulsive power contribution of a kite and a flettner rotor on selected shipping routes. *Applied Energy*, 113:362–372, 2014.

[17] S. Wrage, M. Lohss, and S. Brabeck. Academic dictionaries and encyclopedias.

[18] Ø. Buhaug, J. J. Corbett, Ø. Endresen, V. Eyring, J. Faber, S. Hanayama, D. S. Lee, D. Lee, Hå. Lindstad, and A. Z. Markowska. Second imo ghg study 2009. *International Maritime Organization (IMO) London, UK*, 20, 2009.

[19] G. H. Elkaim. System identification for precision control of a wingsailed gps-guided catamaran. *A Dissertaton Submitted to the Department of Aeronautics and Astronautics and the Committee on Graduate Studies of Stanford University in partial fulfillment of the requirements for the degree of Doctor of Philosophy*, 2001.

[20] M. F. Silva, A. Friebe, B. Malheiro, P. Guedes, P. Ferreira, and M. Waller. Rigid wing sailboats: A state of the art survey. *Ocean Engineering*, 187:106150, 2019.

[21] C. Sauzé and M. Neal. Design considerations for sailing robots performing long term autonomous oceanography. In *International Robotic Sailing Conference*, pages 21–29. Centrobot, 2008.

[22] A. C. Domínguez-Brito, B. Valle-Fernández, J. Cabrera-Gámez, A. Ramos-de Miguel, and J. C. García. A-tirma g2: an oceanic autonomous sailboat. In *World Robotic Sailing championship and International Robotic Sailing Conference*, pages 3–13. Springer, 2015.

[23] A. Fiumara, N. Gourdain, V. Chapin, and J. Senter. Aerodynamic analysis of a c-class-like catamaran in simplified unsteady wind conditions using les and urans modeling. *Journal of Wind Engineering and Industrial Aerodynamics*, 180:262–275, 2018.

[24] K. Kijima, T. Katsuno, Y. Nakiri, and Y. Furukawa. On the manoeuvring performance of a ship with theparameter of loading condition. *Journal of the society of naval architects of Japan*, 1990(168):141–148, 1990.

[25] L. Larsson. Scientific methods in yacht design. *Annual review of fluid mechanics*, 22(1):349–385, 1990.

[26] J. He, Y. Hu, J. Tang, and S. Xue. Research on sail aerodynamics performance and sail-assisted ship stability. *Journal of Wind Engineering and Industrial Aerodynamics*, 146:81–89, 2015.

[27] D. Crane. Dictionary of aeronautical terms. aviation supplies & academics, 1997.

[28] J. Slotnick, A. Khodadoust, J. Alonso, D. Darmofal, W. Gropp, E. Lurie, and D. Mavriplis. Cfd vision 2030 study: a path to revolutionary computational aerosciences. 2013.

[29] C. P. Jackson. A finite-element study of the onset of vortex shedding in flow past variously shaped bodies. *Journal of fluid Mechanics*, 182:23–45, 1987.

[30] C. W. Knisely. Strouhal numbers of rectangular cylinders at incidence: a review and new data. *Journal of fluids and structures*, 4(4):371–393, 1990.

[31] M. R. Castelli, P. Cioppa, and E. Benini. Numerical simulation of the flow field around a vertical flat plate of infinite extent. *World Academy of Science, Engineering and Technology*, (61):284–289, 2012.

[32] R. E. Sheldahl and P. C. Klimas. Aerodynamic characteristics of seven symmetrical airfoil sections through 180-degree angle of attack for use in aerodynamic analysis of vertical axis wind turbines. Technical report, Sandia National Labs., Albuquerque, NM (USA), 1981.

[33] K. W. McAlister. *NACA 0015 wing pressure and trailing vortex measurements*, volume 3151. National Aeronautics and Space Administration, Office of Management ..., 1991.

[34] F. Bertagnolio. Naca0015 measurements in lm wind tunnel and turbulence generated noise. 2008.

[35] J. A. Ekaterinaris and M. F. Platzer. Computational prediction of airfoil dynamic stall. *Progress in aerospace sciences*, 33(11-12):759–846, 1998.

[36] S. A. Morton, J. R. Forsythe, K. D. Squires, and R. M. Cummings. Detached-eddy simulations of full aircraft experiencing massively separated flows. 2005.

[37] A. K. Travin, M. L. Shur, P. R. Spalart, and M. K. Strelets. Improvement of delayed detached-eddy simulation for les with wall modelling. 2006.

[38] N. Durrani and N. Qin. Behavior of detached-eddy simulations for mild airfoil trailing-edge separation. *Journal of Aircraft*, 48(1):193–202, 2011.

[39] F. Bertagnolio. Boundary layer measurements of the naca0015 and implications for noise modeling. 2011.

[40] Y. Yang and G. Zha. Simulation of airfoil stall flows using iddes with high order

schemes. In *46th AIAA Fluid Dynamics Conference*, page 3185, 2016.

[41] M. Sato, K. Asada, T. Nonomura, S. Kawai, and K. Fujii. Large-eddy simulation of naca 0015 airfoil flow at reynolds number of 1.6× 10 6. *AIAA Journal*, 55(2):673–679, 2017.

[42] J. S. Park, F. D. Witherden, and P. E. Vincent. High-order implicit large-eddy simulations of flow over a naca0021 aerofoil. *AIAA Journal*, pages 2186–2197, 2017.

[43] T. Fujiwara, K. Hirata, M. Ueno, and T. Nimura. On aerodynamic characteristics of a hybrid-sail with square soft sail. In *The Thirteenth International Offshore and Polar Engineering Conference*. International Society of Offshore and Polar Engineers, 2003.

[44] L. Davidson. Fluid mechanics, turbulent flow and turbulence modeling, 2015.

[45] N. J. Cook. The designer's guide to wind loading of building structures. vol. 2: Static structures. *Building Research Establishment Report, London: Butterworth,| c1990*, 1990.

[46] F. Menter and T. Esch. Elements of industrial heat transfer predictions. In *16th Brazilian Congress of Mechanical Engineering (COBEM)*, volume 109, page 650, 2001.

[47] F. R. Menter, M. Kuntz, and R. Langtry. Ten years of industrial experience with the sst turbulence model. *Turbulence, heat and mass transfer*, 4(1):625–632, 2003.

[48] C. J. Greenshields. Openfoam user guide. *OpenFOAM Foundation Ltd, version*, 3(1):e2888, 2015.

[49] P. R. Spalart. Comments on the feasibility of les for wings, and on a hybrid rans/les approach. In *Proceedings of first AFOSR international conference on DNS/LES*. Greyden Press, 1997.

[50] M. S. Gritskevich, A. V. Garbaruk, J. Schütze, and F. R. Menter. Development of ddes and iddes formulations for the k-ω shear stress transport model. *Flow, turbulence and combustion*, 88(3):431–449, 2012.

[51] M. Strelets. Detached eddy simulation of massively separated flows. In *39th Aerospace sciences meeting and exhibit*, page 879, 2001.

[52] L. S. Caretto, A. D. Gosman, S. V. Patankar, and D. B. Spalding. Two calculation procedures for steady, three-dimensional flows with recirculation. In *Proceedings of the third international conference on numerical methods in fluid mechanics*, pages 60–68. Springer, 1973.

[53] H. K. Versteeg and W. Malalasekera. *An introduction to computational fluid*

dynamics: the finite volume method. Pearson education, 2007.

[54] R. I. Issa. Solution of the implicitly discretised fluid flow equations by operator-splitting. *Journal of computational physics*, 62(1):40–65, 1986.

[55] E. N. Jacobs, K. E. Ward, and R. M. Pinkerton. *The Characteristics of 78 Related Airfoil Section from Tests in the Variable-Density Wind Tunnel*. Number 460. US Government Printing Office, 1933.

[56] G. Alexander. Aerospaceweb. org [cited 2013 march 22nd].

[57] M. S. Selig. Uiuc airfoil data site. 1996.

[58] Pointwise. Release 17, pointwise user manual, pointwise, 2015.

[59] M. D. Todorov. Determination of the aerodynamic characteristics of a light aircraft using ansys workbench and fluent software. *Romanian Review Precision Mechanics, Optics & Mechatronics*, (48):117, 2015.

[60] G. Karniadakis and S. Sherwin. *Spectral/hp element methods for computational fluid dynamics*. Oxford University Press, 2013.